

**New insights into the structure-performance  
relationships of Ce-based catalysts for synthesis  
of organic carbonates using CO<sub>2</sub>**

**Dissertation**

zur Erlangung des akademischen Grades

doctor rerum naturalium

(Dr. rer. nat.)

am Institut für Chemie

der Mathematisch-Naturwissenschaftlichen Fakultät

der Universität Rostock

vorgelegt von

M. Sc. Iuliia Prymak

geboren am 18.05.1987 in Charkiw, Ukraine

Rostock 2019

**Gutachter:**

1. Gutachter:

PD Dr. habil. Evgenii V. Kondratenko

Leibniz-Institut für Katalyse e.V., Universität Rostock

2. Gutachter:

Prof. Dr. Angelika Brückner

Leibniz-Institut für Katalyse e.V., Universität Rostock

**Datum der Einreichung: 14.05.2019**

**Datum der Verteidigung: 12.11.2019**

# Declaration

I declare that the work presented in this thesis entitled "New insights into the structure-performance relationships of Ce-based catalysts for synthesis of organic carbonates using CO<sub>2</sub>" is original and carried out by myself to obtain the doctoral degree at the Leibniz Institute for Catalysis e.V., Rostock, Germany, under the guidance of my supervisors PD Dr. habil. Andreas Martin (2011-2015, retired), PD Dr. habil. Evgenii V. Kondratenko (2015-2019, Department "Catalyst Discovery and Reaction Engineering", group "Reaction Mechanisms", Group leader) and Dr. Venkata Narayana Kalevaru (2011-2019, Department "Bioinspired Homo- & Heterogeneous Catalysis", Group "Gas Phase Oxidations", Group leader). I further declare that this thesis has not been submitted, either wholly or in part, to any academic institution for the award of any other degree or qualifications.

Rüsselsheim, 14.05.2019

Iuliia Prymak

*Dedicated to my lovely  
husband Dimitri and our son  
Mark....*

# Acknowledgements

First of all, I would like to sincerely thank my supervisor, **PD Dr. habil. Andreas Martin**, for his patient guidance, great support and advice throughout my Ph.D study. Under his guidance I learnt a lot and successfully overcame many difficulties. I also thank him for providing me with the opportunity to work with a talented team of researchers.

I would like also to acknowledge the head of "Reaction mechanism" group **PD Dr. habil. Evgenii V. Kondratenko** as my second supervisor and reader of my thesis, and I am gratefully indebted to him for his very valuable comments on my thesis.

I am deeply thankful to my co-supervisor **Dr. Venkata Narayana Kalevaru**. His door was always open whenever I had questions about my research or writing. Dr. V. N. Kalevaru steered me in the right direction whenever he thought I needed it.

Besides my official advisors, I would like to thank **Dr. Sebastian Wohlrab** as my mentor for his continuous support of my Ph.D study, motivation, and immense knowledge. His guidance helped me in all the time of research and upon writing of this thesis.

I am also grateful to Dr. U. Bentrup, Dr. M. Schneider, Dr. J. Radnik, Dr. M.-M. Pohl, Dr. H. Atia, Ms. A. Simmula, Mrs. K. Struve for their unfailing support and assistance upon catalyst characterisation.

I would like to extend my sincere esteems to all my colleagues in the Heterogeneous Catalytic Processes Department who have supported me along the way. A very special gratitude goes out to Dr. M. Polyakov for his input in my doctoral work. I thank my fellow labmates and very good friends Ailing, Radostina, Sven, Rafael for their helpful discussions and for all the fun we have had during my Ph.D study. I miss our interesting and long talks.

I am especially grateful to my beloved **Parents** for their endless love and support, without whom I would never have enjoyed so many opportunities; to my brother **Oleg** for his care and dedicated support. I thank with love to my husband **Dimitri** for his unconditional love, for giving me the strength and support. Many times I thought that it is impossible to continue Ph.D study, you helped me to believe in myself. I owe thanks to a very special person, my son **Mark**, who is the pride and joy of my life.

At last I'd like to thank many other people whose names are not mentioned here for help and support during my Ph.D study.

## Abstract

Carbon dioxide is a non-toxic, abundant and low-cost  $C_1$  feedstock. Its chemical utilization in various organic syntheses is certainly very attractive from both economic and environmental points of view, because  $CO_2$  is one of the most prominent greenhouse gases, being responsible for global warming. In this regard, this thesis is focused on a couple of industrially important catalytic reactions, where  $CO_2$  and  $C_1$ - $C_2$  alcohols (methanol or ethanol) are used as reactants to produce more valuable products, e.g. dimethyl carbonate (DMC) or diethyl carbonate (DEC). However, the one-step synthesis of organic carbonates from  $CO_2$  and alcohols is thermodynamically difficult and hence the yield of desired product reported so far is relatively low ( $\sim 2\%$ ). Therefore, the aim of this study is to achieve the maximal thermodynamically possible yield of dialkyl carbonate by various means such as (i) by applying high pressure conditions (80-180 bar) in the temperature range 80-180  $^{\circ}C$ , (ii) developing efficient catalyst compositions, (iii) using continuous flow system.

Literature survey reveals that  $ZrO_2$ ,  $CeO_2$  and their solid solutions are effective catalysts for the direct production of organic carbonates due to the presence of both acidic and basic sites on its surface, which consist of coordinatively unsaturated metal cations  $M^{4+}$ , oxide anions  $O^{2-}$  and hydroxyl groups. In order to further investigate the potential of  $CeO_2$ -based catalysts, the effects of (i) surface modifications with phosphoric acid, (ii) doping of second metal, i.e.  $Hf^{4+}$ ,  $Zr^{4+}$ ,  $Ti^{4+}$ , (iii) calcination temperature and (iv) various synthesis methods on the yield of dialkyl carbonate were explored in detail. Catalytic performance of these solids was first checked in batch runs (stainless steel autoclave) for the formation of DMC from methanol and  $CO_2$  and then in a continuous-mode operation using a plug-flow reactor (PFR) for the formation of DEC from ethanol and  $CO_2$ . The  $Ce_xM_{1-x}O_2$  ( $M$  = metal) catalysts exhibited significant differences in their performance mainly depending on (i) their  $Ce : M$  ratio, (ii) the different acid–base characteristics and phase composition, (iii) ability to form monodentate methoxy intermediates.

The catalysts containing 80 mol%  $Ce$  and 20 mol%  $Zr$  exhibited the most efficient performance ( $Y_{DMC} = 0.24\%$  and  $Y_{DEC} = 0.7\%$ ), which could be attributed to a good balance between the basic and acidic sites on its surface. The DMC yield was successfully improved further from 0.24% to 1.6% by phosphate modification of  $Ce_{0.8}Zr_{0.2}O_2$  ( $P/Zr = 0.12$ ).

# Zusammenfassung

Das Kohlenstoffdioxid ist nicht toxisch, ein reichlich verfügbarer und kostengünstiger  $C_1$  Rohstoff. Außerdem ist die chemische Verwertung von  $CO_2$  in der organischen Synthese unter Beachtung wirtschaftlicher und ökologischer Gesichtspunkte sehr attraktiv, da  $CO_2$  eins der wichtigsten Treibhausgase und möglicherweise für die globale Erwärmung verantwortlich ist. In dieser Hinsicht befasst sich die vorliegende Arbeit mit industriell bedeutsamen katalytischen Reaktionen, bei denen  $CO_2$  und  $C_1$ - $C_2$  Alkohole (Methanol bzw. Ethanol) als Edukte verwendet werden, um höherwertige Produkte, wie z.B. Dimethylcarbonat (DMC) und/oder Diethylcarbonat (DEC), herzustellen. Allerdings ist die direkte Synthese von organischen Carbonaten aus  $CO_2$  und Alkoholen thermodynamisch ungünstig und die Produktausbeute, wie in der Literatur berichtet, ist relativ gering ( $\sim 2\%$ ). Aus diesem Grund war das Ziel dieser Arbeit die maximal thermodynamisch mögliche Ausbeute von Dialkylcarbonat durch die Variation der i) Einwirkung von starkem Druck (80-180 bar) im Temperaturbereich 80-180 °C, durch ii) Entwicklung effizienter Katalysatorzusammensetzungen und durch iii) Verwendung eines Durchlaufsystems zu erreichen.

Die Literaturrecherche ergab, dass  $ZrO_2$ ,  $CeO_2$  und deren Mischkristalle als effektive Katalysatoren für die direkte Synthese von organischen Carbonaten verwendet werden können, da sie sowohl saure als auch basische Zentren an ihrer Oberfläche aufweisen, die aus den koordinativ ungesättigten Metallkationen  $M^{4+}$ , Oxidanionen  $O^{2-}$  und Hydroxylgruppen bestehen. Um das Potenzial von  $CeO_2$ -basierten Katalysatoren weiter zu erforschen, wurde die Auswirkung von (i) Oberflächenmodifikationen mittels Phosphorsäure, (ii) Dotierung mit einem zweiten Metall, z.B.  $Hf^{4+}$ ,  $Zr^{4+}$ ,  $Ti^{4+}$ , (iii) der Kalzinierungstemperatur und (iv) von verschiedenen Synthesemethoden auf die Ausbeute von Dialkylcarbonat detaillierter untersucht. Die katalytische Effektivität dieser Festkörper wurde zuerst durch die Bildung von DMC aus Methanol und  $CO_2$  in Eintopfsynthesen (Edelstahlautoklav) und dann durch eine Durchflusssynthese von DEC aus Ethanol und  $CO_2$  im Plug-Flow-Reaktor (PFR) getestet. Die  $Ce_xM_{1-x}O_2$ -Katalysatoren ( $M$  = Metall) zeichneten sich durch signifikante Unterschiede in ihrer Leistung aus, hauptsächlich abhängig von (i) dem  $Ce : M$  Verhältnis, (ii) den unterschiedlichen sauren und basischen Eigenschaften und der Phasenzusammensetzung, (iii) der Fähigkeit einzähnige Methoxy-Liganden als Zwischenprodukte zu bilden.

Die Katalysatoren, die 80 mol% Ce und 20 mol% Zr enthielten, wiesen das effizienteste Ergebnis ( $Y_{\text{DMC}} = 0.24\%$  und  $Y_{\text{DEC}} = 0.7\%$ ) auf, welches durch ein ausgewogenes Gleichgewicht zwischen den basischen und sauren Zentren auf deren Oberfläche erklärt werden konnte. Die Ausbeute an DMC wurde durch die Phosphat-Modifikation von  $\text{Ce}_{0.8}\text{Zr}_{0.2}\text{O}_2$  (P/Zr = 0.12) erfolgreich von 0.24 % auf 1.6 % erhöht.



# List of Abbreviations, Acronyms and Symbols

ABF	Annular Bright Field
atm.	Atmospheric Pressure [101.325 kPa]
a	Lattice Constant [nm]
→	Arrow Indicated Stationary Isothermal Treatment of the Samples
BET	Brunauer–Emmet–Teller
b	Lattice Constant [nm]
BJH	Barret–Joyner–Halenda
CP	Critical Parameters
CO <sub>2</sub> -TPD	Temperature Programmed Desorption of Carbon Dioxide
c	Lattice Constant [nm]
D	Crystallite Size [nm]
D <sub>r</sub>	Reactor Diameter [mm]
d <sub>p</sub>	Particle Diameter [mm]
d	Average Pore Diameter [nm]
DEC	Diethyl Carbonate
DMC	Dimethyl Carbonate
DME	Dimethyl Ether
DEE	Diethyl Ether
°C	Degree Celsius
EDXS	Energy Dispersive X-ray Spectroscopy
ε	Microstrain [%]
etc.	Et Cetera
e.g.	Exempli Gratia
et al.	Et Alii
EtOH	Ethanol
ESCA	Electron Spectroscopy for Chemical Analysis
EDXS	Energy Dispersive X-ray Spectroscopy
FID	Flame Ionization Detector
FTIR	Fourier Transformation Infrared Spectroscopy
FIZ Karlsruhe	Fachinformationszentrum Karlsruhe
GWP	Global Warming Potential



TCD	Thermal Conductivity Detector
TGA	Thermogravimetric Analysis
TPR	Temperature Programmed Reduction
$\tau$	Contact Time [s]
$T_{\max}$	Maximal Temperature [ $^{\circ}\text{C}$ ]
$T_c$	Calcination Temperature [ $^{\circ}\text{C}$ ]
$T_D$	Drying Temperature [ $^{\circ}\text{C}$ ]
$t$	Time [h]
$T$	Temperature [ $^{\circ}\text{C}$ ]
$T_{\text{cr}}$	Critical Temperature [ $^{\circ}\text{C}$ ]
U.S.	United State
UPS	Ultraviolet Photoelectron Spectroscopy
VLE	Vapor-Liquid Equilibrium
$V$	Volume of the Unit Cell [ $\text{nm}^3$ ]
wt%	Weight Percentage
$x$	Molar Fraction
XRD	X-ray Diffraction
XPS	X-ray Photoelectron Spectroscopy
$Y$	Yield [%]

# Structure of the thesis

The thesis is composed of seven chapters on the basis of motivation and objectives, state-of-the-art, catalyst preparation methods applied, characterization techniques used, modification of catalyst compositions and their catalytic results.

**Chapter 1** contains a general introduction on carbon dioxide properties and its applications in the chemical industry followed by a brief description of the organic carbonates, their properties and applications. In addition, effective catalysts used so far for the synthesis of dialkyl carbonate are described together with the operation conditions and catalyst performance. The use of different dehydrating agents in order to increase dialkyl carbonate yield will also be shortly discussed. Furthermore, the motivation and the objective of the current study are also presented.

**Chapter 2** summarizes the experimental procedures including solids preparation methods, basic principles and applications of different characterization techniques, description of the reaction setups and of evaluation of catalyst performance for the direct carboxylation of alcohols with carbon dioxide to dialkyl carbonates.

**Chapter 3** deals with the results and discussion about the effect of Ce/Zr ratio in  $\text{Ce}_x\text{Zr}_{1-x}\text{O}_2$  and surface modification of  $\text{Ce}_{0.8}\text{Zr}_{0.2}\text{O}_2$  by phosphoric acid on the catalytic performance for the direct synthesis of dimethyl carbonate (DMC) from methanol and  $\text{CO}_2$  using stainless steel autoclave. These catalysts are characterized by  $\text{N}_2$ -adsorption (BET-SA), XRD, ICP-OES, TEM, *in situ* FTIR,  $\text{NH}_3$ -TPD as well as  $\text{CO}_2$ -TPD.

**Chapter 4** demonstrates the data obtained from the catalytic tests for the direct synthesis of diethyl carbonate (DEC) from ethanol and  $\text{CO}_2$  under continuous-flow conditions over different  $\text{Ce}_x\text{Zr}_{1-x}\text{O}_2$  catalysts. The optimization of reaction conditions is also described in this chapter. The catalysts were characterized with the help of various physico-chemical methods mentioned above.

**Chapter 5** describes the influence of second metal in  $\text{Ce}_{0.8}\text{M}_{0.2}\text{O}_2$  catalyst, where M is a metal ( $\text{Hf}^{4+}$ ,  $\text{Ti}^{4+}$ ), on the catalytic performance for direct synthesis of DEC from ethanol and  $\text{CO}_2$ . Catalyst characterization using the techniques listed above is also studied.

**Chapter 6** explores the influence of synthesis parameters on the catalytic performance for the continuous production of DEC from CO<sub>2</sub> and ethanol, along with the solid state characterization to derive structure-performance correlations.

Finally, the main conclusions of this thesis are reviewed in **Chapter 7**, together with outlook for future research on the direct synthesis of organic carbonates from CO<sub>2</sub> and alcohols.

# Table of contents

1. General Introduction and Literature Overview .....	1
1.1. Carbon dioxide.....	2
1.1.1. Chemical and physical properties of carbon dioxide.....	2
1.1.2. World greenhouse gas emissions (GHG) .....	3
1.1.3. Utilization of CO <sub>2</sub> .....	5
1.2. Organic carbonates.....	6
1.2.1. Physical and chemical properties of dimethyl carbonate (DMC) and diethyl carbonate (DEC).....	6
1.2.2. Application of DMC and DEC .....	6
1.2.3. Production of DMC and DEC .....	7
1.3. State of the art: Carboxylation of alcohols.....	10
1.3.1. Suitable catalysts for DMC synthesis.....	10
1.3.2. Suitable catalysts for DEC synthesis .....	11
1.3.3. Thermodynamic restrictions .....	12
1.3.4. Phase behavior of the CO <sub>2</sub> + EtOH system .....	13
1.4. Motivation and objectives of the thesis.....	15
2. Experimental section: Preparation, testing and characterization methods .....	18
2.1. Catalyst preparation .....	19
2.1.1. Chemicals .....	19
2.1.2. Citrate complexation method.....	19
2.1.2.1. Ce <sub>x</sub> Zr <sub>1-x</sub> O <sub>2</sub> solids.....	19
2.1.2.2. Ce <sub>0.8</sub> Ti <sub>0.2</sub> O <sub>2</sub> solids.....	20
2.1.2.3. Ce <sub>0.8</sub> Hf <sub>0.2</sub> O <sub>2</sub> solids .....	20
2.1.3. Ce <sub>0.8</sub> Zr <sub>0.2</sub> O <sub>2</sub> solid solutions prepared by co-precipitation.....	20
2.1.4. Ce <sub>x</sub> Zr <sub>1-x</sub> O <sub>2</sub> via oxalate gel co-precipitation method .....	21

2.1.5.	Phosphated $\text{Ce}_x\text{Zr}_{1-x}\text{O}_2$ : co-precipitation and wet impregnation .....	22
2.2.	Catalyst characterization .....	23
2.2.1.	Thermogravimetric analysis (TGA) .....	23
2.2.2	Nitrogen adsorption: BET and BJH methods .....	23
2.2.3	X-ray diffraction studies (XRD).....	24
2.2.4	Inductively coupled plasma optical emission spectroscopy (ICP-OES) .....	25
2.2.5	X-ray photoelectron spectroscopy (XPS) .....	25
2.2.6	Transmission electron microscopy (TEM).....	25
2.2.7	Temperature-programmed reduction (TPR) using $\text{H}_2$ as the reduction agent ..	26
2.2.8	Temperature programmed desorption (TPD) using $\text{NH}_3$ as basic probe and $\text{CO}_2$ as acidic probe.....	26
2.2.9	Fourier Transform Infrared Spectroscopy (FTIR).....	27
2.3.	Experimental system and catalytic tests.....	27
2.3.1.	Continuous flow reactor .....	27
2.3.2.	Batch reactor .....	29
2.3.3.	Analysis: Gas chromatography.....	30
2.3.3.1.	Continuous reaction .....	30
2.3.3.2.	Batch reaction .....	31
3.	Ce-Zr mixed oxide catalysts and surface modified $\text{Ce}_{0.8}\text{Zr}_{0.2}\text{O}_2$ for the direct synthesis of dimethyl carbonate from methanol and $\text{CO}_2$ .....	32
3.1.	Ce-Zr mixed oxide catalysts for the direct synthesis of dimethyl carbonate from methanol and carbon dioxide .....	33
3.1.1.	Catalysts characterization .....	33
3.1.2.	Catalytic results .....	39
3.2.	Surface modified $\text{Ce}_{0.8}\text{Zr}_{0.2}\text{O}_2$ catalyst for direct synthesis of dimethyl carbonate from methanol and $\text{CO}_2$ . .....	41
3.2.1.	Catalysts characterization .....	41
3.2.2.	Catalytic results .....	48

3.3. Summary .....	49
4. Continuous synthesis of diethyl carbonate from ethanol and CO <sub>2</sub> over Ce <sub>x</sub> Zr <sub>1-x</sub> O <sub>2</sub> (x = 0, 0.2, 0.5, 0.8, 1) catalysts .....	52
4.1. An effective Ce <sub>x</sub> Zr <sub>1-x</sub> O <sub>2</sub> catalysts for the continuous synthesis of DEC from CO <sub>2</sub> and ethanol : effect of varying reaction conditions .....	53
4.1.1. Catalysts characterization .....	53
4.1.2. Catalytic results: effect of Ce/Zr ratio, temperature and pressure on catalytic performance .....	60
4.1.3. Catalytic results and materials properties affecting the catalyst activity .....	62
4.2. Impact of calcination temperature on catalytic properties of Ce <sub>0.8</sub> Zr <sub>0.2</sub> O <sub>2</sub> solids .....	64
4.2.1. Catalysts characterization .....	64
4.2.2. Catalytic results and material properties affecting the activity .....	71
4.3. Effect of LHSV and ratio of EtOH : CO <sub>2</sub> on catalytic performance .....	73
4.4. Conclusions .....	74
5. Effect of second metal in Ce <sub>0.8</sub> M <sub>0.2</sub> O <sub>2</sub> catalysts on the catalytic activity towards DEC synthesis from ethanol and CO <sub>2</sub> .....	76
5.1. Catalyst characterization .....	77
5.2. Catalytic results .....	83
5.3. Conclusions .....	85
6. Influence of synthesis parameters on catalytic performance of Ce <sub>0.8</sub> Zr <sub>0.2</sub> O <sub>2</sub> in the production of diethyl carbonate from ethanol and CO <sub>2</sub> .....	86
6.1. Catalyst characterization .....	87
6.3. Conclusions .....	94
7. Summary and Outlook .....	95
7.1. Ce-Zr mixed oxide catalysts and surface modified Ce <sub>0.8</sub> Zr <sub>0.2</sub> O <sub>2</sub> for the direct synthesis of dimethyl carbonate from methanol and CO <sub>2</sub> .....	95
7.2. Continuous synthesis of diethyl carbonate from CO <sub>2</sub> and ethanol over Ce <sub>x</sub> Zr <sub>1-x</sub> O <sub>2</sub> (x = 0, 0.2, 0.5, 0.8, 1) catalysts .....	96

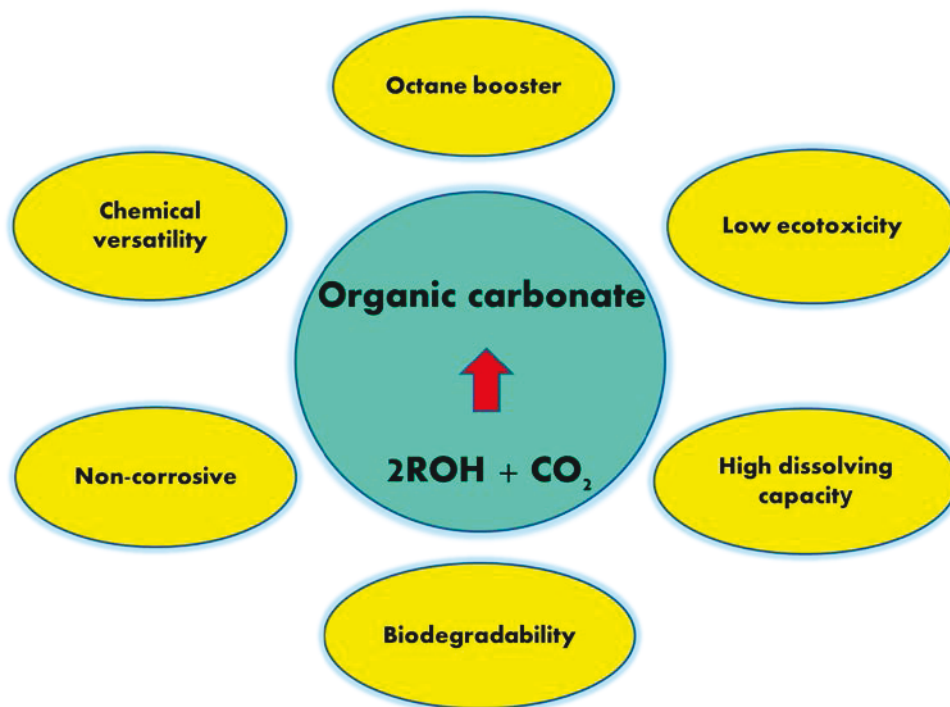


7.3. Effect of second metal in $\text{Ce}_{0.8}\text{M}_{0.2}\text{O}_2$ catalysts on the catalytic activity towards DEC synthesis from ethanol and $\text{CO}_2$ .....	98
7.4. Influence of synthesis methods on catalytic performance of $\text{Ce}_{0.8}\text{Zr}_{0.2}\text{O}_2$ in the production of diethyl carbonate from ethanol and $\text{CO}_2$ .....	98
7.5. Outlook.....	99
8. References.....	101

# Chapter 1

## 1. General Introduction and Literature Overview

*Chapter 1 comprises a thorough literature survey on production of organic carbonates with a special emphasis on technologies of dimethyl carbonate and diethyl carbonate synthesis. It starts with a short description of the physical and chemical properties of carbon dioxide and its applications in chemical industries. The main focus is put on direct synthesis of organic carbonates via carboxylation of alcohols and effective heterogeneous catalysts. Moreover, various drawbacks of this reaction, such as thermodynamic limitations and hydrolysis of products, are also discussed. Physical and chemical properties as well as industrial applications of these carbonates are also introduced and discussed (Scheme 1). The motivation and main objectives of the thesis are given at the end.*



*Scheme 1. Important properties of organic carbonates for industrial uses.*

## 1.1. Carbon dioxide

### 1.1.1. Chemical and physical properties of carbon dioxide

Carbon dioxide (CO<sub>2</sub>) is a non-toxic, abundant and relatively cheap C<sub>1</sub> feedstock. It is a major greenhouse gas, however it is considered as a substitute to phosgene currently used for large-scale DMC synthesis [1, 2]. The oxidation number of carbon in CO<sub>2</sub> is +IV. For chemical conversion of CO<sub>2</sub>, a substantial input of energy, effective reaction conditions and active catalysts are typically required because CO<sub>2</sub> is a highly thermodynamically and kinetically stable molecule. However, CO<sub>2</sub> has a strong affinity towards electron-donating reagents and thus, rapidly reacts with basic compounds, like ammonia. CO<sub>2</sub> is used for various industrial applications: chemicals, pharmaceuticals, foodstuffs, beverage, healthcare, laboratories and analysis (mobile phase in supercritical chromatography), safety (CO<sub>2</sub> for fire extinguishers) [3]. Selected physical and chemical properties of CO<sub>2</sub> are summarized in Table 1.1.

**Table 1.1.** Physical and chemical properties of CO<sub>2</sub>.

Property	Value	Unit
Molecular weight	44.01	g·mol <sup>-1</sup>
Gas density at 273 K and 1 atm.	1.977	kg·m <sup>-3</sup>
Liquid density at 293 K and 56 atm.	770	kg·m <sup>-3</sup>
Solid density at 195 K and 1 atm.	1562	kg·m <sup>-3</sup>
Triple point at 5.1 atm.	-56.5	°C
Critical temperature	31.04	°C
Critical pressure	72.85	bar
Critical density	468	kg·m <sup>-3</sup>

The physical state of CO<sub>2</sub> changes with temperature and pressure. As shown in Figure 1.1a, CO<sub>2</sub> has three states: solid, liquid and gas. However, at temperatures and pressures above the critical point ( $T_{cr} = 31.1^{\circ}\text{C}$ ,  $p_{cr} = 73.8$  bar), CO<sub>2</sub> behaves as a supercritical fluid. Under these conditions, CO<sub>2</sub> is in a single phase with both liquid and gas properties. Carbon dioxide has no liquid state at pressures below 5.1 atm. At atmospheric pressure and temperatures below  $-78.5^{\circ}\text{C}$  gaseous CO<sub>2</sub> is converted into a solid and the solid sublimates directly to a gas above  $-78.5^{\circ}\text{C}$ . Liquid CO<sub>2</sub> is formed only at pressures and temperatures above 5.1 atm. and above  $-56.6^{\circ}\text{C}$ . The density of CO<sub>2</sub> varies with temperature and pressure (Figure. 1.1b). At critical pressure, its compressibility is maximized, and small changes in temperature can lead to big changes in CO<sub>2</sub> local density and its solubility [4]. Supercritical

CO<sub>2</sub> is an important commercial and industrial solvent due to its role in chemical extraction in addition to its low toxicity and environmental impact.

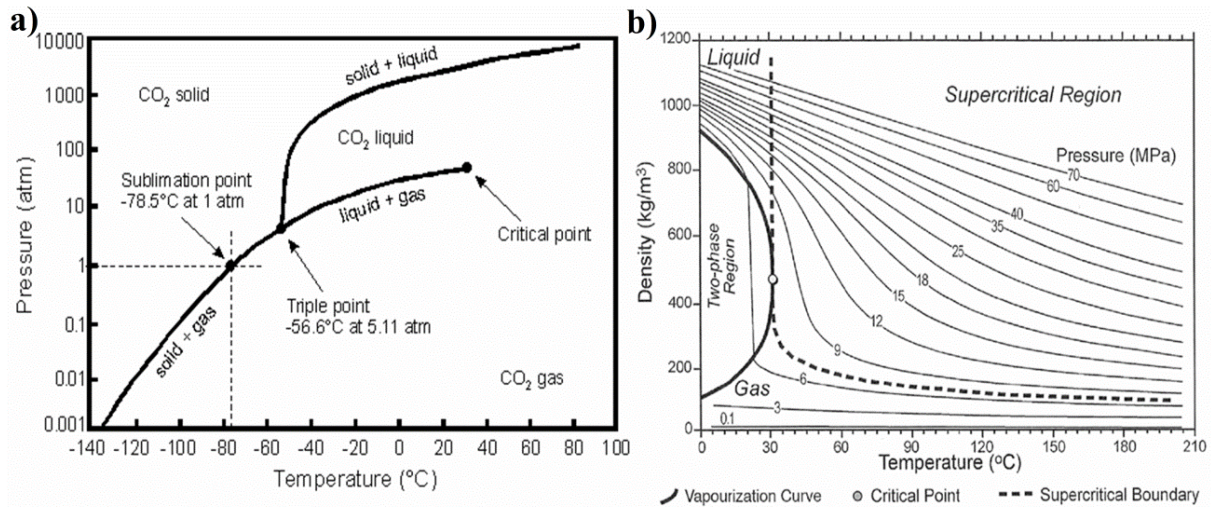


**Figure 1.1.** (a) Phase diagram for CO<sub>2</sub> and (b) Variation of density as a function of temperature and pressure (reprinted from the Annex of IPCC [5]).

### 1.1.2. World greenhouse gas emissions (GHG)

Carbon dioxide (CO<sub>2</sub>), methane (CH<sub>4</sub>) and nitrous oxide (N<sub>2</sub>O) are some of the major greenhouse gases (GHG) with a large global warming potential (GWP). GWP is a measure of the radiative forcing of a unit mass of a given greenhouse gas in atmosphere integrated over a selected time horizon, relative to that of CO<sub>2</sub> (Table 1.2). Thus, if a molecule has a longer atmospheric lifetime than CO<sub>2</sub> its GWP will increase with the timescale considered. CO<sub>2</sub> has a GWP of 1 over all time periods.

**Table 1.2.** GWP values of various greenhouse gases [6].

Gas	Lifetime (year)	Global warming potential		
		20-yr	100-yr	500-yr
CO <sub>2</sub>	-	1	1	1
CH <sub>4</sub>	12	72	25	7.6
N <sub>2</sub> O	114	289	298	153

Figure 1.2a represents a relative fraction of anthropogenic greenhouse gases originating from eight categories of sources, as estimated by the Emission Database for Global Atmospheric Research version 3.2 [7]. Anthropogenic emissions are emissions related with human activities including combustion of fossil fuels, deforestation, livestock etc. Global annual emissions of CO<sub>2</sub>, CH<sub>4</sub> and N<sub>2</sub>O in 2017 were 73%, 18%, and 6%, respectively.

Figure 1.2b shows changes in the global emissions of CO<sub>2</sub> in the period of time from 1995-2017. 2017 was an outstanding year in which emissions increased by 1.2% and reached 37.1 gigatonnes (Gt). The largest producers of energy-related CO<sub>2</sub> emissions in 2017, based on their share of global energy-related CO<sub>2</sub> emissions, were: China, U.S., India, Russia, Brazil and Japan (Figure 1.2b (inset)). China was the biggest emitter of CO<sub>2</sub> that accounted for around 25% of global CO<sub>2</sub> emissions.

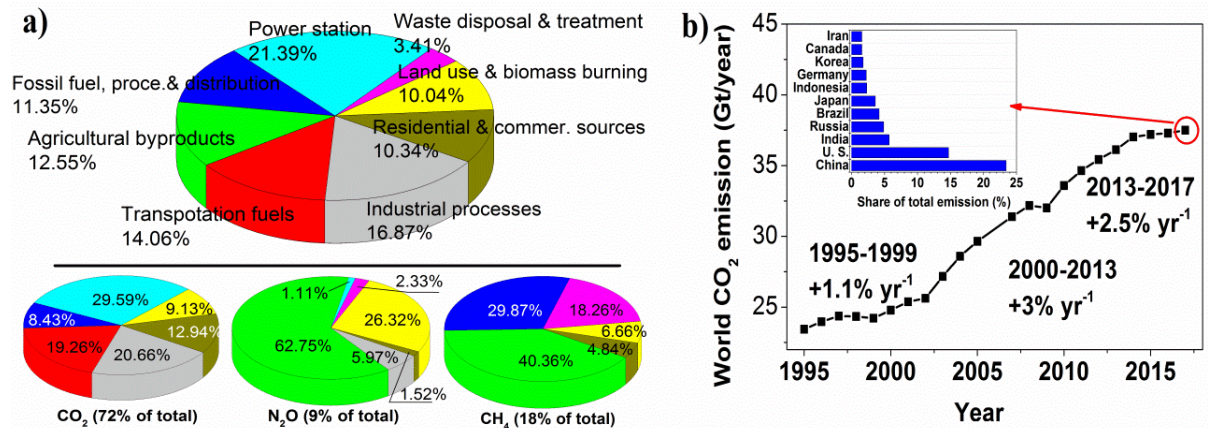


**Figure 1.2.** (a) Annual greenhouse gas emission by sector. Lower panel: comparable information for CO<sub>2</sub>, CH<sub>4</sub> and N<sub>2</sub>O (quoted from work of Robert A. Rohde, source [8]). (b) Global CO<sub>2</sub> emissions from 1995 to 2017 [9-11]. Inset: Global CO<sub>2</sub> emission by region in 2017.

It is a well-known fact that greenhouse gases are responsible for global climate change. There are some key issues related to GHG control and utilization: energy economics, policy regulations, environmental protections and global climate change. Carbon dioxide is today's greenhouse gas number one (73% of total emissions). A continuous temperature increase on the Earth (1.2 °C since 1850), caused by increased CO<sub>2</sub> concentration in the atmosphere, results in melting of arctic Sea ice, increased forest fires, rising sea levels, loss of animal habitat, spreading of tropical diseases and more frequent and severe storms [12, 13].

Figure 1.3 shows three main pathways for utilizing of CO<sub>2</sub>:

- Conversion of CO<sub>2</sub> into fuels
- Utilization of CO<sub>2</sub> as a feedstock for synthesis of chemicals
- Non-conversional use of CO<sub>2</sub>.



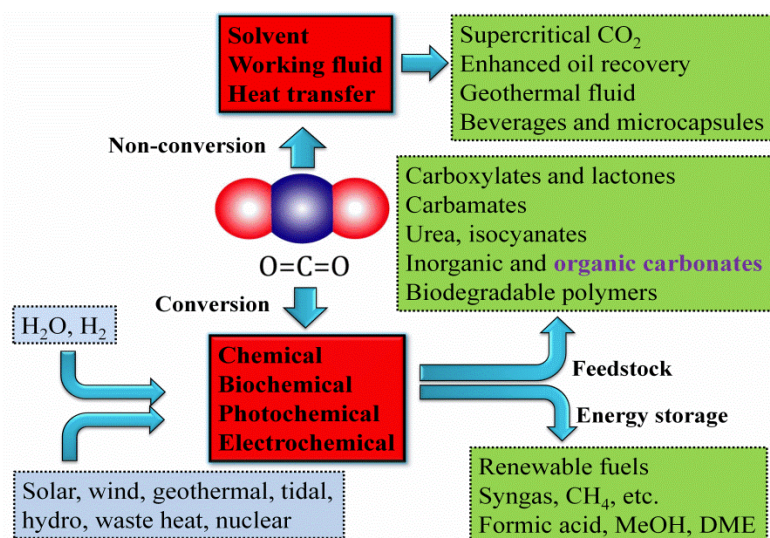


**Figure 1.3.** Different pathways of utilization of CO<sub>2</sub> (quoted from work of Sridhar, source [14]).

### 1.1.3. Utilization of CO<sub>2</sub>

In 2003 the global market for merchant CO<sub>2</sub>, measured by the amount of CO<sub>2</sub> sold in the market, was estimated to be \$3.2 billions [15]. Thus, CO<sub>2</sub> conversion into various useful chemical products is very attractive from both economic and environmental points of view.

The main processes for CO<sub>2</sub> conversion and application in the chemical industry are:

- CO<sub>2</sub> hydrogenation to various compounds, depending upon the catalysts used and reaction conditions applied
  - $\text{CO}_2 + 3\text{H}_2 \rightarrow \text{CH}_3\text{OH} + \text{H}_2\text{O}$ ,  $\Delta H^{273} = -49.5 \text{ kJ/mol}$ : low conversion resulting in high volume of recycled gases, 5 Mt/year of methanol, important petrochemicals in industry [16, 17].
  - $\text{CO}_2 + \text{H}_2 \rightarrow \text{HCOOH}$ ,  $\Delta H^{273} = -31.6 \text{ kJ/mol}$ : reactant for electrochemical fuel cells [18].
  - $\text{CO}_2 + \text{H}_2 \rightleftharpoons \text{CO} + \text{H}_2\text{O}$ ,  $\Delta H^{273} = +41.19 \text{ kJ/mol}$ : provides a synthetically valuable CO from cheap CO<sub>2</sub> [19].
- Dry reforming of methane ( $\text{CH}_4 + \text{CO}_2 \rightarrow 2\text{CO} + 2\text{H}_2$ ,  $\Delta H^{273} = +247.3 \text{ kJ/mol}$ ) gives syngas [20].
- Synthesis of urea ( $\text{CO}_2 + 2\text{NH}_3 \rightarrow \text{CO}(\text{NH}_2)_2 + \text{H}_2\text{O}$ ,  $\Delta H^{273} = -134 \text{ kJ/mol}$ ) is the largest-volume industrial example of converting CO<sub>2</sub>, 146 Mt of urea/year [21].
- Production of salicylic acid ( $\text{C}_6\text{H}_5\text{OH} + \text{CO}_2 \rightarrow \text{C}_7\text{H}_6\text{O}_3$ ,  $\Delta H^{273} = -90.1 \text{ kJ/mol}$ ), which is used for making Aspirin, 170 kT/year of salicylic acid.

Obviously, many reactions for CO<sub>2</sub> conversion involve positive change in enthalpy and thus they are endothermic in nature. In addition, there are many other methodologies to transform carbon dioxide into various commercially important products, for instance, transformation of CO<sub>2</sub> into cyclic carbonates by cycloaddition with epoxides [22, 23] or glycols [23] and via oxidative carboxylation of olefins with CO<sub>2</sub> [23], synthesis of ethanol (70 Mt/year) from CO<sub>2</sub> and H<sub>2</sub> [24] etc. Among different approaches, direct synthesis of organic carbonates from alcohols and CO<sub>2</sub> [25, 26] is gaining huge interest in recent times due to their high commercial significance. Efforts have been made to produce fuel additives from CO<sub>2</sub> without using hydrogen source. For instance, dimethyl carbonate (DMC) from methanol and CO<sub>2</sub> [23, 27, 28] or diethyl carbonate (DEC) from ethanol and CO<sub>2</sub> [29-31] were found to be effective fuel additives.

## **1.2. Organic carbonates**

### **1.2.1. Physical and chemical properties of dimethyl carbonate (DMC) and diethyl carbonate (DEC)**

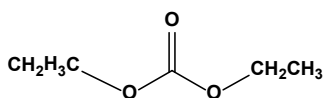
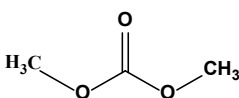
Dialkyl carbonates are low toxic, non-corrosive and readily biodegradable [32]. They are useful intermediates for manufacture of polycarbonates through a non-phosgene process [33]. Among different approaches, direct synthesis of organic carbonates from alcohols and CO<sub>2</sub> [25, 26] is gaining huge interest in recent times due to commercial significance of organic carbonates. For instance, dimethyl carbonate (DMC) from methanol and CO<sub>2</sub> [23, 27, 28] or diethyl carbonate (DEC) from ethanol and CO<sub>2</sub> [29-31] are two challenging examples of CO<sub>2</sub> utilization. Some properties of DEC and DMC are summarized in Table 1.3.

### **1.2.2. Application of DMC and DEC**

The catalytic synthesis of DMC is currently studied intensively owing to wide applications of this chemical such as solvent [34], raw material for production of polycarbonate resins [35], electrolyte solvent [36, 37] and in pharmacy [38]. In contrast, DEC the second homologue in short-chain dialkylcarbonate family played only a negligible role, although DEC is also used as a raw material for production of polycarbonates [39], as solvent and intermediate for various pharmaceuticals [40, 41], as solvent for polyamides, polyacrylonitriles and diphenol resins in the synthetic fiber industry, as solvent for cellulose ethers, synthetic and natural resins in the textile printing and dyeing industry, as paint remover and as electrolyte in lithium ion batteries [42]. CH<sub>3</sub>-/C<sub>2</sub>H<sub>5</sub>- and -CO- functional groups in the DMC / DEC molecules,

respectively, are suited for alkylation and carbonylation making a green substitution of phosgene, dimethyl sulfate/methyl iodide and ethyl/methyl halides possible [32, 34, 43, 44]. Furthermore, DMC and DEC contain 53.3 and 40.6 wt.% of oxygen, respectively, and thus can be used as an additive to diesel fuel due to their high octane booster power (Table 1.3) [34] to improve the performance of gasoline combustion. Engine tests show that 5 wt% DEC in diesel fuel can reduce particulate emissions by up to 50% [45]. DMC and DEC have more oxygen content per volume than methyl *tert*-butyl ether (MTBE, 18.2%). Moreover, the use of MTBE as an oxygen-containing fuel additive has a negative environmental impact.

**Table 1.3.** Selected properties of DEC and DMC [46].

Property	DEC	DMC	Unit
Molecular formula	$(C_2H_5O)_2CO$	$(CH_3O)_2CO$	-
			
Molar mass	118.13	90.08	$g \cdot mol^{-1}$
Density	0.975	1.069-1.073	$g \cdot cm^{-3}$
Boiling point	126-128	90	$^{\circ}C$
Melting point	-43	4	$^{\circ}C$
Flash point	33	17	$^{\circ}C$
Blending octane (R+M)/2*	104-106	103-116	-
Toxicity	Mildly toxic	Slightly toxic	
Oral acute toxicity (rats)	$LD_{50} = 1.57$	$LD_{50} = 13.8$	$g \cdot kg^{-1}$

\*R is the research octane number and M stands for motor octane number

### 1.2.3. Production of DMC and DEC

The world-wide production of DMC in 1993 was estimated to be 0.1 Mt per year [47, 48], in 1997 was estimated around 0.06 Mt/year and in 2006 to be 0.1-0.15 Mt/year [49]. The global consumption of DMC is majorly driven by including polycarbonate industry (51%), solvent (24%) and other (25%). Hence, global market size for dimethyl carbonate was valued over 410 million USD and its compound general growth rate is expected to exceed 5% by 2024 [50]. In a contrast, DEC production capacity is estimated to be much lower [51]. The demand of DMC/DEC is much higher than the production and hence lots of efforts have been done in order to find a sustainable route to produce DMC in large scale.



<b>Scheme 1: Phosgenation</b>	$2 \text{ ROH} + \text{Cl}-\overset{\text{O}}{\parallel}{\text{C}}-\text{Cl} \xrightarrow{\text{CO} + \text{Cl}_2} \text{R}-\text{O}-\overset{\text{O}}{\parallel}{\text{C}}-\text{O}-\text{R} + 2 \text{ HCl}$
<i>Drawbacks</i>	acid waste, corrosive, toxic, co-production of salt
<i>Advantages</i>	pure products with high yields
<i>Producer</i>	Bayer (Germany)

Up to beginning of the 1980s, dialkyl carbonates were mainly produced by the Bayer company developed a process on the basis of the reaction of alcohols with phosgene in the presence of sodium hydroxide (Scheme 1) [52-54]. However, the main disadvantages of this route are the use of poisonous gas (phosgene) and co-production of large amounts of salt in a subsequent neutralization step.

<b>Scheme 2: Oxidative carbonylation of alcohols</b>	$2 \text{ ROH} + \text{CO} + 0.5 \text{ O}_2 \longrightarrow \text{R}-\text{O}-\overset{\text{O}}{\parallel}{\text{C}}-\text{O}-\text{R} + \text{H}_2\text{O}$
<i>Drawbacks</i>	corrosive, flammable, toxic
<i>Advantages</i>	high yields of products
<i>Producer</i>	ENIChem (Italy)

To fulfil the growing market demand, new synthetic technologies were developed on the basis of CO or CO<sub>2</sub>, which were used as phosgene substitutes. As a result, a new industrial process was developed at ENIChem (1983), which is based on the oxidative carbonylation of alcohols over metal catalysts such as copper- or palladium-based solids (Scheme 2) [55, 56].

<b>Scheme 3: Carbonylation of alkyl nitrite</b>	$2 \text{ ROH} + 2 \text{ NO} + 0.5 \text{ O}_2 \longrightarrow \text{O}=\text{N}-\text{O}-\text{R} + \text{H}_2\text{O}$ $\text{O}=\text{N}-\text{O}-\text{R} + \text{CO} \longrightarrow \text{R}-\text{O}-\overset{\text{O}}{\parallel}{\text{C}}-\text{O}-\text{R} + 2 \text{ NO}$
<i>Drawbacks</i>	Combination of three reagents (EtOH/MeOH, NO and O <sub>2</sub> )-highly exothermic and explosive under certain reaction conditions; methyl/ethyl nitrite is highly reactive; not environmentally friendly process-formation of NO
<i>Advantages</i>	without deactivation of catalyst
<i>Producer</i>	UBE (Japan)

Nowadays, dialkyl carbonates are mainly produced via oxidative carbonylation of alcohols in both gaseous and liquid phase in the presence of Cu-based catalysts (Versalis/Lummus technology, China and N.W. Europe location bases). However, this process uses an explosive gas mixture (CO/O<sub>2</sub>) under certain reaction conditions.

<b>Scheme 4:</b> <b>Transesterification of cyclic carbonate</b>	
<i>Drawbacks</i>	explosive, unfavorable equilibrium
<i>Advantages</i>	environmentally friendly synthetic route, ethylene glycol as by-product
<i>Current producer</i>	Asahi technology (USA)

In addition several other routes are applied like carbonylation of alkyl nitrite (UBE, 1983) using Pd/carbon catalysts (Scheme 3) [57-59], transesterification of ethylene carbonate with alcohols in the presence of Sn, Zr and Ti complexes (Scheme 4) [60, 61] or transesterification of urea with alcohols using metal oxide catalysts like ZnO (Scheme 5) [62, 63]

<b>Scheme 5: Transesterification of urea</b>	
<i>Drawbacks</i>	unfavorable equilibrium
<i>Advantages</i>	environmentally friendly and atom efficient, NH <sub>3</sub> can be recycled for the preparation of urea
<i>Current producer</i>	CDT technology

Since the 1980s alternative routes to form linear carbonates via direct carboxylation of alcohols in liquid as well as in gaseous phase have been reported [27, 64-69]. The direct synthesis of organic carbonates from CO<sub>2</sub> and alcohols represents one of the proposed favorable processes (Scheme 6). The one-step synthesis of dialkylcarbonates from CO<sub>2</sub> and alcohols allows CO<sub>2</sub> to be viewed as non-toxic, non-flammable, non-corrosive and abundant feedstock. This route will be deeply discussed in the next sections.

<b>Scheme 6: Carboxylation of alcohols</b>	$2 \text{ ROH} + \text{CO}_2 \rightleftharpoons \text{R-O-C(=O)-O-R} + \text{H}_2\text{O}$
<i>Drawbacks</i>	unfavorable thermodynamic equilibrium, H <sub>2</sub> O co-production
<i>Advantages</i>	environmentally friendly synthetic route, low cost of materials
<i>Current producer</i>	laboratory scale

### 1.3. State of the art: Carboxylation of alcohols

#### 1.3.1. Suitable catalysts for DMC synthesis

Until now, a wide range of catalytic systems had been studied for direct synthesis of DMC from methanol and CO<sub>2</sub> (see Table A1.2). For instance, group IV- and V-metal alkoxides (e.g. Nb, Ta, V, Ti) [70-72], organometallic compounds such as n-Bu<sub>2</sub>Sn(OCH<sub>3</sub>)<sub>2</sub> [73-77] and (MeO)<sub>2</sub>ClSi(CH<sub>2</sub>)<sub>3</sub>SnCl<sub>3</sub> [78], K<sub>2</sub>CO<sub>3</sub> in presence of C<sub>2</sub>H<sub>5</sub>I as co-reagent [79], CH<sub>3</sub>OK in presence of CH<sub>3</sub>I [80], Keggin type heteropoly compounds with different counteranions, like Co or Fe, and addenda atoms, like W or Mo [81-84], basic zeolites [85], metal oxides [67, 86, 87], mixed metal oxides [28, 66, 88, 89] and supported catalysts (Cu-Fe/SiO<sub>2</sub>, CeO<sub>2</sub>/Al<sub>2</sub>O<sub>3</sub>, Cu-Ni/graphite, CuCl<sub>2</sub>/AC, Rh/ZSM-5) [46, 90-92]. Among those catalysts, ZrO<sub>2</sub>, CeO<sub>2</sub> and their mixtures showed very promising performance [65, 93, 94]. The catalytic activity of Ce<sub>x</sub>Zr<sub>1-x</sub>O<sub>2</sub> solid solutions is adjustable through tuning the acid-base characteristics with varying Ce/Zr ratios. Moreover, due to the different charges and ionic radii of Ce<sup>4+</sup> (0.097 nm) and Zr<sup>4+</sup> (0.084 nm) cations, the acid strength of mixed oxides may change. For instance, Zr<sup>4+</sup> with the smaller ionic radius exhibits a more acidic nature than Ce<sup>4+</sup> in Ce<sub>x</sub>Zr<sub>1-x</sub>O<sub>2</sub> solid solutions [95]. However, a concentration balance between the basic and acidic centers on the catalyst's surface is also known to be crucial in the direct synthesis of DMC [82, 83]. In order to further promote these key properties Ikeda *et al.* performed surface modifications of ZrO<sub>2</sub> with phosphoric acid [96]. The authors claimed that both ZrO<sub>2</sub> and ZrO<sub>2</sub>/H<sub>3</sub>PO<sub>4</sub> had Lewis acid sites (Zr<sup>4+</sup>), whereas only ZrO<sub>2</sub>/H<sub>3</sub>PO<sub>4</sub> had weak Brønsted acid sites. From the reaction mechanism proposed by Ikeda *et al.* they claimed that in the last step of DMC formation, activation of MeOH was more favorable on the Brønsted acid sites than on the Lewis acid sites. In the research group of Wu *et al.* V<sub>2</sub>O<sub>5</sub> catalyst was also modified by phosphoric acid and applied for DMC synthesis [97]. The results showed an increase in DMC yield with increasing P/V ratio. Such improved catalytic performance was also attributed to the formation of weak Brønsted acid sites by interaction between V and P. In the case of ZrO<sub>2</sub>/H<sub>3</sub>PO<sub>4</sub> catalyst, the Brønsted acid sites on ZrO<sub>2</sub>/H<sub>3</sub>PO<sub>4</sub> were responsible for methanol

activation. Another well-known method to enhance the surface acidity is the modification with sulfate ions (super acidic catalyst) [98]. However, it is known that the catalytic activity of unmodified  $\text{Ce}_x\text{Zr}_{1-x}\text{O}_2$  is reduced to some extent by the presence of strong acid sites on the surface of the catalysts [99].

### 1.3.2. Suitable catalysts for DEC synthesis

Based on the results shown in Tables A1.1, A1.2 and A1.3, it is obvious that only a few efforts are being made to develop suitable catalysts for the direct synthesis of DEC from ethanol and carbon dioxide. However, the majority of these efforts were focused mainly on batch processes. According to the Tables A1.1 and A1.2, attempts to use continuous process(es) for DEC production from ethanol are very rare. In addition, the synthesis of DEC certainly allows  $\text{CO}_2$  to be used as a valuable and renewable relatively low-cost feedstock. Until now, a wide range of heterogeneous catalytic systems have been studied for this reaction. For instance,  $\text{CeO}_2$  [99-105],  $\text{K}_2\text{CO}_3\text{-C}_2\text{H}_5\text{I}$  [30],  $\text{CeO}_2/\text{SBA-15}$  [102],  $\text{Nb}_2\text{O}_5/\text{CeO}_2$  [106],  $\text{Cu-Ni/AC}$  [31],  $\text{Ce-H-MCM-41}$  [29],  $\text{Cu-Cl}$  [107],  $\text{CeO}_2\text{-ZrO}_2$  are some of the most widely used catalyst compositions so far. In addition, several homogeneous catalysts such as  $\text{KI/EtONa}$  [72] and metal tetra-alkoxides [70, 72] were found to be effective for one-pot DEC synthesis. Among them, literature reports indicate that Ce-Zr-O solids are most effective catalysts [94, 99, 100]. The catalytic activity of Ce-Zr-O towards DEC production was ascribed to the presence of acid-base sites on the surface, which consist of coordinatively unsaturated metal cations  $\text{M}^{4+}$  (Lewis acid-electron acceptors), lattice oxygen  $\text{O}^{2-}$  (Lewis base-electron donors) and hydroxyl groups probably acting as Brønsted basic centers during water formation [27, 99]. It has been proposed that dissociation of adsorbed ethanol leads to the formation of ethoxide group on the acid sites of the catalyst accompanied by a proton release, which reacts with a surface hydroxyl group to produce water.  $\text{CO}_2$  is then inserted into the M-O bond of the  $\text{C}_2\text{H}_5\text{O-M}$  species to produce the reaction intermediate  $\text{m-C}_2\text{H}_5\text{OCOO-M}$ . This process is facilitated by interactions of C and O atoms with Lewis acid-base pairs, i.e.  $\text{O}^{2-}\text{-M}^{4+}\text{-O}^{2-}$ . Monoethyl carbonate species react with activated ethanol on the acid sites of the catalyst to produce DEC [87, 108, 109]. It was suggested that high selectivity to DEC is due to rapid conversion of the ethoxide species to ethyl carbonate species under high  $\text{CO}_2$  pressure.

### 1.3.3. Thermodynamic restrictions

In spite of the obvious environmentally-friendly synthesis route, some additional difficulties of the direct synthesis of carbonate esters from alcohols and CO<sub>2</sub> also need to be taken into account. For instance, the activation of carbon dioxide is very difficult due to the fact that CO<sub>2</sub> is highly thermodynamically stable and kinetically inert. In addition, direct synthesis of dialkyl carbonates from alcohols and CO<sub>2</sub> shows some thermodynamic (equilibrium) limitations and therefore the yields of DEC and DMC to be achieved are expected to be relatively low in the absence of dehydrating agent. Thermodynamically possible yield of dialkyl carbonate is in a range of 1-2%, depending on reaction temperature and pressure. The formation of H<sub>2</sub>O as a by-product shifts the equilibrium towards the reactants side. Several studies described some ways to overcome this problem (Table A1.3), e.g. usage of certain chemical reagents or absorbents for instance butylene oxide [29, 88, 102], benzonitrile [110], acetals or ketals [71, 76, 78, 79, 94], acetonitrile [104] and also inorganic absorbents like zeolites [77], might be helpful to remove H<sub>2</sub>O from the product stream during the course of the reaction. The use of acetals as dehydrating agents over Bu<sub>2</sub>Sn(OMe)<sub>2</sub> catalyst leads to high yield of DMC ( $Y_{\text{DMC}} = 70\%$ ), however high CO<sub>2</sub> pressure (2000 bar) is required in order to avoid side reactions [25]. Choi *et al.* used inorganic dehydrating agent and reached high DMC yield (~50%) by removing the water with molecular sieve 3A in an external cooled loop [77]. However, this route has not been explored due to an extra consumption of energy for cooling the loop. Alternatively, Dibenedetto *et al.* [106] used a polymeric organic membrane PERVAP 1211 to remove the water formed during the reaction. Unfortunately, this effort was not successful due to problem that the reaction mixture cannot be directly separated as DEC passes through the membrane since it is permeable at concentrations above 0.3%. Nevertheless, in the work of Li *et al.* [89] three types of supported membranes (mesoporous silica, polyimide silica and polyimide-titania hybrid membrane) were applied for the synthesis of dimethyl carbonate (DMC) from methanol and CO<sub>2</sub>. Even though, the use of such membranes considerably improved DMC formation, however, the capability of dehydration at high pressure and temperature was reported to be very low.

### 1.3.4. Phase behavior of the CO<sub>2</sub> + EtOH system

Carbon dioxide has a low critical temperature ( $T_{cr} = 31.04\text{ }^{\circ}\text{C}$ ) and pressure ( $p_{cr} = 72.9\text{ bar}$ ). However, the addition of alcohols to CO<sub>2</sub> causes a variation of the critical properties  $T_{cr}$ ,  $p_{cr}$ ,  $\rho_{cr}$  and of phase diagram of the resultant CO<sub>2</sub>-alcohol mixture. For instance, the addition of 4.8 mol% MeOH to CO<sub>2</sub> causes to increase of  $T_{cr}$  of CO<sub>2</sub>-MeOH by 39% and to increase of  $P_{cr}$  by a factor of 2.2, compared to pure CO<sub>2</sub>. [111]. Since the present study was mainly focused on diethyl carbonate synthesis, the phase behavior of CO<sub>2</sub> + EtOH system at different temperatures and pressure is further described in detail. The critical points ( $p_{cr}$ ,  $T_{cr}$ ) for the C<sub>2</sub>H<sub>5</sub>OH-CO<sub>2</sub> binary system were studied by various researchers in the past, such as by Backer [112], Takishima [113], Lim [114], Yeo [115] and Galicia-Luna *et al.* [116, 117]. As can be seen in Fig. 1.4a, the supercritical region for C<sub>2</sub>H<sub>5</sub>OH-CO<sub>2</sub> binary system is reached maximum near 160 bar and temperature in a range of 120-160 °C when initial CO<sub>2</sub> molar fraction in such system is between 0.7 and 0.9. Moreover, the larger the ethanol concentration in the feed mixture, the higher the required temperature to reach the critical point is. Based on such reports, I suppose that these trends are still valid for quaternary system, due to the low amounts of DEC (predicted  $x \sim 0.004$  at reaction equilibrium) and H<sub>2</sub>O (predicted  $x \sim 0.004$  at reaction equilibrium). One can also expect that above 160 bar the reaction mixture might be in the liquid or supercritical state, depending upon the system temperature. Based on the literature [68, 106], in order to reach a higher ethanol conversion with respect to using liquid ethanol pressurized by CO<sub>2</sub> the use of supercritical conditions is required. I supposed that under supercritical conditions, EtOH and CO<sub>2</sub> are in a single phase and the effect of solubility-dependent concentration of CO<sub>2</sub> in the liquid phase is cancelled out. Cai *et al.* [118] and Leino *et al.* [26] showed in their theoretical studies for DMC synthesis that the relatively high DMC formation had been partly attributed to the fact that reaction becomes thermodynamically favourable as the system pressure increases. The experimental data are confirmed that an increase in the pressure from 45 bar to 200 bar improved the yield of DMC from 0.14 mol% to 0.20 mol%, respectively, at relatively low reaction temperature of 170 °C.

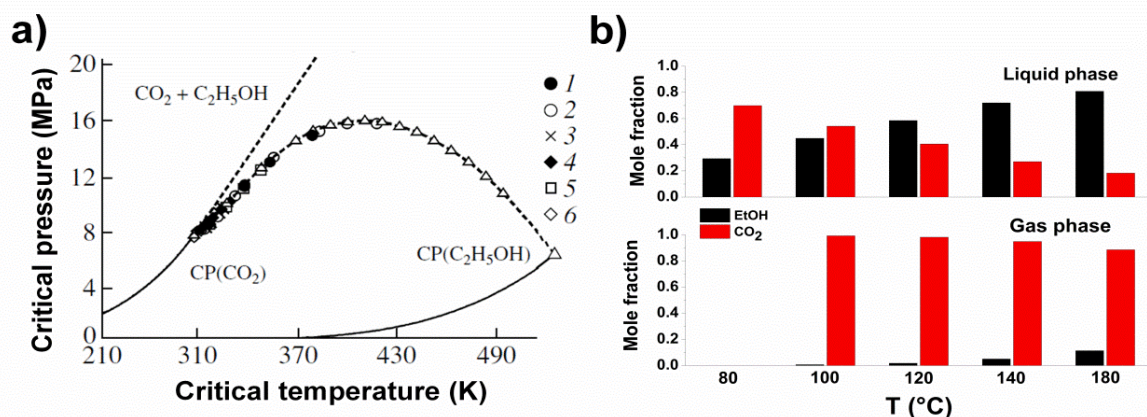


**Figure 1.4.** (a) Critical parameters for CO<sub>2</sub>-C<sub>2</sub>H<sub>5</sub>OH mixture reported by several authors: 1-[116], 2-[115], 3-[112], 4-[119], 5-[114], 6-[113] (reprinted from [111]). \*CP- supercritical parameters of pure components; (b) Ethanol and CO<sub>2</sub> concentrations in the C<sub>2</sub>H<sub>5</sub>OH-CO<sub>2</sub> system in vapor-liquid equilibria at: p = 140 bar, T = 80, 100, 120, 140, 180 °C and molar EtOH : CO<sub>2</sub> = 30 : 70.

A group contribution equation of state called PSRK (Predictive Soave-Redlich-Kwong) [120] has been applied to describe vapor-liquid equilibrium (VLE) of quaternary mixture, containing C<sub>2</sub>H<sub>5</sub>OH-CO<sub>2</sub>-C<sub>5</sub>H<sub>10</sub>O<sub>3</sub>-H<sub>2</sub>O. VLE were measured at 80, 100, 120, 140, 180 °C and at high pressure (80-200 bar). The general form of SRK (Soave-Redlich-Kwong) equation can be written as follows:

$$P = \frac{RT}{(V-b)} + \frac{a \alpha(T_r)}{V(V+b)} \quad (\text{Equation 1.1})$$

The calculation of thermodynamic parameters under the temperatures 80-180 °C and the pressures 80-200 bar is used to predict the maximum DEC yields under selected reaction conditions (Table 1.4). It is noted, that in the C<sub>2</sub>H<sub>5</sub>OH-CO<sub>2</sub>-C<sub>5</sub>H<sub>10</sub>O<sub>3</sub>-H<sub>2</sub>O system vapor-liquid two phases exist.

**Table 1.4.** Maximal thermodynamically possible DEC yields at equilibrium for several reaction conditions at a constant molar ratio of EtOH : CO<sub>2</sub> of 30 : 70.

T→	80		140		180		200	
p↓	Liquid	Vapor	Liquid	Vapor	Liquid	Vapor	Liquid	Vapor
<b>80</b>	0.8	0.1	1.1	0	1.1	0	1.1	0
<b>100</b>	0.6	0.1	0.9	0.1	1.1	0	1.1	0
<b>120</b>	0.5	0.1	0.8	0.2	0.8	0.2	1.0	0.2
<b>150</b>	0.5	0.1	0.6	0.1	0.7	0.1	0.8	0.1
<b>180</b>	0.5	0.1	0.5	0.1	0.6	0.1	0.6	0.1

To illustrate the effect of temperature on the concentration of ethanol and CO<sub>2</sub>, mole fractions of ethanol and CO<sub>2</sub> in gas and liquid phase at 140 bar are plotted in Figure 1.4b. It clearly seen, that ethanol concentrated in liquid phase and as temperature increases, the highest attainable ethanol concentration increases. These results are in a good agreement with those published by J. S. Lim [114]. He described a high pressure vapour-liquid equilibrium for CO<sub>2</sub>-C<sub>2</sub>H<sub>5</sub>OH system with a wide range of ethanol concentration and found the similar effect of temperature on the ethanol concentration.

#### 1.4. Motivation and objectives of the thesis

The global warming from the emission of greenhouse gases has received worldwide interest in the recent years. Among several greenhouse gases, CO<sub>2</sub> contributes over 72% to global warming due to its huge emission amount over 37 Gt CO<sub>2</sub> per year. This is also indicated by increased atmospheric CO<sub>2</sub> concentration, which has risen from about 280 ppm (1850) to 411 ppm (February 2019). The utilization of CO<sub>2</sub> to produce various commercially important chemicals over heterogeneous catalysts is one of the efficient pathways to reduce CO<sub>2</sub> emissions, since the CO<sub>2</sub> is not only just a greenhouse gas, but also an important source of carbon in industry.

Among different chemicals that can be produced from CO<sub>2</sub> conversion, organic carbonates are special class of chemicals with high oxygen content that are used in various sectors. The traditional route to produce organic carbonates is to use the extremely toxic phosgene (Bayer process). In terms of safety and environment concerns, the replacement of hazardous phosgene route by CO<sub>2</sub> is highly concerned, encouraged and also attracted the scientific interest. The organic carbonates, such as dimethyl carbonate (DMC) and diethyl carbonate (DEC), are used as raw materials in a wide range of chemical reactions, for instance, as a precursor to synthesize polycarbonates, as electrolytes in lithium batteries and as solvent due to their high solubilizing power, exhibit relatively low toxicity and having suitable boiling point to be removed by vaporization. Furthermore, DEC/DMC can be used as an additive to diesel fuel due to their high oxygen content (40.6% for DEC and 53.3% for DMC) and high octane booster power ( $((R + M)/2 = 105$ , where R is the research octane number and M stands for motor octane number) to improve the performance of gasoline combustion.

The direct production of organic carbonates via reaction of CO<sub>2</sub> and alcohols is certainly attractive and promising way due to the conversion of CO<sub>2</sub> into valuable chemicals and is



"green" chemical process with many advantages. However, the amount of CO<sub>2</sub> consumption for generated chemicals is relatively small (only 110 Mt/y of CO<sub>2</sub> converted into organic and inorganic compounds) and is not enough to consume most of CO<sub>2</sub> produced. Therefore, there is a real need to convert CO<sub>2</sub> into various industrially important products, such as DMC and DEC.

However, there are three major problems of this reaction: i) thermodynamic limitations, ii) catalyst deactivation and iii) hydrolysis of the desired products by formed water. Therefore, achieving high yield of target product is difficult / very low (~1-2%) without water elimination during the course of the reaction. Within the project "Innovative homogen- und heterogenkatalysierte Reaktionen zur chemischen Umwandlung von CO<sub>2</sub>", the main task of our research group was developing effective catalysts and identifying suitable reaction conditions for the direct and continuous synthesis of dialkyl carbonates from CO<sub>2</sub> and C<sub>1</sub>-C<sub>2</sub> alcohols (methanol and ethanol). Water-removal approaches using inorganic membranes for the direct carboxylation of alcohols were designed and tested by other research group under the same project but with another Ph.D. student.

Thus, the main objective of the present study in general is to improve the yield of dialkyl carbonates from CO<sub>2</sub> and alcohols by means of developing i) effective catalyst compositions, ii) optimizing reaction conditions, iii) identifying key properties of the catalysts (e.g. acid-base functions, reducibility etc.), iv) ultimately establishing structure-performance relationships as required for tailored catalyst design. In particular, for direct and continuous synthesis of DEC the main goal is to evaluate the potential of catalysts in a continuous mode using a plug-flow reactor (PFR) to increase the DEC yield under suitable reaction conditions.

Pure CeO<sub>2</sub>, ZrO<sub>2</sub> and mixed Ce-Zr oxides are generally reported to be the most effective catalysts in the formation of dialkyl carbonates due to the presence of both acidic and basic sites in these solids. Even though Ce-Zr oxides are known from the literature, tuning their acid-base properties, their suitable modifications by means of different dopants and exploring their potential towards the desired reaction are still missing in the literature. With this background, we are motivated to systematically tune their catalytic properties by various means, e.g. by varying preparative methods, tuning Ce/Zr ratios, application of different dopants, varying calcination temperatures etc. and check their influence on the catalytic performance. As mentioned above, catalytic properties of various CeO<sub>2</sub>-ZrO<sub>2</sub> solid solutions can be adjusted through the ratio of Ce/Zr. Therefore, Ce<sub>x</sub>Zr<sub>1-x</sub>O<sub>2</sub> catalysts with different Ce/Zr ratios were synthesized in the frame of this work. Moreover, the effect of promoting of

CeO<sub>2</sub>-ZrO<sub>2</sub> with an acidic compound, e.g. phosphoric acid, was also investigated with the purpose to check if the yield of DMC can be increased through accelerating DMC formation step.

In order to achieve the above mentioned goals, this thesis focuses on the following aspects:

- i) to synthesize and apply Ce<sub>x</sub>Zr<sub>1-x</sub>O<sub>2</sub> catalysts with different Ce content for the one-pot synthesis of organic carbonates from CO<sub>2</sub> and alcohols and find out optimum Ce content.
- ii) to perform surface modifications of previously optimized Ce-Zr-O composition (e.g. Ce<sub>0.8</sub>Zr<sub>0.2</sub>O<sub>2</sub> catalyst) with a phosphoric acid and also to investigate the effect of such modification through varying P-contents in Ce<sub>0.8</sub>Zr<sub>0.2</sub>O<sub>2</sub> with the aim to identify efficient catalyst composition for direct synthesis of DMC from CO<sub>2</sub> and methanol.
- iii) to gain deeper insights into the key catalytic properties, the catalysts were characterized by means of various physico-chemical techniques such as N<sub>2</sub> physisorption, ICP-OES, BET, XRD, XPS, H<sub>2</sub>-TPR, TEM, In situ FTIR, NH<sub>3</sub>- and CO<sub>2</sub>-TPD. The obtained results were related to catalytic activity towards dialkyl carbonates production.
- iv) to design continuous flow system and to determine optimal reaction conditions for direct DEC synthesis from CO<sub>2</sub> and ethanol, i.e. to investigate the effect of each parameter (e.g. temperature, pressure, EtOH : CO<sub>2</sub> ratios and LHSV) on DEC yield.

## Chapter 2

### **2. Experimental section: Preparation, testing and characterization methods**

*Chapter 2 represents the detailed procedure for the preparation of  $Ce_xM_{1-x}O_2$  materials: various Ce/M ratios, preparation methods, surface modification etc. The necessary theoretical background of different characterization methods is also given. The experimental set-ups and reaction procedures are described in detail.*

## 2.1. Catalyst preparation

### 2.1.1. Chemicals

For catalyst preparation  $\text{Ce}(\text{NO}_3)_3 \cdot 6\text{H}_2\text{O}$  (99.5%, Acros),  $\text{ZrO}(\text{NO}_3)_2 \cdot x\text{H}_2\text{O}$  (99%, technical grade),  $\text{ZrOCl}_2 \cdot 8\text{H}_2\text{O}$  (99.5%, Sigma-Aldrich), anhydrous hafnium nitrate ( $\text{Hf}(\text{NO}_3)_4$ , Sigma-Aldrich, 99.9%), titanium tetrachloride (99.9%  $\text{TiCl}_4$ , Aldrich), oxalic acid-dihydrate (98%  $\text{C}_2\text{O}_4\text{H}_2 \cdot 2\text{H}_2\text{O}$ , Alfa Aesar), phosphoric acid (85%  $\text{H}_3\text{PO}_4$ , Roth), nitric acid (65%  $\text{HNO}_3$ , Roth), citric acid (99%  $\text{C}_6\text{H}_8\text{O}_7$ , Sigma-Aldrich) and aqueous ammonium hydroxide (25%, Roth) were used. All used solvents were of analytical grade.

### 2.1.2. Citrate complexation method

#### 2.1.2.1. $\text{Ce}_x\text{Zr}_{1-x}\text{O}_2$ solids

For the correct calculation of the specific  $\text{Ce}_x\text{Zr}_{1-x}\text{O}_2$  stoichiometries the determination of  $x$  in  $\text{ZrO}(\text{NO}_3)_2 \cdot x\text{H}_2\text{O}$  is absolutely essential.  $x$  was calculated from the thermal decomposition of the Zr precursor studied by TG under air.  $x$  was calculated with  $\sim 4$ . Hence, the molar composition was  $\text{ZrO}(\text{NO}_3)_2 \cdot 4\text{H}_2\text{O}$ . The detailed explanation is given in Appendix (section A2.1).  $\text{Ce}_x\text{Zr}_{1-x}\text{O}_2$  solids with  $x = 0, 0.2, 0.5, 0.8$  or  $1.0$  (catalysts for Chapter 4) were prepared by a citric acid complexation method according to Alifanti *et al.* [121].  $\text{ZrO}(\text{NO}_3)_2 \cdot 4\text{H}_2\text{O}$  and  $\text{Ce}(\text{NO}_3)_3 \cdot 6\text{H}_2\text{O}$  in desired quantities were dissolved in deionized water yielding a 0.1 M solution (Table 2.1).

**Table 2.1.** The synthesis conditions for different  $\text{Ce}_x\text{Zr}_{1-x}\text{O}_2$  catalysts prepared by citrate complexation method.

Catalyst	Code	$\text{Ce}(\text{NO}_3)_3 \cdot 6\text{H}_2\text{O}$ (g)	$\text{ZrO}(\text{NO}_3)_2 \cdot 4\text{H}_2\text{O}$ (g)	$\text{C}_6\text{H}_8\text{O}_7$ (g)	Drying ( $T_D/t$ )	Calcination ( $T_C/\text{atm./t}$ )
$\text{CeO}_2$	C-citrate	15.5	-	7.5	70 °C/16h	450 °C/air/3h
$\text{Ce}_{0.8}\text{Zr}_{0.2}\text{O}_2$	C80Z-citrate	15.5	2.7	9.4	70 °C/16h	450,700, 1000 °C/air/3h
$\text{Ce}_{0.8}\text{Zr}_{0.2}\text{O}_2$	C80Z-1 <sup>a</sup>	15.5	2.7	9.4	70 °C/16h	700 °C/air/3h
$\text{Ce}_{0.5}\text{Zr}_{0.5}\text{O}_2$	C50Z-citrate	15.5	10.8	15.1	70 °C/16h	450 °C/air/3h
$\text{Ce}_{0.2}\text{Zr}_{0.8}\text{O}_2$	C20Z-citrate	15.5	43.3	37.7	70 °C/16h	450 °C/air/3h
$\text{ZrO}_2$	Z-citrate	-	43.3	30.2	70 °C/16h	450 °C/air/3h

<sup>a</sup>  $\text{C}_2\text{H}_5\text{OH}$  was used as a solvent during preparation instead of  $\text{H}_2\text{O}$

Citric acid was added in 10 mol% excess for complete complexation of metal cations. The mixture was stirred at room temperature for 2 hours. The excess solvent was removed on a

rotary evaporator. The obtained solid was dried overnight (16 h) under vacuum at 70 °C. The precursors were calcined at 450 °C for 3 h in air (heating rate of 2 K min<sup>-1</sup>, air flow of 60 mL min<sup>-1</sup>). In total five different Ce<sub>x</sub>Zr<sub>1-x</sub>O<sub>2</sub> catalysts with varying Ce contents of 0, 20, 50, 80, 100 mol% were prepared and they are denoted as Z-citrate (pure zirconia), C20Z-citrate, C50Z-citrate, C80Z-citrate and C-citrate (pure ceria), respectively. Another batch of C80Z-citrate was calcined in air separately at 700 or 1000 °C for 3 h.

### 2.1.2.2. Ce<sub>0.8</sub>Ti<sub>0.2</sub>O<sub>2</sub> solids

The Ce<sub>0.8</sub>Ti<sub>0.2</sub>O<sub>2</sub> catalyst was prepared by citrate complexation method in analogy to section 2.1.2.1. Cerium nitrate hexahydrate and titanyl nitrate (Table 2.2) were used as Ce and Ti precursors. Based on the fact that titanyl nitrate is not commercially available, TiO(NO<sub>3</sub>)<sub>2</sub> [122] was prepared and used as precursor for Ce<sub>0.8</sub>Ti<sub>0.2</sub>O<sub>2</sub> (See Appendix A2.2).

**Table 2.2.** Pure TiO<sub>2</sub> and Ce<sub>0.8</sub>Ti<sub>0.2</sub>O<sub>2</sub> catalysts prepared by citrate complexation method.

Catalyst	Code	Ce(NO <sub>3</sub> ) <sub>3</sub> ·6H <sub>2</sub> O (g)	TiO(NO <sub>3</sub> ) <sub>2</sub> (g)	C <sub>6</sub> H <sub>8</sub> O <sub>7</sub> (g)	Drying (T <sub>D</sub> /t)	Calcination (T <sub>c</sub> /atm./t)
Ce <sub>0.8</sub> Ti <sub>0.2</sub> O <sub>2</sub>	C80T-citrate	7.7	0.4	4.1	70 °C/16h	700 °C/air/3h
TiO <sub>2</sub>	T-citrate	-	8.5	20	70 °C/16h	700 °C/air/3h

### 2.1.2.3. Ce<sub>0.8</sub>Hf<sub>0.2</sub>O<sub>2</sub> solids

The Ce<sub>0.8</sub>Hf<sub>0.2</sub>O<sub>2</sub> catalyst was prepared by citrate complexation method using the procedure described in section 2.1.2.1. Cerium nitrate hexahydrate and anhydrous hafnium nitrate were used as Ce and Hf precursors (Table 2.3).

**Table 2.3.** Pure HfO<sub>2</sub> and Ce<sub>0.8</sub>Hf<sub>0.2</sub>O<sub>2</sub> catalysts prepared by citrate complexation method.

Catalyst	Code	Ce(NO <sub>3</sub> ) <sub>3</sub> ·6H <sub>2</sub> O (g)	Hf(NO <sub>3</sub> ) <sub>3</sub> (g)	C <sub>6</sub> H <sub>8</sub> O <sub>7</sub> (g)	Drying (T <sub>D</sub> /t)	Calcination (T <sub>c</sub> /atm./t)
Ce <sub>0.8</sub> Hf <sub>0.2</sub> O <sub>2</sub>	C80H-citrate	15.49	3.8	9.4	70 °C/16h	700 °C/air/3h
HfO <sub>2</sub>	H-citrate	-	8.5	6.1	70 °C/16h	700 °C/air/3h

### 2.1.3. Ce<sub>0.8</sub>Zr<sub>0.2</sub>O<sub>2</sub> solid solutions prepared by co-precipitation

Ce<sub>0.8</sub>Zr<sub>0.2</sub>O<sub>2</sub> (catalyst used in Chapter 6) was prepared by a co-precipitation method with aqueous solutions of ZrOCl<sub>2</sub>·8H<sub>2</sub>O (0.1M) and Ce(NO<sub>3</sub>)<sub>3</sub>·6H<sub>2</sub>O (0.36M) using aqueous

ammonium hydroxide (6 vol.%) as a precipitating agent (Table 2.4) [99]. pH value during this procedure (addition of  $\text{NH}_4\text{OH}$ ) was controlled to be about 10. The resultant precipitate was collected and washed with deionized water until  $\text{Cl}^-$  species were no longer detectable as  $\text{AgCl}$  precipitate via titration with  $\text{AgNO}_3$  solution. The product precipitate was dried at  $120\text{ }^\circ\text{C}$  overnight and calcined at  $700\text{ }^\circ\text{C}$  for 3 hours in air (heating rate of  $2\text{ K min}^{-1}$ , air flow of  $60\text{ mL min}^{-1}$ ).

**Table 2.4.**  $\text{Ce}_{0.8}\text{Zr}_{0.2}\text{O}_2$  catalyst prepared by co-precipitation method.

Catalyst	Code	$\text{Ce}(\text{NO}_3)_3 \cdot 6\text{H}_2\text{O}$ (g)	$\text{ZrOCl}_2 \cdot 8\text{H}_2\text{O}$ (g)	Drying ( $T_D/t$ )	Calcination ( $T_C/\text{atm./t}$ )
$\text{Ce}_{0.8}\text{Zr}_{0.2}\text{O}_2$	C80Z-2	15.49	2.9	$120\text{ }^\circ\text{C}/16\text{h}$	$700\text{ }^\circ\text{C}/\text{air}/3\text{h}$

### 2.1.4. $\text{Ce}_x\text{Zr}_{1-x}\text{O}_2$ via oxalate gel co-precipitation method

The preparation of  $\text{Ce}_x\text{Zr}_{1-x}\text{O}_2$  solids (with  $x = 0, 0.2, 0.4, 0.6, 0.8$  and  $1.0$ ) was carried out by an oxalate gel co-precipitation method (catalysts for Chapter 3) [123]. For each synthesis, following two solutions were prepared: i) desired amounts of  $\text{Ce}(\text{NO}_3)_3 \cdot 6\text{H}_2\text{O}$  and  $\text{ZrO}(\text{NO}_3)_2 \cdot 4\text{H}_2\text{O}$  were dissolved in 65 ml of ethanol and ii) 6 g of oxalic acid in 48 ml of ethanol (1M solution) (Table 2.5).

**Table 2.5.** List of  $\text{Ce}_x\text{Zr}_{1-x}\text{O}_2$  catalysts prepared by oxalate gel co-precipitation method.

Catalyst	Code	$\text{Ce}(\text{NO}_3)_3 \cdot 6\text{H}_2\text{O}$ (g)	$\text{ZrO}(\text{NO}_3)_2 \cdot 4\text{H}_2\text{O}$ (g)	Drying ( $T_D/t$ )	Calcination ( $T_C/\text{atm./t}$ )
$\text{CeO}_2$	$\text{C}^{\text{prec}}$	4.3	-	$70\text{ }^\circ\text{C}/16\text{h}$	$600\text{ }^\circ\text{C}/\text{air}/4\text{hr}$
$\text{Ce}_{0.8}\text{Zr}_{0.2}\text{O}_2$	$\text{C80Z}^{\text{prec}}$	17.4	3.03	$70\text{ }^\circ\text{C}/16\text{h}$	$600\text{ }^\circ\text{C}/\text{air}/4\text{h}$
$\text{Ce}_{0.6}\text{Zr}_{0.4}\text{O}_2$	$\text{C60Z}^{\text{prec}}$	6.5	3.03	$70\text{ }^\circ\text{C}/16\text{h}$	$600\text{ }^\circ\text{C}/\text{air}/4\text{h}$
$\text{Ce}_{0.4}\text{Zr}_{0.6}\text{O}_2$	$\text{C40Z}^{\text{prec}}$	2.9	3.03	$70\text{ }^\circ\text{C}/16\text{h}$	$600\text{ }^\circ\text{C}/\text{air}/4\text{h}$
$\text{Ce}_{0.2}\text{Zr}_{0.8}\text{O}_2$	$\text{C20Z}^{\text{prec}}$	1.1	3.03	$70\text{ }^\circ\text{C}/16\text{h}$	$600\text{ }^\circ\text{C}/\text{air}/4\text{h}$
$\text{ZrO}_2$	$\text{Z}^{\text{prec}}$	-	3.03	$70\text{ }^\circ\text{C}/16\text{h}$	$600\text{ }^\circ\text{C}/\text{air}/4\text{h}$

Solution (ii) was added dropwise under vigorous stirring to solution (i) until complete precipitation. The obtained precipitate was stirred for additional 2 hours, filtered and dried overnight (16 h) at  $70\text{ }^\circ\text{C}$ . Afterwards, the received powders were calcined at  $600\text{ }^\circ\text{C}$  for 4 hours (heating rate of  $1.67\text{ K min}^{-1}$ , air flow of  $100\text{ mL min}^{-1}$ ). The received  $\text{Ce}_x\text{Zr}_{1-x}\text{O}_2$  catalysts were denoted as  $\text{Z}^{\text{prec}}$  (pure zirconia),  $\text{C20Z}^{\text{prec}}$ ,  $\text{C40Z}^{\text{prec}}$ ,  $\text{C60Z}^{\text{prec}}$ ,  $\text{C80Z}^{\text{prec}}$  (40, 60, 80 mol% Ce) and  $\text{C}^{\text{prec}}$  (pure ceria).

### 2.1.5. Phosphated $\text{Ce}_x\text{Zr}_{1-x}\text{O}_2$ : co-precipitation and wet impregnation

$\text{Ce}_x\text{Zr}_{1-x}\text{O}_2/\text{H}_3\text{PO}_4$  ( $x = 0.8$ ) solid solutions were prepared in two steps according to previously reported protocols [96, 124]. First, Ce-Zr hydroxide were prepared at room temperature from ethanolic solutions of  $\text{ZrO}(\text{NO}_3)_2 \cdot 4\text{H}_2\text{O}$  and  $\text{Ce}(\text{NO}_3)_3 \cdot 6\text{H}_2\text{O}$  in desired quantities using aqueous ammonium hydroxide (6 vol.%) as precipitating agent (Table 2.6). pH value at the end of the procedure was about 9. The resultant precipitate was washed three times with deionized water and then dried at 120 °C for 12 hours.

**Table 2.6.** Ce-Zr precursor prepared by precipitation method.

Precursor	$\text{Ce}(\text{NO}_3)_3 \cdot 6\text{H}_2\text{O}$ (g)	$\text{ZrO}(\text{NO}_3)_2 \cdot 4\text{H}_2\text{O}(\text{g})$	Drying ( $T_D/t$ )
$(\text{Ce}_{0.8}\text{Zr}_{0.2})\text{OH}$	17.4	3.03	120 °C/12h

$\text{Ce}_{0.8}\text{Zr}_{0.2}\text{O}_2/\text{H}_3\text{PO}_4$  catalysts were prepared by impregnation of 0.06M aqueous  $\text{H}_3\text{PO}_4$  on Ce-Zr hydroxides with different P/Zr ratios of 0.03 (C80ZP-1), 0.12 (C80ZP-2), 0.3 (C80ZP-3) (Table 2.7).

**Table 2.7.** List of  $\text{Ce}_x\text{Zr}_{1-x}\text{O}_2$  catalysts treated with  $\text{H}_3\text{PO}_4$ .

Catalyst	Code	V of 0.06M $\text{H}_3\text{PO}_4$ (mL) for 1g of Zr	P/Zr	Drying ( $T_D/t$ )	Calcination ( $T_C/\text{atm.}/t$ )
$\text{Ce}_{0.8}\text{Zr}_{0.2}\text{O}_2/\text{H}_3\text{PO}_4$	C80ZP-1	6.5	0.03	120 °C/3h	600 °C/air/4h
$\text{Ce}_{0.8}\text{Zr}_{0.2}\text{O}_2/\text{H}_3\text{PO}_4$	C80ZP-2	26	0.12	120 °C/3h	600 °C/air/4h
$\text{Ce}_{0.8}\text{Zr}_{0.2}\text{O}_2/\text{H}_3\text{PO}_4$	C80ZP-3	65	0.3	120 °C/3h	600 °C/air/4h
$\text{Ce}_{0.8}\text{Zr}_{0.2}\text{O}_2/\text{H}_3\text{PO}_4$	C80ZP* <sup>a</sup>	26	0.12	120 °C/3h	600 °C/air/4h

<sup>a</sup> Post-treated sample

To investigate the effect of post-treatment, 0.06M aqueous  $\text{H}_3\text{PO}_4$  (P/Zr=0.12) was introduced directly to calcined  $\text{Ce}_{0.8}\text{Zr}_{0.2}\text{O}_2$  at 600 °C/air/4h (denoted as C80ZP\*). All treatments were performed under stirring for 1 hour at room temperature. The excess liquid was removed under vacuum on a rotavapor, the residue was dried for 3 hours at 120 °C and finally calcined at 600 °C for 4h ( $1.67 \text{ K min}^{-1}$ , airstream of  $100 \text{ mL min}^{-1}$ ).

## 2.2. Catalyst characterization

### 2.2.1. Thermogravimetric analysis (TGA)

Thermogravimetric analysis (TGA) is used to evaluate the thermal stability of materials and to determine the fraction of volatile components (e.g. moisture) during heating process. TGA has been performed in the temperature range between 27 and 1000 °C using a Netzsch STA 449F3 instrument. The heating rate was 10 K min<sup>-1</sup>. The measurements were carried out in synthetic air (80 mL min<sup>-1</sup>). 60 mg of the each sample was used for the analysis.

### 2.2.2 Nitrogen adsorption: BET and BJH methods

Physical adsorption of nitrogen is widely used for the determination of overall surface area and pore size distribution of various porous solids. The specific surface area is estimated by measuring the amount of adsorbed nitrogen at -196°C across a wide range of relative pressures. In present work the surface areas (SA) calculated according to the BET equation (Equation 2.1) and pore volumes of the samples obtained from BJH equation (Equation 2.2) were experimentally determined using a NOVA 4200e device (Quantachrome Instruments).

$$S_{BET} = \frac{V_m N_A A_m}{22414 W} \quad (\text{Equation 2.1})$$

$V_m$  = the monolayer volume at STP conditions (mL)

$N_A$  = Avogadro constant ( $6.022 \times 10^{23} \text{ mol}^{-1}$ )

$A_m$  = effective cross-sectional area of one adsorbate molecule (0.162 nm<sup>2</sup> for N<sub>2</sub>)

22414 = volume occupied by 1 mole of the adsorbate gas at STP (mL)

$W$  = the amount of the sample tested (grams).

$$r_k = \frac{-2\sigma V}{RT \ln(\frac{p}{p_0})} \quad (\text{Equation 2.2})$$

$r_k$  = Kelvin radius

$V$  = molar volume of liquid condensate

$\sigma$  = the surface tension of the liquid condensate.

Prior to each nitrogen sorption measurement, the samples were evacuated at 200 °C for 2 h to remove gases and vapours that may have become physically adsorbed on the surface during preparation and storage.



### 2.2.3 X-ray diffraction studies (XRD)

X-ray diffraction is used to determine the crystal structure, phase composition, lattice parameters, crystallite size and microstrain of solids. X-ray diffraction (XRD) studies described and discussed in Sections 4.1 and 5 were carried out on a X'Pert Pro diffractometer (Panalytical, Almelo, Netherlands) with CuK $\alpha$  radiation ( $\lambda = 1.5418 \text{ \AA}$ , 40 kV, 40 mA) and an X'Celerator RTMS detector. The phase composition of the samples was determined using the program suite WinXPOW by STOE & CIE with inclusion of the Powder Diffraction File PDF2 of the ICDD (International Centre of Diffraction Data). An average crystallite size ( $D$ ) was calculated using Scherrer equation [125]:

$$D = \frac{K\lambda}{\beta \cos \theta} \quad (\text{Equation 2.3})$$

$\lambda$  = X-ray wavelength (1.54  $\text{\AA}$  for CuK $\alpha$  radiation)

$K$  = Scherrer's constant of proportionality taken as 0.94

$\beta$  = full width at half maximum of the peak

$\theta$  = the diffraction angle

The detailed XRD analysis, recorded on a Bruker D8 Advance instrument in Bragg-Brentano mode with Cu K $\alpha$  radiation (1.54  $\text{\AA}$ , 40 kV and 40 mA) using a silicon single crystal as sample holder to minimize scattering, was described and discussed in sections 3, 4.2 and 6. For better homogenization, the dried powder samples were redispersed in ethanol and coated on a silicon surface. XRD patterns were recorded in the range from 5 to 90° 2 $\theta$  with a step of 0.01° 2 $\theta$  at a counting time of 0.6 s. For qualitative phase analysis with a Diffrac.Suite EVA V1.2 from Bruker the pattern of monoclinic ZrO<sub>2</sub> (#78-0047), tetragonal ZrO<sub>2</sub> (#79-1764), and cubic CeO<sub>2</sub> phase (#78-0694) from the ICDD database were used as references. Rietveld refinement with the program package TOPAS 4.2 from Bruker or Rietveld Quantitative Analysis was performed to determine the lattice parameters, the substitution in the unit cells, the weight amount of crystalline phases, the crystallographic density, the average crystallite sizes and microstrain. The breadth and position of diffraction peak can be affected by the defective crystal structure. This deviation from the crystallinity is caused by the lattice distortion due to the microstrain. The defects producing microstrains are dislocations, grain, sinter stresses and grain boundaries etc. The width of the diffraction peaks can vary due to the size of crystallite and crystalline defects. Thus, both microstrain and

crystallite size lead to peak broadening. The peak broadening due to microstrain ( $\varepsilon$ ) changes as

$$B(2\theta) = 4\varepsilon \frac{\sin\theta}{\cos\theta} \quad (\text{Equation 2.4})$$

compared to peak broadening due to crystallite size

$$B(2\theta) = \frac{K\lambda}{D\cos\theta} \quad (\text{Equation 2.5})$$

For each Rietveld refinement, the instrumental correction as determined with a standard powder sample LaB6 from NIST (National Institute of Standards and Technology) as standard reference material (SRM 660b;  $a(\text{LaB6})=4.15689 \text{ \AA}$ ) was taken into account.

#### 2.2.4 Inductively coupled plasma optical emission spectroscopy (ICP-OES)

For the determination of the elemental composition, a Varian 715-ES ICP-OES was used. Approximately 10 mg of the sample was mixed with 8 mL of aqua regia and 2 mL hydrofluoric acid. The acid digestion was performed in a microwave-assisted sample preparation system "MULTIWAVE PRO" from Anton Paar at  $\sim 200^\circ\text{C}$  and  $\sim 50$  bar pressure. The data analysis was performed on the Varian 715-ES software "ICP Expert".

#### 2.2.5 X-ray photoelectron spectroscopy (XPS)

X-ray photoelectron spectroscopy (XPS), also known as ESCA (electron spectroscopy for chemical analysis), is used to determine the composition of the catalysts in the near-surface-region due to shifts in the binding energies. XPS tests were carried out using a VG ESCALAB 220iXL instrument with monochromatic  $\text{AlK}\alpha$  radiation ( $E = 1486.6 \text{ eV}$ ). The samples were fixed by using a double adhesive carbon tape on a stainless steel sample holder. The peaks were fitted by Gaussian–Lorentzian curves following a Shirley background subtraction.

#### 2.2.6 Transmission electron microscopy (TEM)

Transmission Electron Microscopy (TEM) provides information on position of atoms in crystalline sample, morphology (size, shape, distributions) and elemental composition. TEM

investigations were carried out at 200 kV with an aberration-corrected JEM-ARM200F (JEOL, Corrector: CEOS). The aberration corrected STEM imaging (High-Angle Annular Dark Field (HAADF) and Annular Bright Field (ABF)) were done with a spot size of approximately 0.13 nm, a convergence angle of 30–36° and collection semi-angles for HAADF and ABF of 90–170 mrad and 11–22 mrad, respectively. The microscope is equipped with a JED-2300 (JEOL) energy-dispersive X-ray-spectrometer (EDXS) for chemical analysis. Samples were prepared by depositing without any pre-treatment on a holey carbon supported Cu-grid (mesh 300) and transferred to the microscope.

### **2.2.7 Temperature-programmed reduction (TPR) using H<sub>2</sub> as the reduction agent**

Temperature programmed reduction (TPR) is a useful technique to obtain information on the reducibility of solid oxide materials. TPR profiles were recorded in a temperature range from RT to 800 °C at a heating rate of 5 K min<sup>-1</sup> on a Micromeritics AC2920 instrument. This instrument mainly consists of a fixed-bed reactor in a furnace and a thermal conductivity detector (TCD) for determination of gas composition. The temperature of reaction is controlled by thermocouple located in the catalyst bed. The H<sub>2</sub> concentration in a gas stream is monitored continuously using TCD with a linear temperature ramp of e.g. 5 K min<sup>-1</sup>. The obtained TPR profiles are used to determine an overall amount of H<sub>2</sub> consumed and temperature of maximal H<sub>2</sub> consumption. Prior to TPR measurements, all the samples were pretreated with 5% H<sub>2</sub>/Ar at room temperature for 10 min. For each H<sub>2</sub>-TPR experiment 0.1-0.2 g of powder is used.

### **2.2.8 Temperature programmed desorption (TPD) using NH<sub>3</sub> as basic probe and CO<sub>2</sub> as acidic probe**

Temperature programmed desorption (TPD) techniques are important methods for determination of acidic and basic properties (strength and number of acid-base sites) of catalyst. In this method, acidic (e.g. carbon dioxide) or basic molecular probes (e.g. ammonia) are adsorbed on the basic or acidic sites of solids, respectively. TPD of ammonia (TPD-NH<sub>3</sub>) or carbon dioxide (TPD-CO<sub>2</sub>) were carried out in a homemade apparatus consisting of a gas flow system, a high temperature oven and a quartz reactor. For determination of overall concentration of acid sites and their distribution, the samples (0.1–0.2 g) were treated in nitrogen at 400 °C for 30 min to remove moisture and cooled down to 100 °C in He of high

purity (6.0) prior to  $\text{NH}_3$  adsorption, which was carried out at 100 °C for 30 min in a flow of 5%  $\text{NH}_3/\text{He}$ . Afterwards, the TPD- $\text{NH}_3$  experiments were carried out from 100 to 450 °C in He flow ( $50 \text{ cm}^3 \text{ min}^{-1}$ ) with a heating rate of  $10 \text{ K min}^{-1}$ . The reaction temperature was continuously controlled by a thermocouple placed inside the catalyst bed. Desorption of  $\text{NH}_3$  was monitored and evaluated by a thermal conductivity detector (TCD, GOW-Mac Instrument Co.). For determination of basic properties, the sample (0.2 g) was treated in He ( $50 \text{ mL min}^{-1}$ ) at 500 °C with a heating rate of  $10 \text{ K min}^{-1}$  for 15 min (for the removal of adsorbed water) and cooled down to 100 °C in He ( $50 \text{ mL min}^{-1}$ ) prior to  $\text{CO}_2$  adsorption, which was carried out at 100 °C for 90 min in a flow of 1.2%  $\text{CO}_2\text{--He}$  mixture. Afterwards, the TPD- $\text{CO}_2$  experiments were carried out in He flow ( $50 \text{ mL min}^{-1}$ ) at 100 °C for 30 min (for removal of physisorbed  $\text{CO}_2$ ). After cooling to 70 °C for 10 min, the sample was heated up to 800 °C at a rate of  $10 \text{ K min}^{-1}$  in a helium flow ( $50 \text{ mL min}^{-1}$ ). The analysis of the effluent gases was performed by Quadrupole mass spectrometer (Balzers Omnistar).

### 2.2.9 Fourier Transform Infrared Spectroscopy (FTIR)

*In situ* FTIR spectroscopy is widely used to study surface properties of solid samples through the adsorption of probe molecules and to characterize/identify reaction intermediates on its surfaces. In this work methanol and carbon dioxide were selected as probe molecules since they are the feed components in the studied reaction. *In situ* FTIR measurements were carried out in transmission mode on a Bruker Tensor 27 spectrometer equipped with a heatable and evacuable homemade reaction cell with  $\text{CaF}_2$  windows connected to a gas-dosing and evacuation system. The powder was pressed into self-supporting wafer with a diameter of 20 mm and a weight of 50 mg. Before  $\text{MeOH}/\text{CO}_2$  adsorption, the samples were pretreated in synthetic air by heating up to 400 °C for 10 min, cooled down to 170 °C and a spectrum was recorded. Then  $\text{MeOH}/\text{CO}_2$  (saturator, RT;  $50 \text{ mL min}^{-1} \text{ CO}_2$ ) was adsorbed at this temperature for 30 min. After adsorption the cell was flushed with He ( $50 \text{ mL min}^{-1}$ ) for 10 min and the adsorbate spectrum was recorded.

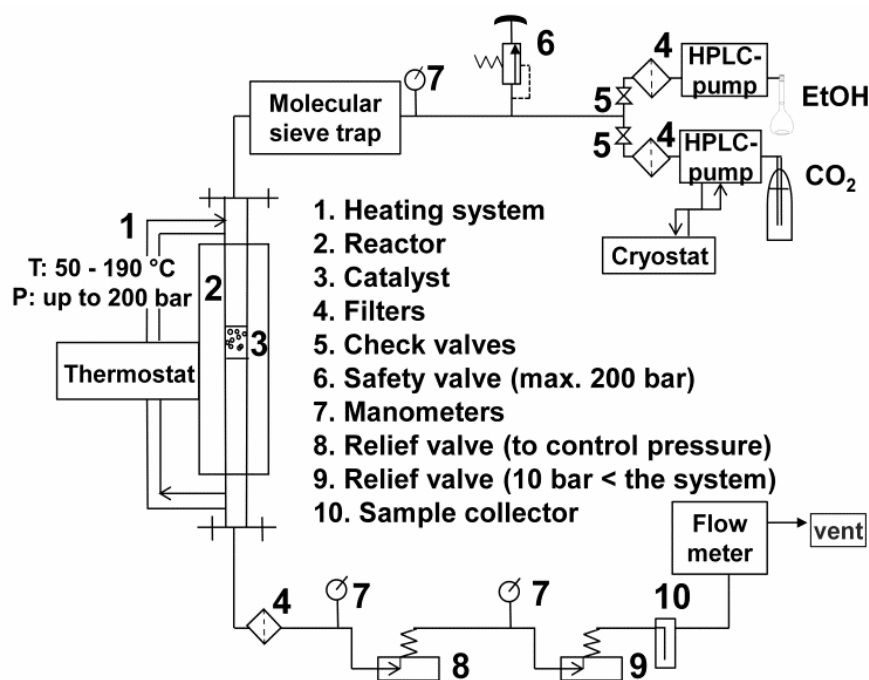
## 2.3. Experimental system and catalytic tests

### 2.3.1. Continuous flow reactor

Continuous operation is used in large-scale industrial processes. In a general procedure, the reactants are delivered continuously into the reactor at a constant flow and reaction products

and non-reacted reactants are collected at the outlet. Moreover, the rate of reaction and the concentration of reactants and reaction products change across the catalyst bed.

Diethyl carbonate from ethanol and carbon dioxide was synthesized in continuous flow reactor. The experimental setup is schematically shown in Scheme 2.1. It mainly consists of a high pressure reactor (plug flow reactor, inner volume = 32 mL, inner diameter = 12.7 mm, max. pressure = 200 bar), equipped with an oil heated jacket (max. temperature = 220 °C); high pressure pumps, relief valves, product collector and flow-meter. All tubings and fittings were made from stainless steel 316L (Swagelok).



**Scheme 2.1.** Schematic diagram of the experimental set up used for diethyl carbonate synthesis from ethanol and carbon dioxide.

In a standard procedure, the reactor was packed layer-by-layer: 27 g of corundum (size: 1 to 1.25 mm), 1 g of catalyst (size: 1 to 1.25 mm fraction), 27 g of corundum (Figure 2.1b). The catalyst was pressed and sieved in the particle size range of 1-1.25 mm. Such range was taken based on operation conditions published by C. Perego and S. Peratello [126]: the reactor diameter (D) must be minimum 10 catalyst particle diameter ( $d_p$ )  $\Rightarrow \frac{D}{d_p} > 10$ .

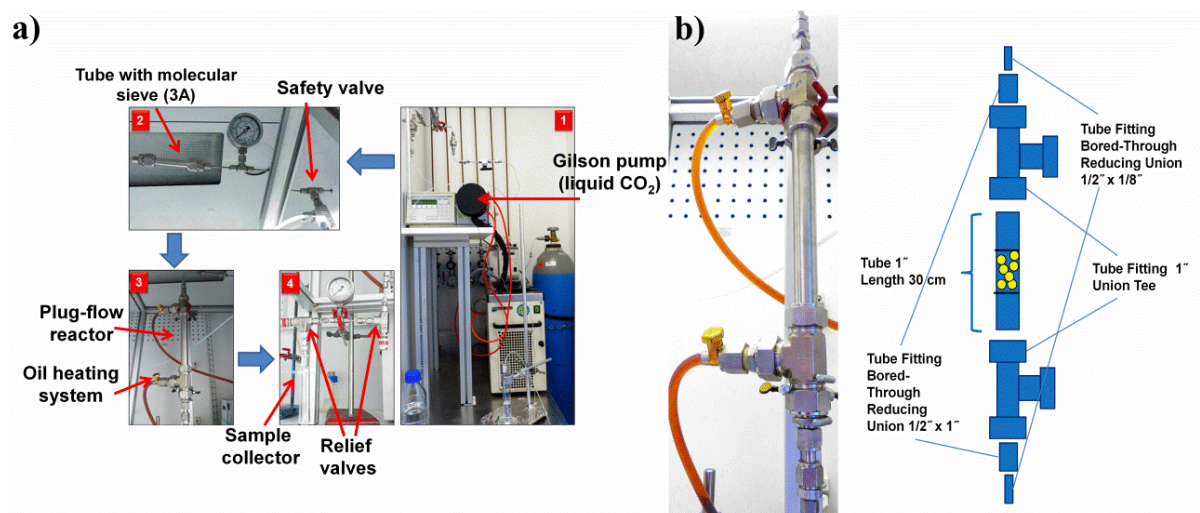


**Figure 2.1.** (a) Digital image of the experimental set up used and (b) Dimensions of plug-flow reactor (PFR).

A Gilson-pump with a thermostatic kit was employed to feed liquid CO<sub>2</sub> (99.9%, Air Liquide) to the reactor at a flow rate of 0.6 mL min<sup>-1</sup> (Figure 2.1a). A Shimadzu-HPLC pump was used in order to independently control the flow of ethanol of 0.1 mL min<sup>-1</sup> (99.9%, H<sub>2</sub>O ≤ 0.1%, Roth). The molar ratio of EtOH : CO<sub>2</sub> was kept constant during the reaction. Three different molar ratios EtOH : CO<sub>2</sub> were used: 1 : 9, 1 : 6 and 1 : 3. The mixture of ethanol and liquid CO<sub>2</sub> (from a dip tube cylinder) were passed through a tube that was filled with molecular sieve type 3A and placed before the reactor to adsorb H<sub>2</sub>O, if any is in the used ethanol. The molecular sieve dehydration technology was used to produce anhydrous EtOH. The filter with pore diameter of 0.5 μm was placed in order to avoid a discharge of catalyst with flowing reagents. The system pressure was controlled by two manually regulated relief valves in series. The first one was set to the desired reaction pressure while the second one was set to approximately 5-10 bar less. Such modification was applied to reduce a possible rapid pressure drop and to allow a more constant flow. Moreover, the second relief valve was covered by an external heating to avoid freezing of humidity. To provide the desired set pressure three different spring kits were used separately: purple (51.7 to 103 bar), orange (103 to 155) and brown (155 to 206 bar). Afterwards, the liquid phase was separated from the gas phase in a cold trap placed at the exit of the reactor outlet.

### 2.3.2. Batch reactor

Batch reactor operation is economical and simple way for small production rates. In a general procedure, the batch reactor is filled with reactants and under the reaction conditions they

convert into products. However, in comparison to continuous process the rate of batch reaction and reactant concentration depend on time. The reactant concentration falls down as shown in Figure 2.2a. Therefore, for the same reactor volume, the batch reaction would give lower conversions than continuous.

Carboxylation of methanol was performed in a stainless steel autoclave with an inner volume of 25 mL (Figure 2.2b). In a standard procedure 10 mL (247 mmol) of methanol and 50 mg of catalyst were added into the autoclave. The reactor was purged by filling and releasing 10 bar of CO<sub>2</sub> three times at room temperature. Further, liquid CO<sub>2</sub> was introduced into the reactor to reach 15 bar. Afterwards the autoclave was heated to 170 °C.

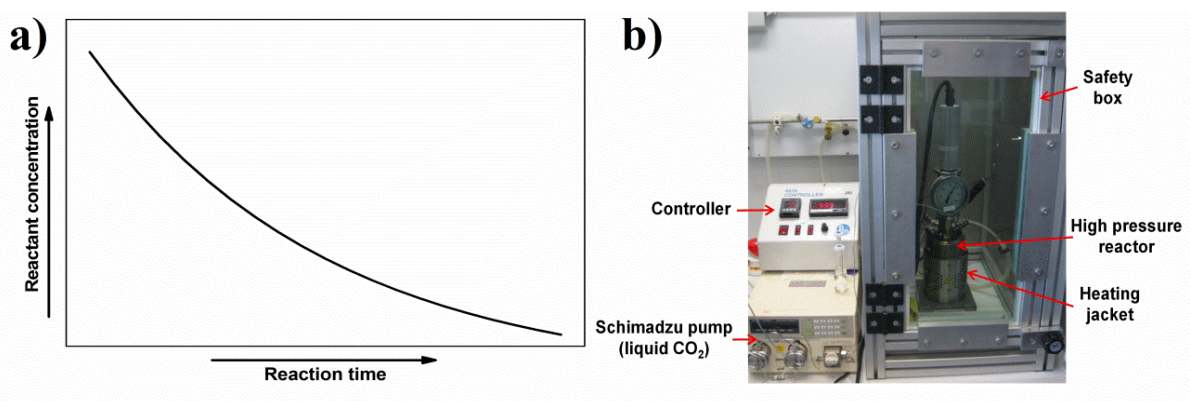


**Figure 2.2.** (a) Influence of time on the concentration of reactants in a batch reactor used for dimethyl carbonate synthesis from methanol and carbon dioxide and (b) Digital image of batch reactor with external heating jacket.

An external jacket was used for heating the reactor. When the desired temperature was achieved, the autoclave was further purged with liquid CO<sub>2</sub> to 65 bar and magnetically stirred constantly at 600 rpm during the reaction time. After 1 h of reaction the autoclave was rapidly cooled down in an ice bath to room temperature and the residual gas was immediately released.

### 2.3.3. Analysis: Gas chromatography

#### 2.3.3.1. Continuous reaction

The feed components and the reaction products were analyzed off-line by a gas chromatograph (GC-2014, Shimadzu) using a capillary column (CP-PoraBOND Q, 10m x 0.53mm x 10μm). The column outlet was connected to a methanizer (NiO catalyst) for conversion of CO<sub>2</sub> into methane, detected by a Flame Ionization Detector (FID). The temperature of the column was held at 45 °C for 3 min, then increased to 160 °C at a rate of

15 K min<sup>-1</sup> and held for 6.5 min. The yield of diethyl carbonate (Y<sub>DEC</sub>, mol%) is defined as molar amount of diethyl carbonate per initial molar amount of taken ethanol.

$$Y(DEC) = \frac{\text{mole amount of DEC formed}}{\text{mole amount of EtOH taken}/2} \times 100\% \quad (\text{Equation 2.6})$$

The standard deviation ( $\sigma$ ) is 0.001 mmol of DEC which is 0.6 %. It was calculated as

$$\sigma = \sqrt{\frac{\sum_{i=1}^n (x_i - \bar{x})^2}{n-1}} \quad (\text{Equation 2.7})$$

$n$  = number of GC measurements made

$x_i$  = each measurement result (mmol of DEC)

$\bar{x}$  = mean value of measurement results (mmol of DEC)

### 2.3.3.2. Batch reaction

Liquid products were analyzed off-line by gas chromatography using a GC HP6890 equipped with an HP-1 capillary column (length 50 m). The yield of DMC (Y<sub>DMC</sub>, mol%) was calculated on the basis of methanol fed.

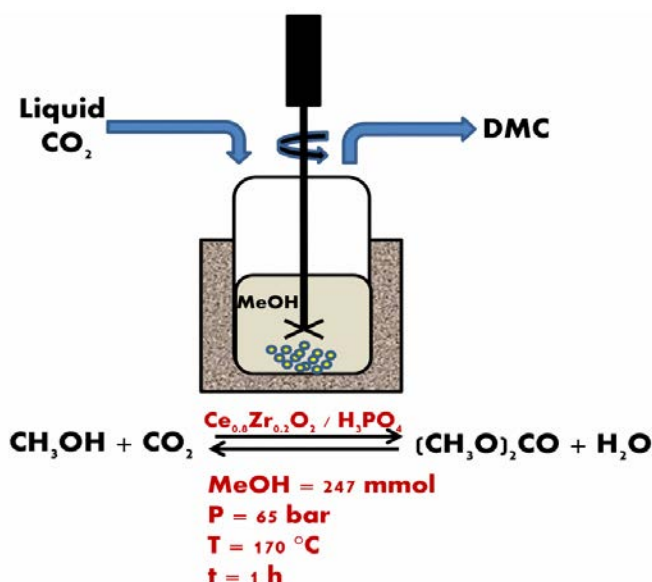
$$Y(DMC) = \frac{\text{mole amount of DMC formed}}{\text{mole amount of MeOH taken}/2} \times 100\% \quad (\text{Equation 2.8})$$



## Chapter 3

### 3. Ce-Zr mixed oxide catalysts and surface modified $\text{Ce}_{0.8}\text{Zr}_{0.2}\text{O}_2$ for the direct synthesis of dimethyl carbonate from methanol and $\text{CO}_2$

Chapter 3 presents the results about the influence of (i) Ce content in  $\text{Ce}_x\text{Zr}_{1-x}\text{O}_2$  solids and (ii) surface modification of  $\text{Ce}_{0.8}\text{Zr}_{0.2}\text{O}_2$  on catalyst performance in the direct dimethyl carbonate synthesis from methanol and  $\text{CO}_2$ . Different Ce-Zr precursors were prepared by a co-precipitation method and calcined at 600 °C. Phosphate surface groups on  $\text{Ce}_{0.8}\text{Zr}_{0.2}\text{O}_2$  solids were generated by treating Ce-Zr-hydroxide precursors and Ce-Zr mixed oxides ( $T_c = 600$  °C) with phosphoric acid. Catalysts were thoroughly characterized by  $\text{N}_2$ -adsorption (BET-SA), XRD, TEM, in situ FTIR,  $\text{NH}_3$ -TPD as well as  $\text{CO}_2$ -TPD. The materials obtained were tested towards the formation of dimethyl carbonate from methanol and carbon dioxide at 170 °C and 65 bar for 1 h using a batch reactor.



### 3.1. Ce-Zr mixed oxide catalysts for the direct synthesis of dimethyl carbonate from methanol and carbon dioxide

#### 3.1.1. Catalysts characterization

##### *BET surface area*

The specific surface areas (SSA), pore volumes and pore diameters of pure metal oxides ( $C^{prec}$  and  $Z^{prec}$ ) and mixed metal oxides ( $C20Z^{prec}$ ,  $C40Z^{prec}$ ,  $C60Z^{prec}$  and  $C80Z^{prec}$ ) are summarized in Table 3.1.

**Table 3.1.** Effect of Ce loading on selected textural properties of  $Ce_xZr_{1-x}O_2$  solids.

Sample	$x$ in $Ce_xZr_{1-x}O_2$	BET-SA ( $m^2 g^{-1}$ )	Pore V ( $cm^3 g^{-1}$ )	Average pore d (nm)
$Z^{prec}$	0.0	25	0.13	3.7
$C20Z^{prec}$	0.2	71	0.19	4.0
$C40Z^{prec}$	0.4	92	0.24	3.7
$C60Z^{prec}$	0.6	73	0.11	3.7
$C80Z^{prec}$	0.8	46	0.13	4.0
$C^{prec}$	1.0	45	0.18	3.7

The surface areas and pore volumes of the unmodified samples vary between 25 and 92  $m^2 g^{-1}$  and between 0.11 and 0.24  $cm^3 g^{-1}$ , respectively. The highest values were obtained for a  $Ce_xZr_{1-x}O_2$  sample with 40% cerium. On the basis of average pore diameters varying between 3.7 to 4.0 nm, it can be concluded that all samples are mesoporous. For the  $C80Z^{prec}$  catalyst, the crystallite sizes were in a good agreement with the values obtained by transmission electron microscopy (see Figure 3.5). Furthermore, the size of individual nanoparticle (visible by TEM) and the crystallite size (calculated by XRD) confirmed that the nanoparticles were not twinned.

##### *X-ray powder diffraction analysis (XRD)*

In the present study the structural assignment was performed using V-curves where the volumes of the substituted unit cells for cubic ( $Ce_xZr_{1-x}O_2$  ( $Fm3m$  space group) and tetragonal ( $Zr_xCe_{1-x}O_2$  ( $P4_2/nmc$  space group) phases were taken from the ICSD database (FIZ Karlsruhe, see Figure 3.2). Therefore, the lattice volume is related to the respective molar compositions in the  $Ce_xZr_{1-x}O_2$  mixed oxides. The obtained phase compositions from V-curves were in a good agreement with those determined using the Rietveld method (program package TOPAS 4.2 from Bruker). Figure 3.1 shows the diffractograms of

$Ce_xZr_{1-x}O_2$  with different Ce/Zr ratios. The results show that ceria is stabilized in the fluorite structure, whereas both monoclinic (71 wt%) and tetragonal phases (29 wt%) were identified in bare  $ZrO_2$ .

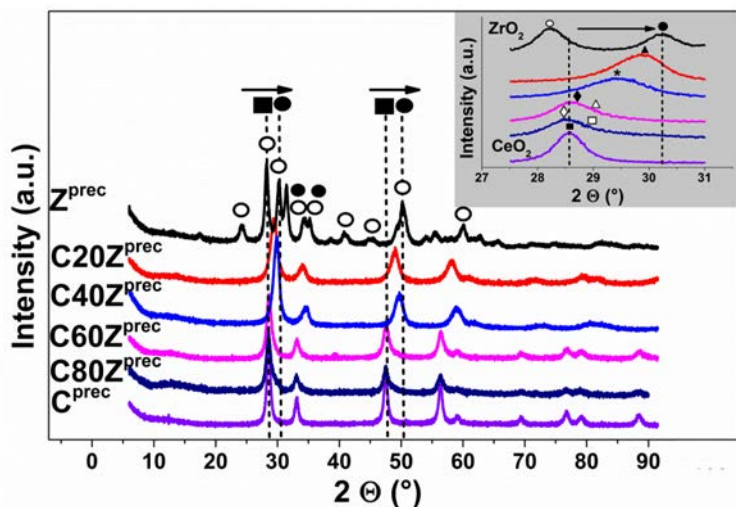


**Figure 3.1.** Diffractograms for  $Ce_xZr_{1-x}O_2$  catalysts. Phase composition: ■ cubic  $CeO_2$  (JCPDS 01-078-0694), ● tetragonal  $ZrO_2$  (JCPDS 01-079-1764), ○ monoclinic  $ZrO_2$  (JCPDS 01-078-0047). Inset: ▲  $t-Ce_{0.26}Zr_{0.74}O_2$ , \*  $t-Ce_{0.45}Zr_{0.55}O_2$ , ◆  $t-Ce_{0.91}Zr_{0.09}O_2$ , △  $t-Ce_{0.5}Zr_{0.5}O_2$ , ◇  $c-Ce_{0.93}Zr_{0.07}O_2$ , □  $t-Ce_{0.62}Zr_{0.38}O_2$ .

In case of mixed metal oxides, the substitution of  $Ce^{4+}$  (ionic radius 0.097 nm) with relatively smaller  $Zr^{4+}$  (ionic radius 0.084 nm) led to a shrinkage of resulted lattice (smaller inter-plane distance  $d$  and lattice constant) and as a consequence to a shift of peak reflections to higher diffraction angles, according to the Bragg's law ( $2d\sin\theta = n\lambda$ , where  $d$  is the spacing between the planes in the lattice,  $\theta$  is the diffraction angle,  $n$  is an integer and  $\lambda$  is the wavelength of incident X-ray wavelength) [127, 128]. The lattice constants ( $a$  and  $c$ ) were slightly changed after addition of zirconium into ceria. A distinct decrease in lattice parameters  $a$  and  $c$  occurred upon incorporation of increasing amount of  $Zr^{4+}$  ( $\geq 60$  mol%) into  $CeO_2$ . The crystallite sizes of the  $Ce_xZr_{1-x}O_2$  samples are varied between 7 and 15 nm calculated from diffractograms by using the Scherrer equation  $D_{XRD} = K\lambda / \beta\cos\theta$  [125] (Table 3.2). It was found that the  $C20Z^{prec}$  and  $C40Z^{prec}$  mixed oxides exhibited homogeneous solid solutions with 100 wt% of tetragonal  $Ce_{0.26}Zr_{0.74}O_2$  and  $Ce_{0.45}Zr_{0.55}O_2$  structure, respectively (see Table 3.2). However, for samples with Ce content  $\geq 60$  mol% ( $C60Z^{prec}$  and  $C80Z^{prec}$ ) additional XRD reflexes were observed.

**Table 3.2.** Effect of Ce content and surface modification on crystallite size (D) and lattice constants of  $\text{Ce}_x\text{Zr}_{1-x}\text{O}_2$  solid solutions. The crystallographic density ( $\rho$ ) and microstrain ( $\varepsilon$ ) for each phase were also calculated.

Sample code	Rietveld method		V-curve							
	Crystal phase	$\rho$ ( $\text{g cm}^{-3}$ )	Crystal phase	$\rho$ ( $\text{g cm}^{-3}$ )	a (nm)	b (nm)	c (nm)	D (nm)	V ( $\text{nm}^3$ )	$\varepsilon$ (%)
$Z^{\text{prec}}$	-	-	71% m- $\text{ZrO}_2$	5.78	0.51	0.52	0.53	14	0.141	0.20
			29% t- $\text{ZrO}_2$	6.06	0.36		0.52	12	0.067	0.11
$\text{C20Z}^{\text{prec}}$	100% t- $\text{Ce}_{0.36}\text{Zr}_{0.64}\text{O}_2$	6.65	100% t- $\text{Ce}_{0.26}\text{Zr}_{0.74}\text{O}_2$	6.42	0.37		0.52	11	0.070	0.53
$\text{C40Z}^{\text{prec}}$	100% t- $\text{Ce}_{0.57}\text{Zr}_{0.43}\text{O}_2$	6.90	100% t- $\text{Ce}_{0.45}\text{Zr}_{0.55}\text{O}_2$	6.63	0.37		0.53	7	0.073	0.43
$\text{C60Z}^{\text{prec}}$	68% c- $\text{Ce}_{0.98}\text{Zr}_{0.02}\text{O}_2$	7.20	68% c- $\text{Ce}_{0.91}\text{Zr}_{0.09}\text{O}_2$	7.06	0.54			12	0.158	0.21
	32% t- $\text{Ce}_{0.73}\text{Zr}_{0.27}\text{O}_2$	7.20	32% t- $\text{Ce}_{0.5}\text{Zr}_{0.5}\text{O}_2$	6.68	0.37		0.53	8	0.073	1.24
$\text{C80Z}^{\text{prec}}$	76% c- $\text{Ce}_{0.95}\text{Zr}_{0.05}\text{O}_2$	7.13	76% c- $\text{Ce}_{0.93}\text{Zr}_{0.07}\text{O}_2$	7.09	0.54			11	0.158	0.24
	24% t- $\text{Ce}_{0.79}\text{Zr}_{0.21}\text{O}_2$	7.20	24% t- $\text{Ce}_{0.62}\text{Zr}_{0.38}\text{O}_2$	6.82	0.37		0.54	7	0.075	0.76
$\text{C80ZP-2}$	-	-	87% c- $\text{Ce}_{0.93}\text{Zr}_{0.07}\text{O}_2$	7.09	0.54			11	0.158	0.25
			13% t- $\text{Ce}_{0.22}\text{Zr}_{0.78}\text{O}_2$	6.37	0.37		0.53	5	0.070	0.36
$\text{C}^{\text{prec}}$	-	-	100% c $\text{CeO}_2$	7.20	0.54			15	0.160	0.16

It was proven that these two samples were not homogeneous in nature and were composed of two different phases, i.e. a tetragonal phase with lower content of Ce with respect to nominal composition (t- $Ce_{0.5}Zr_{0.5}O_2$  for C60Z<sup>prec</sup> and t- $Ce_{0.62}Zr_{0.38}O_2$  for C80Z<sup>prec</sup>) and ii) a cubic phase with higher Ce concentration in regard to nominal composition (c- $Ce_{0.91}Zr_{0.09}O_2$  for C60Z<sup>prec</sup> and t- $Ce_{0.93}Zr_{0.07}O_2$  for C80Z<sup>prec</sup>). Alifanti *et al.* [121] and Yao-Matsuo *et. al* [129] also found that at low cerium contents homogeneous solid solutions can be obtained during sol-gel synthesis while an increase in Ce content led to an appearance of two separate phases: a cubic  $CeO_2$  and cubic  $Ce_{0.5}Zr_{0.5}O_2$ .

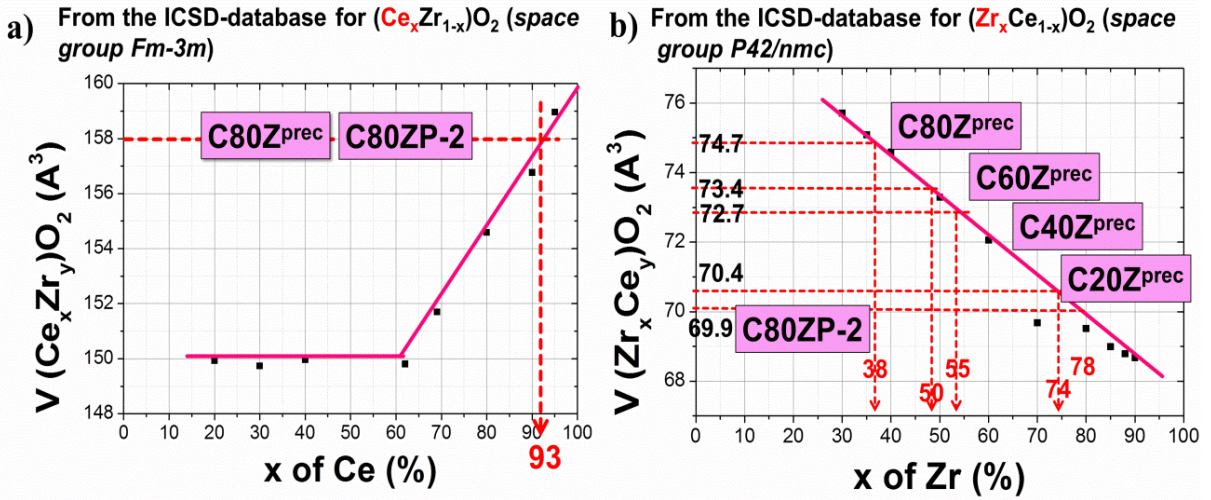


**Figure 3.2.** (a) Volume of the unit cells of the cubic  $(Ce_xZr_{1-x})O_2$  phase as a function of Ce content and (b) Tetragonal  $(Zr_xCe_{1-x})O_2$  phase as a function of the Zr content.

The phase composition of  $Ce_xZr_{1-x}O_2$  solids determined by applying V-curves is summarized in Table 3.2. In case of C60Z<sup>prec</sup>, it was composed of 68 wt% of cubic  $Ce_{0.91}Zr_{0.09}O_2$  and 32 wt% of tetragonal  $Ce_{0.5}Zr_{0.5}O_2$  phases. The C80Z<sup>prec</sup> sample showed well-defined diffraction peaks corresponding to 76 wt% of cubic  $Ce_{0.93}Zr_{0.07}O_2$  and a few less intense peaks due to 24 wt% of tetragonal  $Ce_{0.62}Zr_{0.38}O_2$  phase. Additionally, the lattice volume for the substituted tetragonal and cubic phase was determined. According to Vegard's law, the replacement of  $Ce^{4+}$  cation (0.097 nm) with smaller  $Zr^{4+}$  cation (0.084 nm) leads to a shrinkage of  $CeO_2$  lattice. Hence, with increasing content of incorporated Zr atoms into  $CeO_2$  lattice the corresponding volume and the crystallographic densities (so called density of the unit cell) decreased. Calculated microstrain (Equation 2.4) in the crystal lattice of the  $Ce_xZr_{1-x}O_2$  solid solutions is also presented in Table 3.2. The microstrain is the lattice distortion inside a grain due to the incorporation of  $Zr^{4+}$  into  $CeO_2$ . The microstrain in polycrystalline material appears when small grains deformed in different ways so that the defects (dislocations) could not move in the whole sample volume. This situation leads to

peak broadening. The microstrain of mixed Ce-Zr oxides decreased with zirconium addition into  $CeO_2$ . Such doping effect of  $Zr^{4+}$  into  $CeO_2$  is well described by R. Si *et al.* [130]. Those authors reported that the high lattice strain level in  $Ce_xZr_{1-x}O_2$  solid solutions was related to the large density of oxygen defects including pure oxygen vacancy and vacancy-interstitial oxygen defects in the crystal lattice. Therefore, the zirconium content affects the concentration of oxygen defects and thus resulted in lattice strain in the  $Ce_xZr_{1-x}O_2$  solid solutions.

### ***Elemental analysis by Inductively coupled plasma optical emission spectroscopy (ICP-OES) and X-ray photoelectron spectroscopy (XPS)***

Bulk and surface atomic ratios of Ce/Zr determined from ICP and XPS measurements of  $Ce_xZr_{1-x}O_2$  samples are shown in Table 3.3.

**Table 3.3.** Comparison of molar Ce/Zr ratios in the near-surface-region (as measured by XPS) with bulk composition (as measured by ICP) for  $Ce_xZr_{1-x}O_2$  solids.

Sample	Ce/Zr nominal	Bulk composition (ICP)	Surface composition (XPS)	EDX
		Ce/Zr	Ce/Zr	Ce/Zr
C20Z <sup>prec</sup>	0.25	0.27	0.07	
C40Z <sup>prec</sup>	0.66	0.79	0.25	
C60Z <sup>prec</sup>	1.5	1.9	1.44	
C80Z <sup>prec</sup>	4	5.5	4.25	2.4, 24.1, 12.6 <sup>a</sup>

<sup>a</sup> Figure 3.5a', Ce/Zr molar ratios on labelled areas

The measured ratios were compared with the nominal ones assuming that the metals have been uniformly distributed within the Ce-Zr-O system. The counterparts of C60Z<sup>prec</sup> and C80Z<sup>prec</sup> possessed the nearly nominal Ce/Zr surface atomic ratios of 1.44 and 4.25, respectively. However, at lower Ce contents (samples C40Z<sup>prec</sup> and C20Z<sup>prec</sup>) the surface Ce/Zr ratio is significantly reduced. Such migration of Zr from the bulk to the surface was also noticed by other research groups, who indicated a decrease in the Ce/Zr ratio for  $Ce_{0.7}Zr_{0.3}O_2$ ,  $Ce_{0.5}Zr_{0.5}O_2$  and  $Ce_{0.3}Zr_{0.7}O_2$  [131].

### ***Acid-base properties: Temperature-programmed desorption (TPD) of $NH_3$ and $CO_2$***

Temperature-programmed desorption of  $NH_3$  was used to evaluate acidic properties (total number of acidic sites and their distribution) of the Ce-Zr mixed oxides. The amount of desorbed ammonia, expressed as  $\mu\text{mol}$  of  $NH_3$  per square meter and per gram of catalyst, was taken as a measure of the total acidity of the catalysts (Table 3.4).

**Table 3.4.** Acidic and base characteristics of the  $Ce_xZr_{1-x}O_2$  samples.  $T_{\text{max}}$  ( $NH_3$ ) and  $T_{\text{max}}$  ( $CO_2$ ) stand for temperature of maximal  $NH_3$  and  $CO_2$  desorption, respectively.

Sample	Total basicity ( $CO_2$ -TPD)		Total acidity ( $NH_3$ -TPD)	
	$CO_2$ desorbed ( $\mu\text{mol g}^{-1}$ )	$CO_2$ desorbed ( $\mu\text{mol m}^{-2}$ )	$NH_3$ desorbed ( $\mu\text{mol g}^{-1}$ )	$NH_3$ desorbed ( $\mu\text{mol m}^{-2}$ )
$Z^{prec}$	80	3.2	110	4.4
$C20Z^{prec}$	90	1.3	90	1.3
$C40Z^{prec}$	120	1.3	90	1.0
$C60Z^{prec}$	100	1.4	60	0.8
$C80Z^{prec}$	100	2.2	90	2.0
$C^{prec}$	90	2.0	3	0.07

$NH_3$ -TPD profiles of the  $C_xZr_{1-x}O_2$  samples are presented in Figure 3.3a. The intensity of desorption peaks considerably increased after incorporation of zirconium atoms into the ceria lattice leading to an increase in total concentration of acid sites as reported elsewhere [132]. The highest number of acidic sites was observed for pure  $ZrO_2$  ( $Z^{prec}$ ,  $4.4 \mu\text{mol m}^{-2}$ ), whereas the lowest one was found for pure  $CeO_2$  ( $C^{prec}$ ,  $0.07 \mu\text{mol m}^{-2}$ ). Pengpanich *et al.* [134] reported that  $Zr^{4+}$  exhibits more acidic nature than  $Ce^{4+}$  and incorporation of  $Zr^{4+}$  into  $CeO_2$  lattice can promote the formation of acidic sites in resulted Ce-Zr-O solid solution. As in a present work,  $Zr^{4+}$  in  $CeO_2$  increased the total amount of  $NH_3$  desorbed from Ce-Zr-O solid solutions compared to pure  $CeO_2$ .

On the bases of broad  $NH_3$ -TPD profiles in Figure 3.3a, one can conclude that the tested samples possess acidic sites of different strength. The desorption peaks of  $NH_3$  located at 100-200 °C, 200-400 °C and 400-450 °C can be assigned to weak, moderate and strong acid sites, respectively [133]. The Ce-Zr-O catalysts exhibit mainly weak (<200 °C) and moderate (200-400 °C) acid sites. However, the concentration and distribution of acid sites depend upon the Ce/Zr ratio.



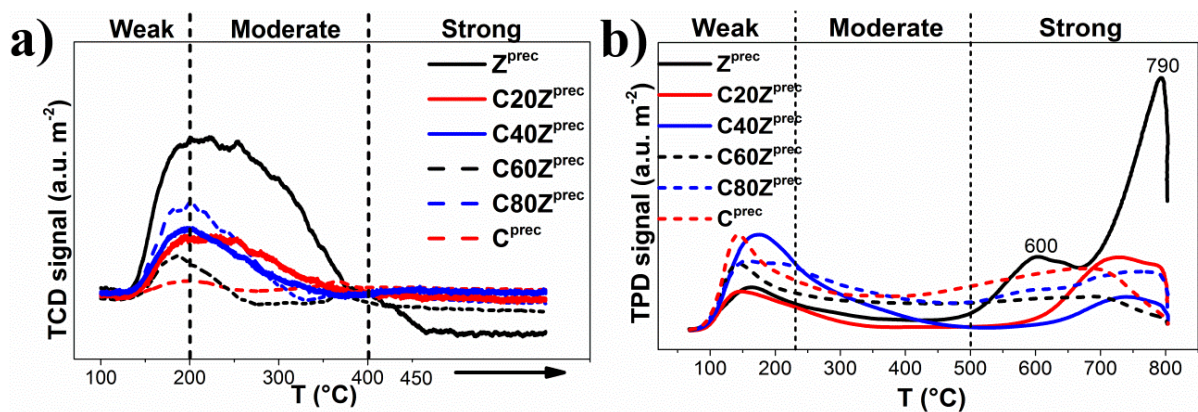


**Figure 3.3.** (a)  $NH_3$ -TPD profiles of  $Ce_xZr_{1-x}O_2$  catalysts, (b)  $CO_2$ -TPD profiles of  $Ce_xZr_{1-x}O_2$  solids.

In order to analyze basic properties of the Ce-Zr-O solids,  $CO_2$ -TPD experiments were also carried out.  $CO_2$  was used as an acidic probe molecule being able to adsorb on surface hydroxyls (forms hydrogen carbonate species) or oxygen ions (forms carbonate species) of metal oxides [134]. Figure 3.3b illustrates the  $CO_2$ -TPD profiles obtained for different  $Ce_xZr_{1-x}O_2$  solids. All Ce-Zr-O catalysts exhibit two broad desorption peaks of  $CO_2$  thus indicating the presence of different types of basic sites such as weak (100-230 °C), moderate (230-500 °C) and strong (above 500 °C) basic sites [105, 135]. The total concentration of basic sites of Ce-Zr-O solid solutions, expressed as the amount of  $CO_2$  desorbed per gram and per square meter of catalyst, is reported in Table 3.4. It can be found that pure  $ZrO_2$  ( $3.2 \mu mol m^{-2}$ ) has the highest concentration of basic sites, which markedly decreases upon addition of 20 mol% of cerium, then increases as Ce content is further increases up to 80 mol%. It was reported that chemical mixing can significantly change basic properties of given metal oxides [136]. As in this case, the incorporation of zirconium into ceria lattice had a direct influence on the basicity and acidity of parent oxides. Moreover, the contribution of strong basic sites to total basicity was more significant as Zr content in the Ce-Zr mixed oxides increased.

### 3.1.2. Catalytic results

Table 3.5 depicts the effect of Ce content in  $Ce_xZr_{1-x}O_2$  catalysts on DMC yield. No DMC was formed over pure  $ZrO_2$ . Catalytic properties of  $ZrO_2$  are greatly enhanced upon its promoting with  $CeO_2$ . It is evident from the results shown in Table 3.5 that the yield of DMC increases with increasing Ce content up to 60% and then remained constant ( $Y_{DMC} \sim 0.24\%$ ). According to the literature, the equilibrium DMC yield was about 2% [137, 138].



**Table 3.5.** Influence of cerium content in  $Ce_xZr_{1-x}O_2$  catalysts on the yield of DMC (Reaction conditions: catalyst weight 50 mg,  $CH_3OH = 247$  mmol,  $T = 170$  °C,  $p = 65$  bar,  $t = 1$  h, 600 rpm).

Sample	x in $Ce_xZr_{1-x}O_2$	Y–DMC (mol%)
$Z^{prec}$	0	0.00
$C20Z^{prec}$	0.2	0.04
$C40Z^{prec}$	0.4	0.13
$C60Z^{prec}$	0.6	0.24
$C80Z^{prec}$	0.8	0.24
$C^{prec}$	1	0.24

No correlation between the DMC yield and BET-SA was found. In fact, the tetragonal  $Ce_xZr_{1-x}O_2$  phase was mainly formed in  $Z^{prec}$ ,  $C20Z^{prec}$  and  $C40Z^{prec}$ , whereas the cubic  $Ce_xZr_{1-x}O_2$  phase was predominant in  $C60Z^{prec}$ ,  $C80Z^{prec}$  and also in pure ceria ( $C^{prec}$ ). Since the latter samples are significantly more active ( $Y_{DMC} \sim 0.24\%$ ), it can be concluded that the most active phase for DMC formation is cubic  $Ce_xZr_{1-x}O_2$  ( $C60Z^{prec}$ ,  $C80Z^{prec}$ ,  $C^{prec}$ ).

Previous studies deal with DMC synthesis from methanol and  $CO_2$  [87, 124] reported that the acid-base properties play a crucial role in the target reaction. As described by Tomishige *et al.* [139], the presence of both acidic and basic sites is the key factor for activating methanol and  $CO_2$  in the course of DMC synthesis. More precisely, a suitable combination of acidic and basic sites is responsible for controlling catalytic carboxylation of methanol over  $ZrO_2$  catalysts. Tomishige *et al.* [87] further claimed that an equal number of neighboring acid-base sites is required for optimal catalyst performance. For the most active catalysts (e.g.  $C60Z^{prec}$ ,  $C80Z^{prec}$  and  $C^{prec}$ ) towards DMC formation this is obviously not the case. Basic sites dominate on their surface (see Table 3.4).

Based on initial results (maximal DMC yields  $\sim 0.24\%$ ), the  $CeO_2$ - $ZrO_2$  solid solution catalyst with a theoretical Ce/Zr ratio of 4 ( $C80Z^{prec}$ ) was chosen and used in subsequent runs especially for modification with  $H_3PO_4$  to boost the yield of DMC beyond 0.24%. The promoting effect of  $H_3PO_4$  was then investigated by varying the P-contents in  $C80Z^{prec}$  with the aim to identify efficient catalyst compositions for achieving enhanced DMC yields.

### 3.2. Surface modified $Ce_{0.8}Zr_{0.2}O_2$ catalyst for direct synthesis of dimethyl carbonate from methanol and $CO_2$ .

#### 3.2.1. Catalysts characterization

##### *BET surface area*

The specific surface area (SSA), pore volume and diameter of modified mixed metal oxides (C80ZP-1, C80ZP-2, C80ZP-3 and C80ZP\*) are summarized in Table 3.6.

**Table 3.6.** Effect of surface modification on the textural properties of  $Ce_{0.8}Zr_{0.2}O_2$  solids.

Sample	$x$ in $Ce_xZr_{1-x}O_2$	P/Zr	$P_{surf.}^b$ (mol%)	BET-SA ( $m^2 g^{-1}$ )	Pore V ( $cm^3 g^{-1}$ )	Average pore d (nm)
C80ZP-1	0.8	0.03	0	73	0.11	3.7
C80ZP-2	0.8	0.12	5	63	0.09	4.3
C80ZP-3	0.8	0.30	34	74	0.10	3.7
C80ZP* <sup>a</sup>	0.8	0.12	21	22	0.08	4.0

<sup>a</sup> post-treated sample ( $H_3PO_4$ -addition to already calcined solid)

<sup>b</sup> surface concentration of phosphorus measured by XPS, assuming that  $Ce+Zr+P=100\%$

The treatment of Ce-Zr hydroxides with  $H_3PO_4$  provoked textural modifications. As a result, considerable changes in surface area and pore volume were observed. C80ZP-2 and C80ZP-1 with P concentration on the surface of 5 mol% and 0 mol%, respectively, showed differences in their specific surface areas. These results are in good agreement with those earlier reported by López Granados *et al.* [140] and Smitha *et al.* [141] where the effect of P loading on structural properties of  $CeO_2/H_3PO_4$  and  $ZrO_2/H_3PO_4$ , in particular on specific surface area, was investigated. It was found that with low amount of phosphorus (2.5 mL of  $H_3PO_4$  per gram of the hydroxide), surface area of  $CeO_2/H_3PO_4$  and  $ZrO_2/H_3PO_4$  slightly increased with respect to parent  $CeO_2$  and  $ZrO_2$ , respectively. However, a further addition of P (5 mL of  $H_3PO_4$ ) led to a decrease in surface area. Nonetheless, this tendency seems to be not valid for the C80ZP-3 (P = 34 mol%) solid, which demonstrated the highest specific surface area of  $74 m^2 g^{-1}$  among all phosphated  $Ce_{0.8}Zr_{0.2}O_2$  samples. In case of the C80ZP\* sample, where the phosphorus was incorporated into the calcined C80ZP<sup>prec</sup> catalyst, a significant loss of SA was found. However, the surface of post-treated C80ZP\* sample contained less phosphorus (26 mol%) in comparison with the C80ZP-3 catalyst. The main reason for such decline of surface area might be the double calcination of C80ZP\* solid at 600 °C, for four hours each time. It is well-known fact that long time calcination causes a

decrease in specific surface area of Ce-based oxides [142]. Therefore, it can be concluded that any change in surface behavior of C80ZP\* occurred as a result of thermal treatment (indicated by the drop in SA).

### ***X-ray powder diffraction analysis (XRD)***

The XRD pattern of C80Z<sup>prec</sup> solid is presented in Figure 3.4. C80ZP-2 was selected for XRD analysis due to its improved catalytic activity towards DMC formation (see Table 3.10).

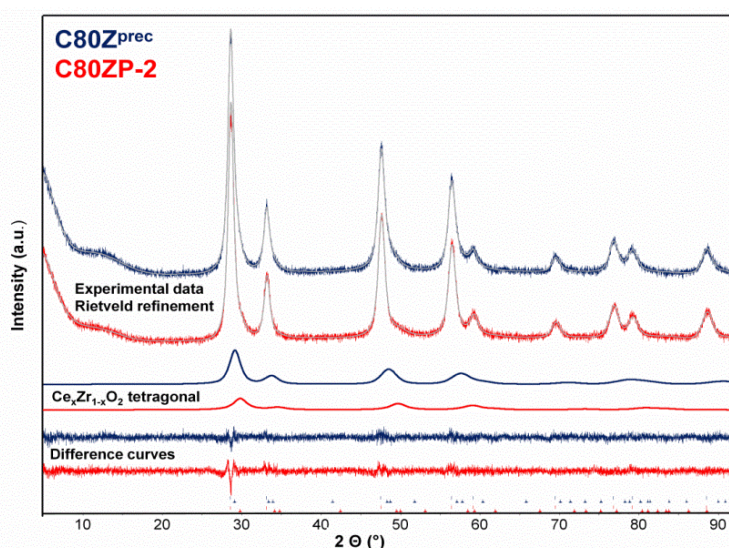


**Figure 3.4.** Representative X-ray powder diffractograms with Rietveld refinement of the samples C80Z<sup>prec</sup> and C80ZP-2 with additionally highlighted tetragonal  $Ce_xZr_{1-x}O_2$  phases.

Unphosphated C80Z<sup>prec</sup> sample is composed of a tetragonal Ce-rich  $Ce_{0.62}Zr_{0.38}O_2$  phase (24%) besides a cubic  $Ce_{0.93}Zr_{0.07}O_2$  phase (76%). In contrast, the formation of a Zr-rich tetragonal  $Ce_{0.22}Zr_{0.78}O_2$  phase (13%) and the cubic  $Ce_{0.93}Zr_{0.07}O_2$  phase (87%) is observed in the phosphated C80ZP-2 sample (see Table 3.2). Crystalline P-containing phases were not detected in these phosphated samples.

### ***Elemental analysis by Inductively coupled plasma optical emission spectroscopy (ICP-OES) and X-ray photoelectron spectroscopy (XPS)***

Bulk and surface atomic ratios (Ce/Zr and P/Zr) from ICP and XPS measurements of the three P-modified C80Z<sup>prec</sup> samples obtained after  $H_3PO_4$  pretreatment of a Ce-Zr hydroxide precursor (C80ZP1-3, P/Zr = 0.03-0.3) are reported in Table 3.7. In addition, the data of another P-doped catalyst are also included (C80ZP\*) for comparative purposes.

**Table 3.7.** Comparison of the overall molar Ce/Zr and P/Zr ratios in the near-surface-region (as measured by XPS) with bulk composition (as measured by ICP) for modified  $Ce_{0.8}Zr_{0.2}O_2$  solids.

Sample			Bulk composition (ICP)		Surface composition (XPS)		EDX
	Ce/Zr nominal	P/Zr nominal	Ce/Zr	P/Zr	Ce/Zr	P/Zr	Ce/Zr
C80ZP-1	4	0.03	4.6	0.04	3.76	n.d. <sup>a</sup>	
C80ZP-2	4	0.12	4.7	0.13	6.69	0.4	6.4, 20.6 <sup>b</sup>
C80ZP-3	4	0.3	4.6	0.47	2.13	1.6	
C80ZP*	4	0.12	1.5	0.13	0.6	0.3	

<sup>a</sup> n.d. – not determined

<sup>b</sup> Fig.3.5b, Ce/Zr molar ratios on labelled areas

Bulk and surface concentrations of P-modified  $C80Z^{prec}$  (C80ZP1-3 and C80ZP\*) catalyst components measured via ICP and XPS measurements, respectively, are reported in Table 3.7. The ICP results revealed a nearly constant Ce/Zr bulk ratio independent on the amount of  $H_3PO_4$  added to the Ce-Zr hydroxide precursor. From the near-surface region compositions (XPS), a maximum of Ce-enrichment was found on the surface of C80ZP-2. These findings are in a good agreement with those reported by Atribak *et al.* [143]. Since the solubility constant of  $Zr(OH)_4$  is lower than that of  $Ce(OH)_3$  ( $2 \times 10^{-48}$  and  $1.5 \times 10^{-20}$ , respectively), a faster precipitation of  $Zr(OH)_4$  during the co-precipitation of  $Ce^{3+}$  and  $Zr^{4+}$  occurs. Therefore, the nuclei of particles will be rich in Zr and outer part will have a Ce-enrichment while the overall compositions obtained by ICP confirmed Ce/Zr ratios very close to the theoretical values. XPS did not detect the phosphorus on the surface of C80ZP-1 (nominal ratio P/Zr = 0.03). Most probably the concentration of P is below the detection limit of XPS technique. On the other hand, C80ZP-3 exhibited Zr-rich surface at phosphorus concentration of 34 mol%. López Granados *et al.* [140] also observed such a decrease in Ce concentration with increasing amount of incorporated P in  $CeO_2/H_3PO_4$  sample. The surface P/Zr ratio of C80ZP-2 was found to be 0.4 and this value is three times higher than its corresponding bulk value (0.13). Comparing ICP and XPS data, it is suggested that P is an important component for tuning catalytic performance and it is mainly concentrated in the near-surface-region of Ce-Zr mixed oxides. In contrary, the post-treated (P-addition to a calcined solid) C80ZP\* sample exhibits low concentration of Ce and high concentration of Zr in the near-surface-region compared to the others. Obviously, the  $H_3PO_4$  treatment of an already calcined catalyst causes Ce-leaching and, therefore, an overall enrichment in Zr. Moreover, the near-surface

concentration of P is much higher (more than three times) than the best C80ZP-2 catalyst. It can be assumed that P remained on the surface (probably formation of monolayer) and did not go deeper into the bulk during impregnation of already calcined samples.

### ***Transmission electron microscopy (TEM)***

HAADF-STEM images of C80Z<sup>prec</sup> and C80ZP-2 are shown in Figure 3.5. They revealed nanosized irregular particles densely agglomerated in two cases. The particles sizes of C80Z<sup>prec</sup> and C80ZP-2 are in the range of 7-15 nm in good agreement to the calculated crystallite sizes from XRD (see Table 3.2).

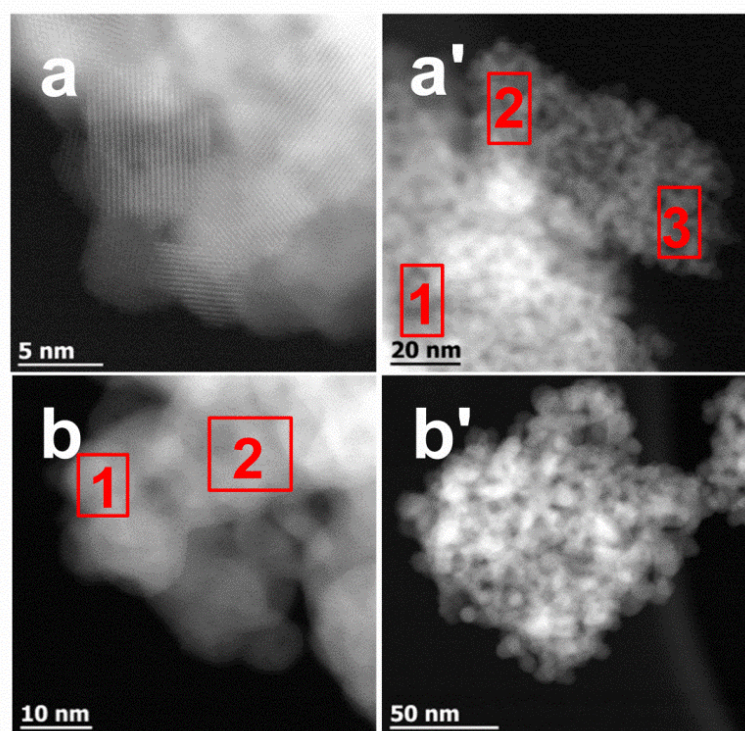


**Figure 3.5.** HAADF-STEM images of (a), (a') C80Z<sup>prec</sup> and (b), (b') C80ZP-2. EDX analysis of the Ce/Zr molar ratio: (a') 1 = 2.4, 2 = 24.1, 3 = 12.6; (b) 1 = 6.4, 2 = 20.6.

Energy dispersive X-Ray analysis (EDX) was used to get information about local composition. EDX results from a relatively large region (0.1-0.3  $\mu\text{m}$ ) confirmed that the distribution of cerium and zirconium concentrations within the selected region is also different (labelled areas in Figure 3.5). In C80Z<sup>prec</sup> the Ce-enrichment is represented by the formation of Ce-rich  $Ce_{0.93}Zr_{0.07}O_2$  phase. In case of C80ZP-2, EDX results confirmed the presence of Ce-rich as well as Zr-rich regions. In C80ZP-2 the Ce/Zr molar ratios from EDX measurements exceeded to a greater extent the Ce/Zr ratios obtained from ICP-OES

measurements (Table 3.7). Obviously, the treatment of Ce-Zr-hydroxides with  $H_3PO_4$  solutions provoked textural modifications.

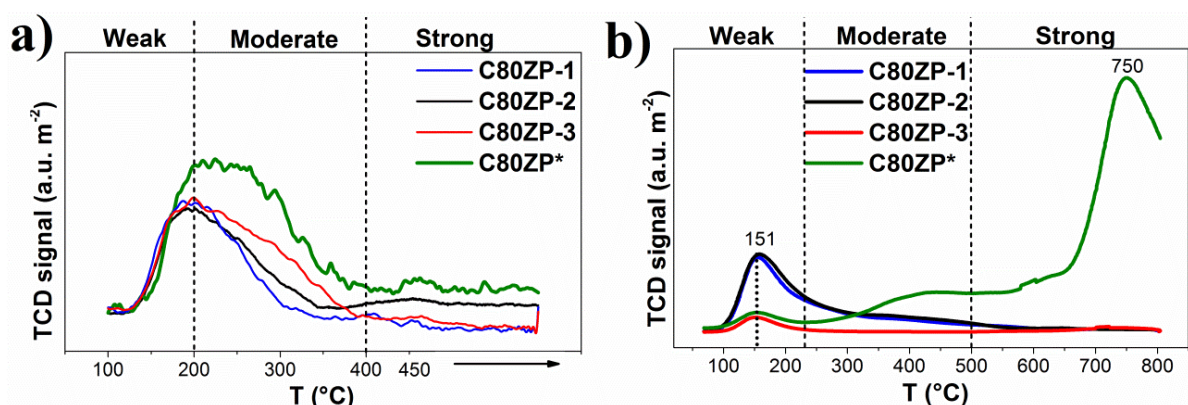
### ***Acid-base properties: Temperature-programmed desorption (TPD) of $NH_3$ and $CO_2$***

Temperature-programmed desorption (TPD) of  $NH_3$  is a suitable characterization technique to estimate the total acidity of the catalysts (Table 3.8).

**Table 3.8.** Acidic and base characteristics of the P-modified C80Z samples.  $T_{max}(NH_3)$  and  $T_{max}(CO_2)$  stand for temperature of maximal  $NH_3$  and  $CO_2$  desorption, respectively.

Sample	Total basicity ( $CO_2$ -TPD)		Total acidity ( $NH_3$ -TPD)	
	$CO_2$ desorbed ( $\mu mol\ g^{-1}$ )	$CO_2$ desorbed ( $\mu mol\ m^{-2}$ )	$NH_3$ desorbed ( $\mu mol\ g^{-1}$ )	$NH_3$ desorbed ( $\mu mol\ m^{-2}$ )
C80ZP-1	35.4	0.5	120	1.6
C80ZP-2	30	0.5	110	1.7
C80ZP-3	6.1	0.1	170	2.3
C80ZP*	48	2.2	100	4.5

The obtained  $NH_3$ -TPD profiles of the surface modified Ce-Zr mixed oxides are displayed in (Figure 3.6a). Depending on desorption temperature range the presence of acid sites can be classified as weak, moderate and strong [67]. P-modified solids exhibit mainly weak (<200 °C) and moderate (200-400 °C) acid sites. However, the concentration and distribution of acidic sites depend upon the Ce/Zr ratio and P-modification.



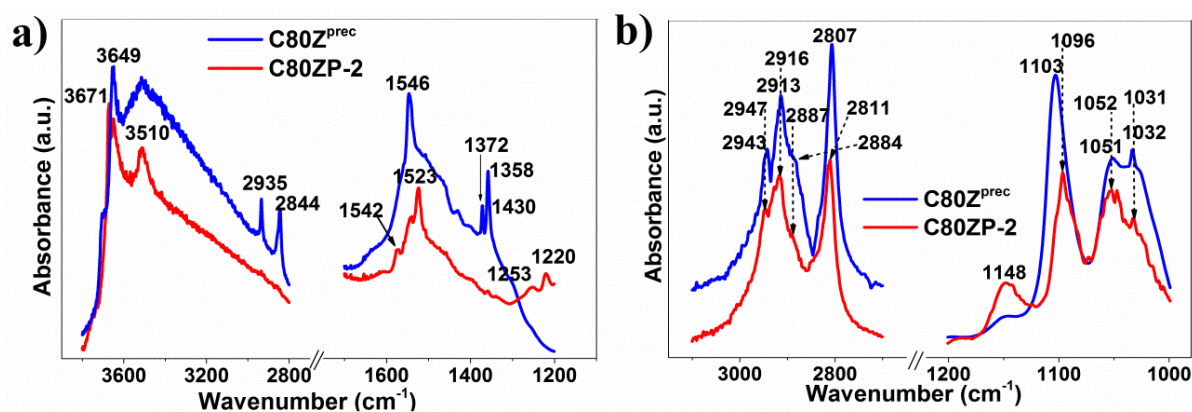
**Figure 3.6.** (a)  $NH_3$ -TPD profiles of P-modified  $Ce_{0.8}Zr_{0.2}O_2$  solids (b)  $CO_2$ -TPD profiles of P-modified  $Ce_{0.8}Zr_{0.2}O_2$  solids.



Figure 3.6b shows  $CO_2$ -TPD profiles of P-modified  $Ce_{0.8}Zr_{0.2}O_2$  mixed oxides. The C80ZP1-3 samples exhibit  $CO_2$  desorption at around 151 °C that indicates the presence of only weak basic sites (<230 °C), whereas this feature is distinctly reduced for C80ZP-3. This suggests that P-modification from hydroxide derived catalyst suppresses the concentration of both moderate and strong basic sites which is not the case for C80ZP\*.

### Fourier Transform Infrared Spectroscopy (FTIR)

In order to further analyze the surface properties (hydroxyl groups and possible carbonate surface species) of C80Z<sup>prec</sup> and C80ZP-2, *in situ* FTIR analysis using synthetic air (400 °C) was performed. The corresponding FTIR spectra of the pretreated samples at 170 °C are shown in Figure 3.7a.



**Figure 3.7.** (a) *In situ* FTIR spectra of C80Z<sup>prec</sup> and C80ZP-2 recorded at 170 °C after pretreatment in synthetic air at 400 °C (b) *In situ* FTIR of C80Z<sup>prec</sup> and C80ZP-2 recorded after 30 min exposure to MeOH/ $CO_2$  at 170 °C and subsequent flushing with He.

Compared to C80Z<sup>prec</sup>, the C80ZP-2 catalyst shows additional bands at 3671  $cm^{-1}$  ( $\nu$ Zr-OH) [144] and 3510  $cm^{-1}$ , besides a band at 3649  $cm^{-1}$  ( $\nu$ Ce-OH) [144]. A band at 3649  $cm^{-1}$  can be assigned to a  $\nu$ OH band from a cerium hydroxide phase [145]. In addition, the ( $\nu$ C-H) bands at 2935, 2844, and 2723  $cm^{-1}$  in C80Z<sup>prec</sup> are due to formate species [146, 147], the respective  $\nu_{as}/\nu_s COO^-$  bands that appear at 1546 and 1372/1358  $cm^{-1}$ . For C80ZP-2 sample these formate bands are missing. Instead, bands at 1542/1523  $cm^{-1}$  and 1253/1220  $cm^{-1}$  appeared. These bands pointed to surface bidentate carbonate species, which could be resulted from oxidation of formate species [148].

For possible correlation of DMC formation from methanol and  $CO_2$  with specific adsorbates species, *in situ* FTIR experiments were performed in which MeOH/ $CO_2$  gas mixtures were adsorbed exemplarily on C80Z<sup>prec</sup> and C80ZP-2 solids at 170 °C. Under these

conditions both catalysts are also active in the conversion of  $CO_2$  with methanol. The corresponding spectra are shown in Figure 3.7b. Methanol can be adsorbed in a dissociative form over the catalyst surface thus giving methoxy species. The bands in the  $\nu C-H$  region around 2940, 2915, and 2810  $cm^{-1}$  are due to C-H stretching vibrations of methoxy species, whereas the bands in the frequency range of 1200-1000  $cm^{-1}$  can be assigned to  $\nu C-O$  vibrations [149]. Based on the  $\nu C-O$  band positions, it is possible to estimate the nature of surface methoxides. Hence, the bands at 1150 and 1100  $cm^{-1}$  are assigned to monodentate methoxy species, whereas the bands around 1050/1030  $cm^{-1}$  are related to bidentate methoxy species adsorbed on  $Zr^{4+}$  or/and  $Ce^{4+}$  [144, 150]. Depending upon the band positions of the monodentate methoxy species it is possible to distinguish between  $Ce^{4+}-OCH_3$  (1103  $cm^{-1}$ ) [150] and  $Zr^{4+}-OCH_3$  (1148  $cm^{-1}$ ) [144]. The FTIR spectrum of  $C80Z^{prec}$  is characterized by a strong band of  $Ce^{4+}-OCH_3$  and only a weak band of  $Zr^{4+}-OCH_3$  species. Moreover, the latter is essentially more intensive over  $C80ZP-2$ . For  $C80Z^{prec}$  the bands due to formate species at 1546 and 1372/1358  $cm^{-1}$  (not shown on Figure 3.7) disappeared, instead, the bands in the range of 1600-1300  $cm^{-1}$  were found due to carbonate species most probably resulted from oxidation of both methoxy and formate species.

**Table 3.9.** Surface properties of the unmodified  $C80Z^{prec}$  and P-modified  $C80ZP-2$  samples examined by MeOH/ $CO_2$  (FTIR) and pyridine adsorption (Py-IR).

Sample	Methoxy formation	Lewis acidity
	Intensity ratio $\nu C-O^a$ $Ce^{4+} / Zr^{4+}$	Band intensity <sup>b</sup> (pyridine ads.)
$C80Z^{prec}$	40 / 1	15.9
$C80ZP-2$	2 / 1	30.5

<sup>a</sup> Ratio of  $\nu C-O$  band intensities ( $\sim 1100$   $cm^{-1}$  and 1150  $cm^{-1}$ ), normalized to BET-SA

<sup>b</sup> Band intensity  $\times 10^{-3}$  (1440  $cm^{-1}$ ), normalized to BET-SA

When comparing the FTIR spectra of pure  $C80Z^{prec}$  and P-modified  $C80ZP-2$ , it is obvious that the overall intensities of the methoxy bands on the surface of  $C80ZP-2$  decreases. However, the intensity ratio of the  $Ce^{4+}/Zr^{4+}-OCH_3$  bands changes dramatically by  $H_3PO_4$  modification in favor of  $Zr^{4+}-OCH_3$  (Table 3.9). This goes well along with an increasing Lewis acidity (Py-IR, Figure A3.1.3) caused by higher percentage of unsaturated surface  $Zr^{4+}$  cations in the modified  $C80ZP-2$  sample. A possible correlation between the adsorbates species and catalyst performance is discussed in next section.



### 3.2.2. Catalytic results

Table 3.10 compares the DMC yields obtained over three P-modified C80ZP samples obtained from  $H_3PO_4$  pretreatment of Ce-Zr hydroxide precursors with varying P/Zr ratios (C80ZP1-3). Furthermore, the DMC yield of another catalyst (C80ZP\*) is also shown. Note that the C80ZP\* catalyst was prepared by post-treatment of  $C80Z^{prec}$  with  $H_3PO_4$ . Ce-Zr precursor was modified initially by  $H_3PO_4$  keeping the ratio of P/Zr=0.03 (C80ZP-1). However, this catalyst didn't show any enhancement in DMC yield (0.24%) with respect to unmodified  $C80Z^{prec}$ . Nevertheless, in further attempts the P-content in the total catalyst was optimized by means of varying P/Zr ratios (P/Zr = 0.12 and 0.3). With this intention,  $Ce_{0.8}Zr_{0.2}O_2$  solid was modified with varying P-contents at varying stages. For instance, phosphorous is added to both uncalcined as well as calcined (post treated) samples and checked its influence on the catalytic performance and in particularly on the yield of DMC.

**Table 3.10.** Influence of the different P/Zr ratios in  $Ce_{0.8}Zr_{0.2}O_2/H_3PO_4$  catalysts on the yield of DMC (Reaction conditions: catalyst weight 50 mg,  $CH_3OH$  = 247 mmol,  $T$  = 170 °C,  $p$  = 65 bar,  $t$  = 1 h, 600 rpm).

Sample	P/Zr	Y-DMC (mol%)
C80ZP-1	0.03	0.24
C80ZP-2	0.12	1.62
C80ZP-3	0.3	0.11
C80ZP*	0.12	0.004

In contrast to the unmodified  $C80Z^{prec}$ , the phosphoric acid treated sample C80ZP-2 showed an extraordinary increase in the yield of DMC reaching ~ 1.62%, which is nearly four times higher than that for the unmodified  $C80Z^{prec}$  sample. The BET-SA increased for all P-modified C80ZP samples compared to their parent  $C80Z^{prec}$  solid. The surface composition is also altered to a certain extent. In fact, there is a clear enrichment of Ce in the P-modified C80ZP-2 sample compared to its parent  $C80Z^{prec}$  solid. From adsorption spectra of MeOH/ $CO_2$  mixture, the decrease of the overall intensities of the methoxy bands for C80ZP-2 could be found. However, the intensity ratio of the  $Ce^{4+}/Zr^{4+}-OCH_3$  bands changes dramatically by  $H_3PO_4$  modification in favor of  $Zr^{4+}-OCH_3$  (Table 3.9). An increasing Lewis acidity in the modified C80ZP-2 sample is also observed.  $CO_2$ - and  $NH_3$ -TPD results confirmed that the total basicity decreased by modification while the overall acidity did not change dramatically (Table 3.8). Based on the work of Tomishige *et al.* [87] intermediate methoxy carbonate species are easily formed over  $ZrO_2$  catalysts by reaction of adsorbed

monodentate methoxy species with  $CO_2$ . It can be concluded that the favored formation of  $Zr^{4+}$ -OCH<sub>3</sub> species is responsible for the increased yield of DMC over C80ZP-2 catalyst.

The yield of DMC significantly increases with increasing P/Zr ratio and reaches a maximum at composition of P/Zr=0.12 (C80ZP-2;  $Y_{DMC} = 1.62\%$ ). A further increase in the P/Zr ratio to 0.3 resulted in a significant decrease in the DMC yield. Ikeda *et al.* [124] reported similar findings for the  $ZrO_2/H_3PO_4$  system: catalysts with low P/Zr ratio (0.025-0.1) were more effective for DMC formation compared to un-phosphated  $ZrO_2$ . A considerably lower DMC yield (0.004 mol%) was obtained over the post-treated C80ZP\*. A similar effect of post-treatment was also observed in phosphated zirconia catalysts by other researchers [96], where the active sites were formed by the interaction between  $H_3PO_4$  and Zr hydroxides during catalyst preparation. XPS results suggest that post-treated sample C80ZP\* has high content of P (21 mol%) concentrated on its surface and high surface acidic characteristics of resulting solids. In contrast, on the surface of pretreated C80ZP-2 solid, the concentration of P was lower (5 mol%) than on post-treated sample with identical nominal P content. Thus, the presence of high concentration of acid sites on CZ80P\* surface ( $4.5 \mu\text{mol NH}_3 \text{ m}^{-2}$ ) could be responsible for lower catalytic activity towards DMC. As a conclusion i) the method of  $H_3PO_4$  treatment plays an important role and ii) a certain amount of phosphorus in the  $C80Z^{prec}$  catalyst (P/Zr=0.12) is essential for proper catalytic activity.

### 3.3. Summary

The effects of Ce content in Ce-Zr mixed oxides and their surface functionalization with phosphoric acid on the DMC yield in liquid phase carboxylation of methanol were investigated. DMC was not formed over pure  $ZrO_2$  catalyst. However, the yield of DMC is greatly affected by the introduction of  $Ce^{4+}$  into  $ZrO_2$ , thus it was enhanced from 0.04% over  $C20Z^{prec}$  to 0.24% over  $C60Z^{prec}$  and remained the same over  $C80Z^{prec}$  and  $C^{prec}$ . Tetragonal  $Ce_xZr_{1-x}O_2$  phase was mainly formed by the high Zr content ( $x \leq 0.4$ ), whereas the cubic  $Ce_xZr_{1-x}O_2$  phase was predominant at higher Ce proportion ( $x > 0.4$ ). To explore acid-base properties, TPD analysis was performed.  $CO_2$  was desorbed in a broad temperature range (100-800 °C) and three types of basic sites were suggested to present on the surface of  $Ce_xZr_{1-x}O_2$  materials: weak, moderate and strong.  $Ce_xZr_{1-x}O_2$  solids with high Zr content exhibited high concentration of  $CO_2$  desorption, predominantly strong.  $NH_3$ -TPD profiles of all  $Ce_xZr_{1-x}O_2$  catalysts are characterized by a broad  $NH_3$  desorption peak with a maximum at 200 °C. Both weak and medium strength acidic sites were identified. Pure  $ZrO_2$  showing poor

catalytic performance had the highest concentration of acidic sites ( $4.4 \mu\text{mol m}^{-2}$ ). The DMC formation is greatly depends on the presence of both acid-base sites on the surface of catalyst, since this reaction is catalyzed simultaneously by acidic and basic sites. Based on mechanism of DMC formation proposed by Tomishige *et al.* [87],  $CO_2$  is activated on basic sites to form  $CO_2^-$  ions, whereas MeOH is activated at both acidic and basic sites to form a methyl and methoxy species, respectively. In order to realize the high DMC yield simultaneous activation of both MeOH and  $CO_2$  is required. Furthermore, nearly equal amount of acidic and basic sites is efficient for DMC formation. In a case when one kind of active sites exceeds the other on the surface of catalyst, only an activation of one reactant is dominant. In this work the presence of strong acidic and/or basic sites has a negative effect on the DMC formation. This suggests that temperature at which  $CO_2$  and  $NH_3$  desorbed from catalyst surface during TPD analyses is related to the activation of  $CO_2$  and MeOH. The higher is desorption temperature during TPD the lower is DMC yield. In the present study the  $Ce_xZr_{1-x}O_2$  catalyst with the acid-basic sites of weak to medium strength (100-400 °C) was favorable for DMC formation, since DMC is catalyzed at temperature of 170 °C and does not involve the temperature region of strong acidity/basicity (400-600 °C).  $C60Z^{prec}$ ,  $C80Z^{prec}$ ,  $C^{prec}$  catalysts having the right balance of the weak and moderate acid/base sites showed high DMC yield.

The effect of surface phosphated Ce-Zr mixed oxides on the carboxylation of methanol was investigated. Phosphate modification of Ce-Zr precursors resulted in a noticeable promotion of catalytic performance compared to their corresponding unmodified  $C80Z^{prec}$ . Structural and textural changes were noticed in P-modified  $C80Z^{prec}$  solids. BET-surface area increased for all samples after the P-modifications. As revealed by XRD, after phosphoric acid treatment the phase composition and crystallite size were also changed leading to Ce-rich cubic and Zr-rich tetragonal  $Ce_xZr_{1-x}O_2$  nanophases with intimate contact on the nanoscale but they do not exhibit the primary influence on DMC yield. The high DMC yield was related to the changed surface properties. The ICP and XPS studies revealed that the bulk P/Zr ratio was much lower than the surface P/Zr ratio indicating the concentration of P mostly on the surface. Moreover, surface enrichment of Ce is also noticed with P-modification, which also promoted the catalytic performance.

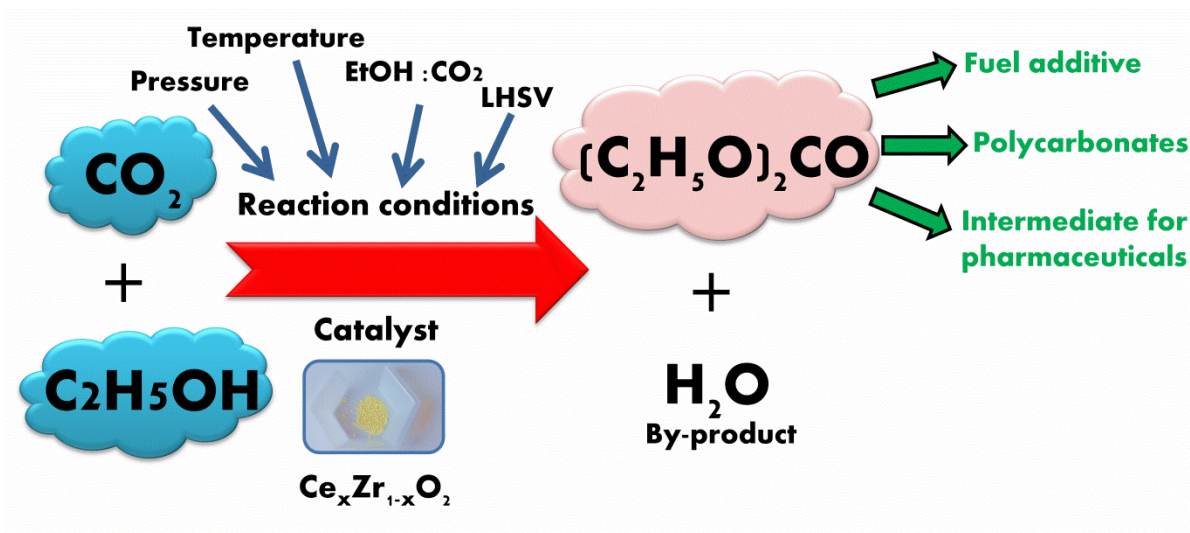
In subsequent efforts on the optimization of P/Zr ratios, the yield of DMC over  $C80ZP-2$  (P/Zr = 0.12) was further enhanced to 1.62%. The acid treatment caused a decrease of moderate and strong basic sites and an increase of Lewis acidic sites from most likely unsaturated surface  $Zr^{4+}$  cations that are responsible for an enhanced ability to form

monodentate methoxy species as an intermediate of the catalytic cycle. Besides, the effect of P-addition to an already calcined  $C80Z^{prec}$  sample was investigated. It was found that the introduction of phosphate ions on the surface of calcined  $C80Z^{prec}$  (post-treatment) caused a decrease of DMC formation compared to its addition on uncalcined samples. This result also suggests that the amount of P and its addition at a suitable stage during their preparation is crucial for tuning the catalytic properties of Ce-Zr-O solids and also to improve the yield of DMC to a considerable extent.

## Chapter 4

### 4. Continuous synthesis of diethyl carbonate from ethanol and CO<sub>2</sub> over Ce<sub>x</sub>Zr<sub>1-x</sub>O<sub>2</sub> (x = 0, 0.2, 0.5, 0.8, 1) catalysts

Chapter 4 deals with preparation of Ce<sub>x</sub>Zr<sub>1-x</sub>O<sub>2</sub> (x = 0, 0.2, 0.5, 0.8 and 1.0) materials by a citrate method and their characterization by various techniques such as N<sub>2</sub>-adsorption (BET-SA), XRD, XPS, ICP-OES, TEM, H<sub>2</sub>-TPR, NH<sub>3</sub>- and CO<sub>2</sub>-TPD. In addition, the potential of such materials is evaluated for the direct synthesis of diethyl carbonate (DEC) from ethanol and CO<sub>2</sub> under continuous-flow conditions in a plug-flow reactor (PFR). According to the thermodynamic data, the reaction is favourable at low temperatures but high pressures. Thus, catalytic experiments were carried out at temperatures in the range between 80 and 180 °C and at pressures between 80 and 180 bar.



## 4.1. An effective Ce<sub>x</sub>Zr<sub>1-x</sub>O<sub>2</sub> catalysts for the continuous synthesis of DEC from CO<sub>2</sub> and ethanol : effect of varying reaction conditions

### 4.1.1. Catalysts characterization

#### *BET surface area*

Ce<sub>x</sub>Zr<sub>1-x</sub>O<sub>2</sub> catalysts were prepared by citrate complexation method from Ce(NO<sub>3</sub>)<sub>3</sub>•6H<sub>2</sub>O and ZrO(NO<sub>3</sub>)<sub>2</sub>•4H<sub>2</sub>O by addition of citric acid as a chelating agent. Table 4.1 compares the surface areas, average pore sizes, pore volumes and crystalline size between pure CeO<sub>2</sub> or ZrO<sub>2</sub> and Ce<sub>x</sub>Zr<sub>1-x</sub>O<sub>2</sub> catalysts. BET surface areas were found to depend on the content of Ce in the catalysts. In a case of pure oxides, C-citrate (CeO<sub>2</sub>) shows much lower SA compared to Z-citrate (ZrO<sub>2</sub>). As a result, the surface area of prepared Ce–Zr mixed oxides was established to decrease with increasing Ce content due to the poor resistivity of cerium-rich solids against sintering as claimed elsewhere [151].

**Table 4.1.** Effect of Ce loading on textural properties and crystallite size of Ce<sub>x</sub>Zr<sub>1-x</sub>O<sub>2</sub> solids.

Sample	x in Ce <sub>x</sub> Zr <sub>1-x</sub> O <sub>2</sub>	BET-SA (m <sup>2</sup> g <sup>-1</sup> )	Average pore d (nm)	Total pore V (cm <sup>3</sup> g <sup>-1</sup> )	D (nm)
Z-citrate	0	88	2.8	0.069	3.8
C20Z citrate	0.2	79	2.8	0.060	4.6
C50Z-citrate	0.5	57	4.2	0.064	4.8
C80Z-citrate	0.8	42	6.2	0.076	6.0
C-citrate	1.0	27	5.3	0.036	9.0

The size of crystallites of Ce<sub>0.18</sub>Zr<sub>0.82</sub>O<sub>2</sub>, Ce<sub>0.5</sub>Zr<sub>0.5</sub>O<sub>2</sub> and Ce<sub>0.75</sub>Zr<sub>0.25</sub>O<sub>2</sub>, as well as the volume of pores of the corresponding mixed solids were found to vary in a narrow range from 4.6 to 6.0 nm and from 0.060 to 0.076 cm<sup>3</sup> g<sup>-1</sup>, respectively. These two parameters are however dependent upon Ce content in the system. Pure ZrO<sub>2</sub> possesses the smallest crystallite size of 3.8 nm and the highest pore volume of 0.069 cm<sup>3</sup> g<sup>-1</sup>, whereas CeO<sub>2</sub> exhibits the largest crystallite size of 9 nm and the lowest pore volume of 0.036 cm<sup>3</sup> g<sup>-1</sup> in the range of mixed oxides. In addition, it was found that mesopores are present in all Ce<sub>x</sub>Zr<sub>1-x</sub>O<sub>2</sub> samples. The mixture of zirconium and cerium suppresses the crystal growth during catalyst preparation and enhances the stability of mixed oxides, compared to their parent oxides. It well-known that thermal stability and redox nature of pure CeO<sub>2</sub> is limited because of the decrease of SA at higher calcination temperature due to nucleation and growth of crystallites

of ceria within the pore [152, 153]. As was reported by Hori *et al.* [154], the addition of Zr<sup>4+</sup> into ceria can improve these properties.

### X-ray diffraction (XRD)

XRD patterns of different Ce<sub>x</sub>Zr<sub>1-x</sub>O<sub>2</sub> catalysts are shown in Figure 4.1. Reflexes in the XRD pattern of the sample C-citrate can be attributed to the cubic CeO<sub>2</sub> phase [29, 155]. After zirconium loading into CeO<sub>2</sub>, the main reflexes of this phase shift to higher diffraction angles due to changes of unit cell parameters and lattice deformation [156-158]. This shift can be attributed to a progressive substitution of Ce<sup>4+</sup> (ionic radius 0.097 nm) with smaller Zr<sup>4+</sup> (ionic radius 0.084 nm) [127, 128, 159].

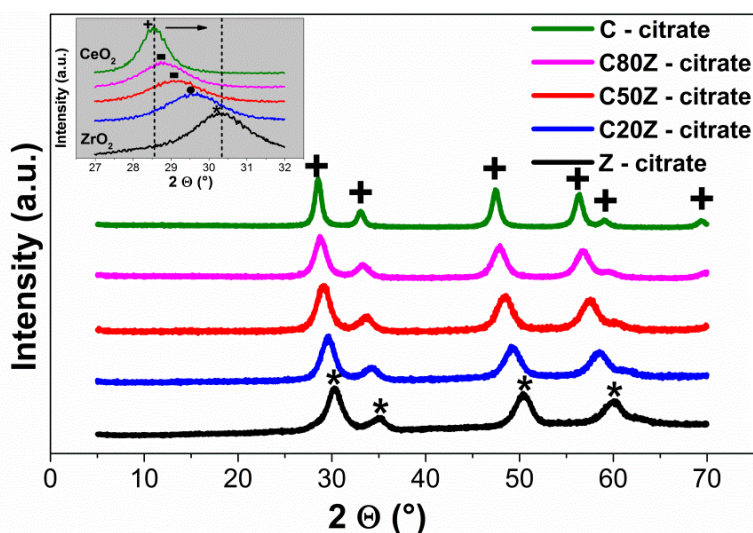


**Figure 4.1.** XRD patterns of Ce<sub>x</sub>Zr<sub>1-x</sub>O<sub>2</sub> catalysts. Phase composition: + cubic CeO<sub>2</sub> (JCPDS 65-5923), \* tetragonal ZrO<sub>2</sub> (JCPDS 79-1769). Inset: ■ c-Ce-Zr-O mixed phase (c-Ce<sub>0.75</sub>Zr<sub>0.25</sub>O<sub>2</sub> (JCPDS 28-271)), ● t-Ce-Zr-O mixed phase (t-Ce<sub>0.18</sub>Zr<sub>0.82</sub>O<sub>2</sub> (JCPDS 80-785), t-Ce<sub>0.5</sub>Zr<sub>0.5</sub>O<sub>2</sub> (JCPDS 38-1436)).

In accordance to the work of Yashima *et al.* [160], the phase transitions occurring in Ce<sub>x</sub>Zr<sub>1-x</sub>O<sub>2</sub> depend on their composition. The cubic single Ce<sub>x</sub>Zr<sub>1-x</sub>O<sub>2</sub> (C50Z-citrate and C80Z-citrate) phase is formed at and above 50 mol% of Ce, while below 50 mol%, a tetragonal Ce<sub>x</sub>Zr<sub>1-x</sub>O<sub>2</sub> (e.g. C20Z-citrate) phase is appeared [127, 158, 161]. There is no evidence for phase segregation in wide range of composition. For pure ZrO<sub>2</sub> (Z-citrate) the diffraction patterns can be assigned to the tetragonal ZrO<sub>2</sub> structure [155].

### ***Elemental analysis by Inductively coupled plasma optical emission spectroscopy (ICP-OES) and X-ray photoelectron spectroscopy (XPS)***

Table 4.2 compares the bulk and surface atomic ratios of Ce/Zr determined from ICP and XPS measurements of Ce<sub>x</sub>Zr<sub>1-x</sub>O<sub>2</sub> samples. It can be observed, that the Ce/Zr surface ratios for all mixed oxides are significantly lower than the corresponding bulk ratios indicating on the clear enrichment of zirconium in the near-surface-region. However, the surface Ce/Zr ratio for Ce<sub>0.8</sub>Zr<sub>0.2</sub>O<sub>2</sub> catalyst is in very close agreement with the nominal value. The similar decrease in surface Ce/Zr ratio for Ce<sub>x</sub>Zr<sub>1-x</sub>O<sub>2</sub> solids was observed in previous Chapter 3 that indicated on the migration of zirconium from the bulk to the surface.

**Table 4.2.** Comparison of molar Ce/Zr ratios in the near-surface-region (as measured by XPS) with bulk composition (as measured by ICP) for Ce<sub>x</sub>Zr<sub>1-x</sub>O<sub>2</sub> solids.

Sample	Ce/Zr ratio nominal	Ce/Zr ratio (XPS)	Ce/Zr ratio (ICP)	Ce/Zr ratio (EDX)
C80Z-citrate	4	3.9	5.34	3.9, 6.1*
C50Z-citrate	1	0.7	1.3	
C20Z-citrate	0.25	0.11	0.41	

\*Selected areas for the calculation of Ce/Zr are labelled on Figure 4.3

### ***Transmission electron microscopy (TEM)***

TEM (Transmission Electron Microscopy) studies were performed on the pure oxides C-citrate and Z-citrate as well on C80Z-citrate in order to get more insight into elemental composition and particle size. The TEM images are displayed in Figure 4.3 revealing nanometer sized particles. The particle size of CeO<sub>2</sub> is about 8 nm, which is quite close to the crystallite size calculated from Scherrer equation (9 nm). In case of C80Z-citrate particle, the size of about 5 nm was determined. As for the pure individual oxides, Ce-Zr-O particles are also not uniform in shape.

EDX results for C80Z-citrate catalyst confirmed that the distribution of cerium and zirconium concentrations within the selected region is not uniform. In 2a(1) region the molar Ce/Zr ratio was found to be 3.9 which is close to nominal one, whereas 2a(2) region represented Ce-enrichment with Ce/Zr molar ratio of 6.1.



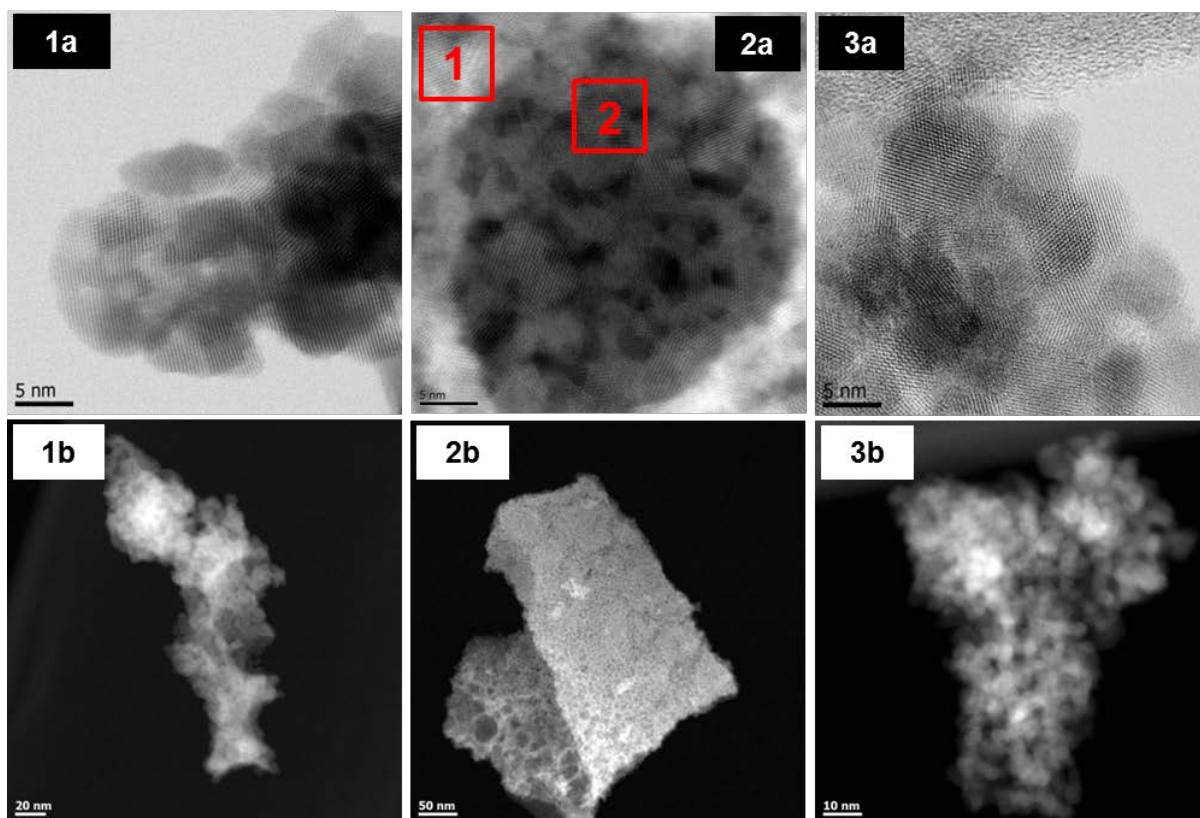


**Figure 4.3.** ABF-STEM (a) and HAADF-STEM (b) images of (1) C-citrate, (2) C80Z-citrate, (3) Z-citrate.

### *Temperature-programmed reduction (TPR) by H<sub>2</sub>*

The redox properties of the Ce<sub>x</sub>Zr<sub>1-x</sub>O<sub>2</sub> solids were investigated by means of temperature-programmed reduction (TPR) experiments using a feed (50 mL min<sup>-1</sup>) with 5 vol% H<sub>2</sub> in Ar. Figure 4.4 displays the TPR profiles of the Ce<sub>x</sub>Zr<sub>1-x</sub>O<sub>2</sub> catalysts with the various temperature regions of catalyst reduction.

It is known that cerium can exist in Ce<sub>x</sub>Zr<sub>1-x</sub>O<sub>2</sub> solid solutions as Ce<sup>3+</sup> and Ce<sup>4+</sup> ions while zirconium exists as Zr<sup>4+</sup> only [162]. Pure CeO<sub>2</sub> (C-citrate) has a high oxygen storage/release capacity compared to pure ZrO<sub>2</sub> [163], since ceria can store the oxygen in aerobic conditions and release the oxygen in anaerobic conditions in order to satisfy its stoichiometry [164]. These redox properties can strongly be enhanced when Zr<sup>4+</sup> cations are introduced into the CeO<sub>2</sub> lattice owing to improving oxygen ion mobility in the modified Ce-Zr-O lattice. The substitution of Ce<sup>4+</sup> (radius 0.097nm) with the smaller Zr<sup>4+</sup> cation (radius 0.084 nm) causes shrinking of the CeO<sub>2</sub> fluorite-type lattice, formation of structural defects and alteration of surrounded oxygen [136, 162, 165]. Moreover, the presence of Zr<sup>4+</sup> in CeO<sub>2</sub> decreases the surface reduction temperature of Ce<sup>4+</sup> and also increases the total amount of reduced cerium.

The reduction process of pure CeO<sub>2</sub> (C-citrate) is well-known to occur in two steps. The first region is located between 350 and 600 °C with T<sub>max</sub> of around 452 °C and second region starts from 600 °C with T<sub>max</sub> of around 792 °C. The low-temperature peak is related to the removal of surface lattice oxygen of CeO<sub>2</sub>, while the high-temperature signal at 792 °C is caused by the removal of bulk lattice oxygen [166]. The small peak centered at 224 °C was associated with the reduction of the outermost layer of Ce<sup>4+</sup> (surface reduction) [163]. The reduction of pure ZrO<sub>2</sub> was negligible (small peak at 582 °C). However, the incorporation of Zr<sup>4+</sup> to CeO<sub>2</sub> promoted the reduction of pure CeO<sub>2</sub>. In contrast to the TPR profile for pure CeO<sub>2</sub>, the mixed Ce<sub>x</sub>Zr<sub>1-x</sub>O<sub>2</sub> oxides show a main broad reduction feature in the region between 500–530 °C with different T<sub>max</sub> values. Based on results obtained by de Rivas *et al.* [167, 168], the addition of Zr<sup>4+</sup> to CeO<sub>2</sub> causes a reduction of surface and bulk in one step at moderate temperatures. In addition, some H<sub>2</sub> consumption can be observed at higher temperatures for C80Z-citrate and C50Z-citrate, but to a lower extent than for CeO<sub>2</sub>. Furthermore, the position of surface reduction peak shifted from 452 to 508 °C with increasing of zirconium content. It was found that the extent of the reduction was the highest for C50Z-citrate sample. In addition, the weak peak at 360 °C can be attributed to the reduction of Ce<sup>4+</sup> located in a different chemical environment, such as subsurface region [169].

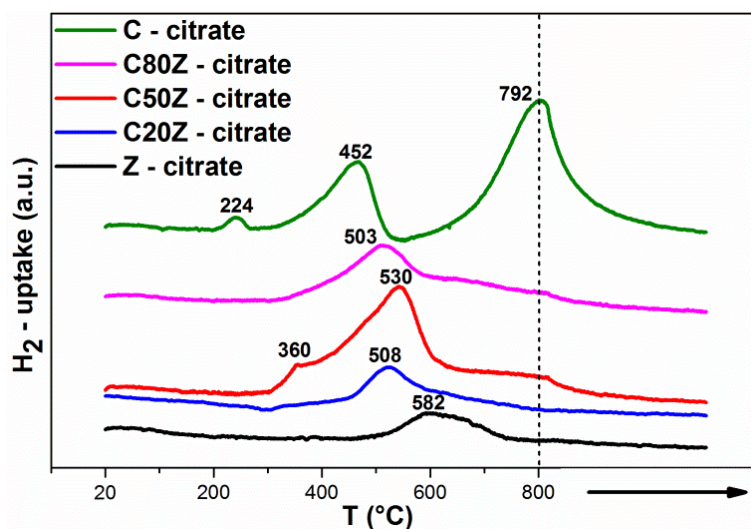


**Figure 4.4.** H<sub>2</sub>-TPR profiles of different Ce<sub>x</sub>Zr<sub>1-x</sub>O<sub>2</sub> solids. (→: indicates isothermal treatment of the samples at 800 °C for 2 h).

In addition, the total amount of hydrogen consumed by the catalysts and T<sub>max</sub> values are summarized in Table 4.3. An increase in the H<sub>2</sub> uptake from 1.15 mmol g<sup>-1</sup> for pure ceria (C-citrate) to 1.793 mmol g<sup>-1</sup> for C50Z-citrate provides hints to an enhanced reducibility of

CeO<sub>2</sub> caused by the addition of Zr<sup>4+</sup> to CeO<sub>2</sub> [167]. Obviously the H<sub>2</sub> consumption progressively reduces with increase in zirconium content above 50 mol%. For pure ZrO<sub>2</sub> (Z-citrate) the H<sub>2</sub> consumption was only 0.192 mmol g<sup>-1</sup>. This result indicates that under the conditions applied the Zr<sup>4+</sup> cations are hardly reduced.

**Table 4.3.** H<sub>2</sub> uptake and temperature of maximal hydrogen consumption (T<sub>max</sub>) during TPR runs for Ce<sub>x</sub>Zr<sub>1-x</sub>O<sub>2</sub> solids.

Sample	H <sub>2</sub> -uptake (mmol g <sup>-1</sup> )	T <sub>max</sub> (°C)
Z-citrate	0.192	582
C20Z-citrate	0.704	508
C50Z-citrate	1.793	530
C80Z-citrate	1.482	503
C-citrate	0.015, 0.271, 0.869	224, 452, 792

### ***Acid-base properties: Temperature-programmed desorption (TPD) of NH<sub>3</sub> and CO<sub>2</sub>***

The total concentration and the strength of acidic sites on the surface of Ce<sub>x</sub>Zr<sub>1-x</sub>O<sub>2</sub> solids were determined by NH<sub>3</sub>-TPD (i.e. expressed as the amount of NH<sub>3</sub> desorbed per gram and per square meter of catalyst) and given in Table 4.4.

**Table 4.4** Acid-base characteristics of Ce<sub>x</sub>Zr<sub>1-x</sub>O<sub>2</sub> solids. T<sub>max</sub> (NH<sub>3</sub>) and T<sub>max</sub> (CO<sub>2</sub>) stand for temperature of maximal NH<sub>3</sub> and CO<sub>2</sub> desorption, respectively.

Sample	NH <sub>3</sub> desorbed (μmol g <sup>-1</sup> / μmol m <sup>-2</sup> )	T <sub>max</sub> (NH <sub>3</sub> ) (°C)	CO <sub>2</sub> desorbed (μmol g <sup>-1</sup> / μmol m <sup>-2</sup> )	T <sub>max</sub> (CO <sub>2</sub> ) (°C)
Z-citrate	185 / 2.1	230	112 / 1.3	168, 584
C20Z-citrate	130 / 1.7	210, ~450	235 / 3.0	171, 570
C50Z-citrate	118 / 2.1	220, ~450	117 / 2.1	168, 637
C80Z-citrate	94 / 2.2	220	104 / 2.5	163, 618
C-citrate	34 / 1.3	200	52 / 1.9	149, 589

The acidic properties of the solids are strongly affected by the presence of zirconium in the lattice of CeO<sub>2</sub> [170], since pure ZrO<sub>2</sub> and CeO<sub>2</sub> have different lattice potentials and incorporation of one oxide matrix into the other cause a generation of new surface acidic sites in the solid solution as per Kung's model [131, 171]. From Table 4.4 it is evident that pure ZrO<sub>2</sub> (Z-citrate) is more acidic (i.e. 2.1 μmol NH<sub>3</sub> m<sup>-2</sup>) than pure CeO<sub>2</sub> (C-citrate). It can be seen that the total acidity was the lowest for solid C-citrate (1.3 μmol NH<sub>3</sub> m<sup>-2</sup>), which is

however considerably improved upon addition of 20 mol% of zirconium, then decreases as Zr content is further increased up to 80 mol%. C80Z-citrate exhibits the highest amount of NH<sub>3</sub> desorbed from its surface (2.2 μmol NH<sub>3</sub> m<sup>-2</sup>). Based on literature [131], the acidic sites are located more in the interior of pores, leading to more physisorption of NH<sub>3</sub>. As in the present case, C80Z-citrate possessed the highest pore volume of 0.076 cm<sup>3</sup> g<sup>-1</sup> compared to other Ce<sub>x</sub>Zr<sub>1-x</sub>O<sub>2</sub> samples.

Figure 4.5 shows the NH<sub>3</sub>-TPD profiles of the Ce<sub>x</sub>Zr<sub>1-x</sub>O<sub>2</sub> solids. It can be seen, that these solids possess acidic sites of different strength. The desorption peaks of TPD profiles located at 100 –200 °C, 200 –400 °C and 400 – 450 °C can be assigned to weak, moderate and strong acid sites, respectively [67]. Both the weak and moderate acid sites were observed for all catalysts. However, the strong acid sites with characteristic desorption temperature of about 450 °C were observed in Z-citrate, C20Z-citrate and C50Z-citrate solids only.

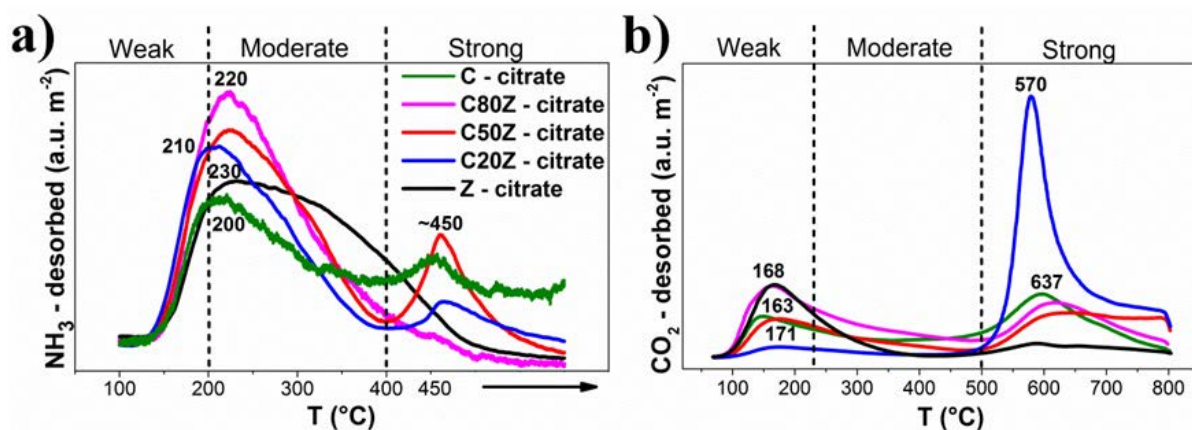


**Figure 4.5.** (a) NH<sub>3</sub>-TPD profiles and (b) CO<sub>2</sub>-TPD profiles of Ce<sub>x</sub>Zr<sub>1-x</sub>O<sub>2</sub> solids.

In order to investigate the effect of Ce content on basic properties, CO<sub>2</sub>-TPD experiments were also studied. CO<sub>2</sub>-TPD profiles of the Ce<sub>x</sub>Zr<sub>1-x</sub>O<sub>2</sub> solids are shown in Figure 4.5b. Ce<sub>x</sub>Zr<sub>1-x</sub>O<sub>2</sub> solids possess basic sites of different types with weak (100-230 °C), moderate (230–500 °C) and strong (above 500 °C) strengths [105, 135]. All Ce-based catalysts exhibit two broad desorption peaks at different temperatures: the low temperature peak was attributed to weak and moderate basic sites, while the high temperature peak was ascribed to strong basic sites.

Table 4.3 lists the amount of CO<sub>2</sub> desorbed during temperature programmed desorption measurements of different Ce<sub>x</sub>Zr<sub>1-x</sub>O<sub>2</sub> solids. It can be seen, that the total concentration of CO<sub>2</sub> desorption from sample Z-citrate is very low (1.3 μmol m<sup>-2</sup>). The basic properties of mixed oxides are improved as the Zr content is increased up to 80 mol%. Among all prepared

mixed oxides, C20Z-citrate exhibited the highest concentration of basic sites (3.0  $\mu\text{mol m}^{-2}$ ), mostly centered in the region of strong basicity (2.9  $\mu\text{mol m}^{-2}$  which is 98% of total basic sites concentration). By comparison the NH<sub>3</sub>- and CO<sub>2</sub>-TPD results, the acid-base properties of pure oxides, i.e. CeO<sub>2</sub> and ZrO<sub>2</sub>, can be significantly modified by their chemical mixing. As the result, mixed Ce<sub>x</sub>Zr<sub>1-x</sub>O<sub>2</sub> catalysts possess both acidic and basic sites of different types. Interestingly the acid-to-base site ratio was about 1 for C80Z-citrate and C50Z-citrate catalysts, which seemed to be optimum for improved catalytic properties.

#### 4.1.2. Catalytic results: effect of Ce/Zr ratio, temperature and pressure on catalytic performance

The present work was focused on transferring the knowledge from batch-reactor approaches to a continuous-flow operation. Thus the contact time of the reagents with the catalyst is a very important parameter to achieve the highest possible DEC yield and space-time-yield as well. From the tests performed over the C80Z-citrate catalyst ( $T_c = 700\text{ }^\circ\text{C}$ ) at 140  $^\circ\text{C}$  and 140 bar and described in Section 4.2, a total flow rate of 42 L<sub>liq.</sub> kg<sub>cat.</sub><sup>-1</sup> h<sup>-1</sup> ( $\tau = 68.6\text{ s}$ , highest  $Y_{\text{DEC}}$  obtained) was identified and selected for the present section. The ratio of EtOH : CO<sub>2</sub> = 1 : 6 was selected for further experiments, since an increase in this ratio leads to a decrease in the DEC yield (see Figure 4.13). The effect of R-OH : CO<sub>2</sub> feed ratio on equilibrium conversion of C<sub>1</sub>-C<sub>2</sub> alcohols was already discussed in literature [172-174]. It was found that the larger is concentration of C<sub>1</sub>-C<sub>2</sub> alcohol in the feed mixture, the higher the temperature (up to the critical temperature of pure R-OH, 240  $^\circ\text{C}$ ) required for conducting the target reaction. Moreover, a decrease of R-OH : CO<sub>2</sub> feed ratio favours the equilibrium C<sub>1</sub>-C<sub>2</sub> alcohols conversion.

Figure 4.6 shows the influence of total reaction pressure ( $p = 80, 110, 140$  or  $180\text{ bar}$ ) and temperature ( $T = 80, 100, 120, 140, 160$  or  $180\text{ }^\circ\text{C}$ ) on DEC formation over C-citrate, C80Z-citrate, C50Z-citrate, C20Z-citrate and Z-citrate catalysts under continuous-flow conditions in a plug flow reactor (tubular reactor). Figure 4.6 shows the influence of pressure and temperature on DEC yield obtained over different Ce<sub>x</sub>Zr<sub>1-x</sub>O<sub>2</sub> catalysts. An increase in DEC yield was determined upon pressure rise up to 140-160 bar depending on Ce content in Ce<sub>x</sub>Zr<sub>1-x</sub>O<sub>2</sub> solid solutions. A further pressure increase up to 180 bar led to a decline in DEC production. Based on phase equilibrium data which are available in the literature [112, 114-117], it was found that supercritical region for C<sub>2</sub>H<sub>5</sub>OH-CO<sub>2</sub> binary system was reached maximum near 160 bar and temperature in a range of 120-160  $^\circ\text{C}$  when initial CO<sub>2</sub> molar



fraction in such system was between 0.7 and 0.9. It was supposed that these trends are still valid for quaternary system, due to the low amounts of DEC (predicted  $x \sim 0.004$  at reaction equilibrium) and H<sub>2</sub>O (predicted  $x \sim 0.004$  at reaction equilibrium). One can also expect that above 160 bar the reaction mixture might be in the liquid or supercritical state, depending upon the system temperature. According to the findings of Hou *et al.* [175] dialkyl carbonate production increased with increasing pressure in the two-phase region, and decreased with pressure in the supercritical region (one phase region).

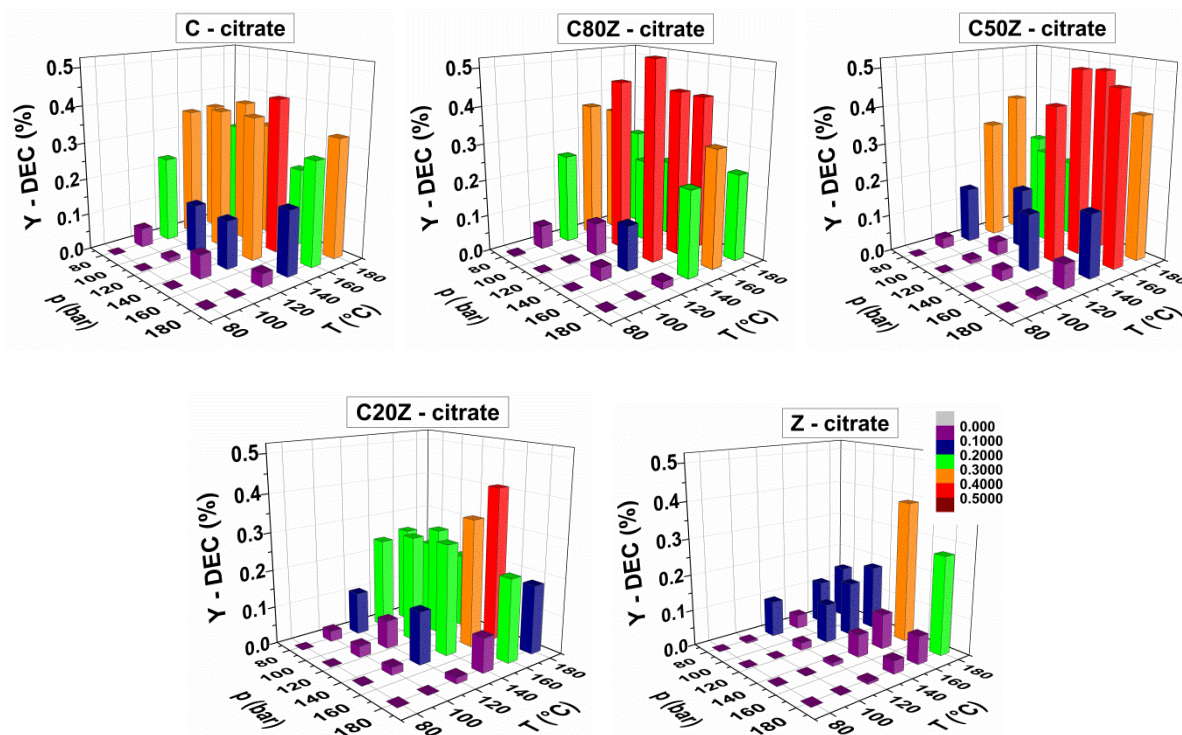


**Figure 4.6.** Effect of reaction pressure and temperature on the yield of DEC over different Ce<sub>x</sub>Zr<sub>1-x</sub>O<sub>2</sub> catalysts. Reaction conditions: catalyst weight 1 g, EtOH : CO<sub>2</sub> = 1 : 6, 1 h time-on-stream, LHSV = 42 L<sub>liq</sub>. kg<sub>cat</sub>.<sup>-1</sup> h<sup>-1</sup>,  $\tau$  = 68.6 s.

The effect of reaction temperature on the desired reaction is more complicated. The yield of DEC gradually increased with reaction temperature up to 140 °C and then dropped to lower values at higher temperatures for C-citrate, C80Z-citrate and C50Z-citrate. Based on the fact that that carboxylation of alcohols is an exothermic reaction, from thermodynamic point of view high reaction temperature is unfavourable for organic carbonates formation [99, 105]. The DEC yield of pure ZrO<sub>2</sub> (Z-citrate) and C20Z-citrate slowly increased with rising temperature in the pressure region of 140-160 bar and reached the highest value of 0.4% at 180 °C. The highest DEC yield over C50Z-citrate (0.48%) and C80Z-citrate (0.5%) catalysts

were achieved at pressure of 160 and 140 bar and temperature of 160 and 140 °C, respectively.

#### 4.1.3. Catalytic results and materials properties affecting the catalyst activity

According to literature [94, 176], DMC and DEC formation over pure CeO<sub>2</sub> and Ce<sub>x</sub>Zr<sub>1-x</sub>O<sub>2</sub> catalysts had been related to its specific surface areas. In this work, the BET-SA of the Ce<sub>x</sub>Zr<sub>1-x</sub>O<sub>2</sub> solids increased with Zr content and reached a maximum value for pure ZrO<sub>2</sub> (Z-citrate). Although C80Z-citrate (42 m<sup>2</sup> g<sup>-1</sup>) and C50Z-citrate (57 m<sup>2</sup> g<sup>-1</sup>) have lower BET-SA in contrast to other Ce<sub>x</sub>Zr<sub>1-x</sub>O<sub>2</sub> catalysts, they exhibited higher DEC yields. Thus, a relation between DEC formation and BET-SA could not be established in the present study. Possible reasons for higher performance of C80Z-citrate and C50Z-citrate solids compared to other Ce/Zr ratios could be related to their different surface composition, crystal structure and acid–base properties. A tetragonal phase was found to be predominant in the solids with Ce content below 50 mol%, whereas the cubic structure was formed for Ce-rich samples (e.g. Ce ≥ 50 mol%). Based on catalytic results, it can be established that the most active phase for DEC formation was cubic Ce<sub>x</sub>Zr<sub>1-x</sub>O<sub>2</sub> (C-citrate, C80Z-citrate, C50Z-citrate). This result is in a good agreement with previous works where pure CeO<sub>2</sub> [99] and mixed oxides such as Ce<sub>0.6</sub>Zr<sub>0.4</sub>O<sub>2</sub> [28] and Ce<sub>0.8</sub>Zr<sub>0.2</sub>O<sub>2</sub> [93] existed in cubic phase were the most active catalysts in direct DEC/DMC batch syntheses. The introduction of Zr into the cubic CeO<sub>2</sub> lattice remarkably affects the amount of oxygen vacancies and the basic properties of the materials therewith [167]. Postole *et al.* [131] claimed that the maximum number of oxygen species, which act as basic sites in the calorimetric experiments, is observed on the surface of Ce<sub>x</sub>Zr<sub>1-x</sub>O<sub>2</sub> sample with high zirconium content. It is due to distortion of CeO<sub>2</sub> lattice by insertion of Zr<sup>4+</sup>, which allowed for easier removal of lattice oxygen. Besides, from XPS results (Table 4.2) a clear enrichment of Zr in the near-surface-region of all samples was found. Interestingly, such enrichment is much more pronounced in case of C80Z-citrate and C50Z-citrate samples. Moreover, the total number of acidic sites in Ce<sub>x</sub>Zr<sub>1-x</sub>O<sub>2</sub> catalysts also depended on Zr content, which consequently led to different catalytic behaviour. Table 4.5 compares acidic properties of Ce<sub>x</sub>Zr<sub>1-x</sub>O<sub>2</sub> catalysts reported by different authors. As in this work, the strength and the total concentration of acidic sites increase upon addition of zirconium. In addition, the high concentration of strong acidic sites 57% and 60% of total acidity was found for Ce<sub>x</sub>Zr<sub>1-x</sub>O<sub>2</sub> samples with x = 0.5 and 0.15, respectively. These results

are in good agreement with the results obtained in this work, since only Ce<sub>x</sub>Zr<sub>1-x</sub>O<sub>2</sub> catalysts with x = 0.5 and 0.2 possess strong acidic sites 15% and 7% of total acidity, respectively.

**Table 4.5.** Comparison of total acidity of catalysts with literature reports.

This work		Postole <i>et al.</i> [131]		de Rivas <i>et al.</i> [167]		Gutiérrez-Ortiz <i>et al.</i> [177]	
Composition	NH <sub>3</sub> μmol m <sup>-2</sup>	Composition	NH <sub>3</sub> μmol m <sup>-2</sup>	Composition	NH <sub>3</sub> μmol m <sup>-2</sup>	Composition	NH <sub>3</sub> μmol m <sup>-2</sup>
CeO <sub>2</sub>	1.3			CeO <sub>2</sub>	1.9	CeO <sub>2</sub>	1.4
Ce <sub>0.8</sub> Zr <sub>0.2</sub> O <sub>2</sub>	2.2	Ce <sub>0.7</sub> Zr <sub>0.3</sub> O <sub>2</sub>	2.0	Ce <sub>0.8</sub> Zr <sub>0.2</sub> O <sub>2</sub>	1.9	Ce <sub>0.8</sub> Zr <sub>0.2</sub> O <sub>2</sub>	1.7
Ce <sub>0.5</sub> Zr <sub>0.5</sub> O <sub>2</sub>	2.1	Ce <sub>0.5</sub> Zr <sub>0.5</sub> O <sub>2</sub>	2.4	Ce <sub>0.5</sub> Zr <sub>0.5</sub> O <sub>2</sub>	2.3	Ce <sub>0.5</sub> Zr <sub>0.5</sub> O <sub>2</sub>	3.5
Ce <sub>0.2</sub> Zr <sub>0.8</sub> O <sub>2</sub>	1.7	Ce <sub>0.3</sub> Zr <sub>0.7</sub> O <sub>2</sub>	2	Ce <sub>0.15</sub> Zr <sub>0.85</sub> O <sub>2</sub>	2.9	Ce <sub>0.15</sub> Zr <sub>0.85</sub> O <sub>2</sub>	4.8
ZrO <sub>2</sub>	2.1			ZrO <sub>2</sub>	4.1	ZrO <sub>2</sub>	6.1

As reported in literature [99, 124], the DEC yield over Ce<sub>x</sub>Zr<sub>1-x</sub>O<sub>2</sub> is reduced to some extent in the presence of strong acid–base sites on the surface of the catalysts. As in the present study, pure ZrO<sub>2</sub> (Z-citrate) and C20Z-citrate possessing stronger strength of acid-base sites in comparison to other Ce<sub>x</sub>Zr<sub>1-x</sub>O<sub>2</sub> catalysts showed rather poor performance. C80Z-citrate catalyst with Ce content of 80 mol% exhibits weak to medium strength of acidic sites seems to be a good balance between the acidity and DEC formation.

According to the results discussed above, the DEC yield was primarily related to the amount of acidic and basic sites on the Ce–Zr–O surface. Both C80Z-citrate and C50Z-citrate have shown nearly an equal amount of acidic and basic sites and the highest catalytic performance as well. These results are in a good agreement with Tomishige *et al.* [87] who claimed that an equal number of neighbouring acidic and basic sites is required for optimal catalyst performance, whereas they found such an effect in the direct synthesis of DMC over ZrO<sub>2</sub> catalysts.

In addition, CO<sub>2</sub> activation needs to be evaluated in a systemic manner, since it is the most difficult part of the reaction. Based on the reaction mechanism proposed by Wada *et al.* [66] for the formation of DMC over Cu–CeO<sub>2</sub> catalyst, the CO<sub>2</sub> adsorption was related to oxidation state of surface cerium (H<sub>2</sub>-TPR results). It was assumed that oxygen vacancies can adsorb CO<sub>2</sub>. The reduction in H<sub>2</sub> and/or by the presence of Cu sites in catalysts lead to the increase the population of O vacancies. In case of Ce<sub>x</sub>Zr<sub>1-x</sub>O<sub>2</sub> solid solutions investigated in the present study, an addition of Zr<sup>4+</sup> into the CeO<sub>2</sub> lattice caused a distortion in the ceria



lattice resulting in an increase in lattice oxygen mobility and also in an increase of the number of anion vacancies on Ce-Zr-O surface [167]. These surface oxygen anions act as basic sites, which were confirmed by CO<sub>2</sub>-TPD analysis (Table 4.4). An improved catalytic performance was achieved on C50Z-citrate and C80Z-citrate solids compared to pure CeO<sub>2</sub> most probably due to significantly increased adsorption of CO<sub>2</sub> on their surface.

Since C80Z-citrate showed the highest Y<sub>DEC</sub> at possibly lowest temperatures and pressures, this solid was used to check its long-term stability. The reaction was performed at 140 °C, 140 bar for 20 hours over C80Z-citrate. It was found that the formation of DEC slightly increased with reaction time and levelled off after 6 hours (Y<sub>DEC</sub> = 0.55%), probably because the active catalytic species forms gradually.

## 4.2. Impact of calcination temperature on catalytic properties of Ce<sub>0.8</sub>Zr<sub>0.2</sub>O<sub>2</sub> solids

Next, the influence of calcination temperature of catalyst precursor compounds on DEC formation was studied. It is a well-known fact that thermal treatment produces significant textural and structural changes. Among various catalysts tested, C80Z-citrate (80 mol% Ce and 20 mol% Zr) sample was found to be active. Therefore, it was further used in subsequent investigations. The catalyst precursor was calcined at three different temperatures (i.e. 450, 700 and 1000 °C) in air for 3 hours and examined under optimized conditions (140 °C and 140 bar). Such results are discussed below in a systematic way.

### 4.2.1. Catalysts characterization

#### ***BET surface area***

Table 4.5 presents the specific BET-SAs, geometrical SAs, pore volumes and average pore sizes of C80Z-citrate samples in dependence on the calcination temperatures applied. The results reveal that an increase in calcination temperature up to 1000 °C caused a significant decrease in the surface area, which was related to changes in pore structure and crystallite size. The calculated geometrical surface areas from  $S_{\text{XRD}} = 6/\rho d$  of Ce<sub>0.8</sub>Zr<sub>0.2</sub>O<sub>2</sub> solids significantly differ from the BET-SA. Dobrosz-Gómez *et al.* [178] explained this fact based on difference in calculations. For  $S_{\text{XRD}}$  calculations, the diffraction peaks of crystallites with initial Ce-Zr solid solution composition were used, while for  $S_{\text{BET}}$  all particles in the sample were taking in account. Moreover, he claimed that solid solution may contain small

agglomerates and grain boundary interfaces which are not available to N<sub>2</sub> gas during the BET analysis. The total pore volumes and the average pores sizes based on the BJH method are also displayed in Table 4.5. An increase in pore size is observed for samples calcined at 700 and 1000 °C. The high temperature treatment leads to the destruction of the small pores and to an increase in the size of the remaining pores. The average pore diameters of all C80Z-citrate catalysts irrespective of calcination temperature are in the mesoporous range.

**Table 4.5.** Effect of calcination temperature on the textural properties of Ce<sub>0.8</sub>Zr<sub>0.2</sub>O<sub>2</sub> catalysts.

Sample	T <sub>c</sub> (°C)	BET-SA <sup>a</sup> (m <sup>2</sup> g <sup>-1</sup> )	XRD-SA <sup>b</sup> (m <sup>2</sup> g <sup>-1</sup> )	Average pore d (nm)	Total pore volume (cm <sup>3</sup> g <sup>-1</sup> )
C80Z-citrate	450	42	143	6.2	0.076
C80Z-citrate	700	37	85	8.9	0.095
C80Z-citrate	1000	11	19	15.7	0.049

<sup>a</sup> Specific BET surface area

<sup>b</sup> Geometrical surface area calculated from S<sub>XRD</sub> = 6/pd.

### X-ray diffraction (XRD)

Figure 4.7a shows the XRD patterns of the C80Z-citrate catalysts. XRD results revealed the formation of single cubic fluorite phase with space group *Fm-3m* in all three cases [179]. No phase segregation was detected. The structural assignment was performed using V-curve (Figure 4.7b). Thus, the lattice volume was related to the respective atomic compositions in the Ce<sub>x</sub>Zr<sub>1-x</sub>O<sub>2</sub> solid solution. C80Z-citrate shows 100% cubic Ce<sub>0.85</sub>Zr<sub>0.15</sub>O<sub>2</sub> phase in all three cases (450, 700 and 1000 °C).

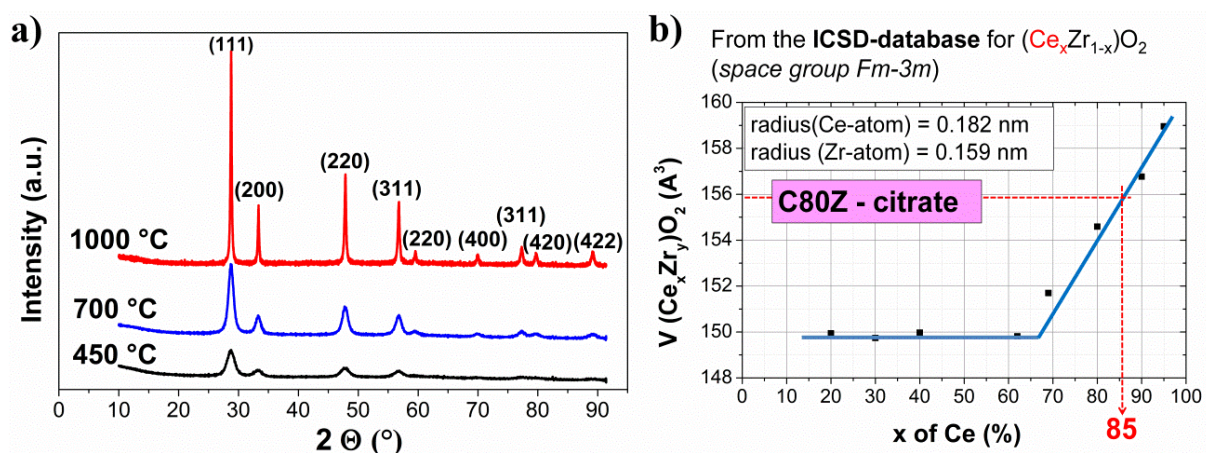


**Figure 4.7.** (a) XRD patterns of C80Z-citrate calcined at 450, 700 and 1000 °C; (b) Volume of the unit cell of the cubic (Ce<sub>x</sub>Zr<sub>1-x</sub>)O<sub>2</sub> as function of the Ce content.

The obtained C80Z-citrate materials are of nanocrystalline nature that is confirmed by the calculation of crystallite size using the Scherrer equation applied to the XRD line broadening [125] (Table 4.6). For the quantitative analysis (Rietveld) the whole diffractogram including the calculated crystallite size in the 2 $\theta$  region from 5-90° was refined. The values are average values for all "visible" reflection peaks of a phase, which appear in the mentioned 2 $\theta$  region and for this calculation the width of peak is required. By the separation of the peaks I would consider anisotropic effects in the size. The diffraction peaks become sharper with increasing calcination temperature from 450 to 700 °C due to crystallite growth (6→10 nm), while at 1000 °C sintering effect is even more pronounced (10 to 45 nm). This observation is in a good agreement with the results from the BET measurements (see Table 4.5).

**Table 4.6.** Effect of calcination temperature on crystallite size, lattice constant, lattice volume and crystallographic density of C80Z-citrate samples.

Sample	T <sub>c</sub> (°C)	Crystal phase	a (nm)	V (nm <sup>3</sup> )	D (nm)	$\rho$ (g cm <sup>-3</sup> )	$\epsilon$ (%)
C80Z-citrate	450	Cubic fluorite	0.538	0.156	6	7.01	0.40
C80Z-citrate	700	Cubic fluorite	0.538	0.156	10	7.02	0.26
C80Z-citrate	1000	Cubic fluorite	0.539	0.156	45	7.00	0.12

The line widths of the Bragg's peaks can vary due to the size of crystallite and crystalline defects originating from microstrain. Thus, both microstrain and crystallite size lead to peak broadening (Equation 2.4). With progressing thermal treatment (700 and 1000 °C) the microstrain decreased due to ordering of the atoms in the crystal lattice and decreasing concentration of defects [180] (Table 4.6). The lattice parameter (a), lattice volume (V) and crystallographic density ( $\rho$ ) are almost not affected by the calcination temperature.

### ***Elemental analysis by Inductively coupled plasma optical emission spectroscopy (ICP-OES) and X-ray photoelectron spectroscopy (XPS)***

XPS and ICP were used to investigate the effect of calcination temperature on the surface and bulk atomic ratios of Ce/Zr in C80Z-citrate solids. The results of the XPS and ICP measurements are presented in Figure 4.8. The surface and bulk atomic Ce/Zr ratios for C80Z-citrate samples calcined at 450 and 700 °C are almost equal to the theoretical atomic ratio of 4.0. However, a decrease in surface Ce to Zr atomic ratio was observed for samples

calcined at 1000 °C due to the migration of Zr from the bulk to the surface during ageing process. Fan *et al.* [181] explained such decline in the Ce/Zr ratio by the reorganization of phases with different Zr composition under high calcination temperature, forming a so-called "shell–core" structure with the high-Zr composition phase in the outer sphere of the particles.

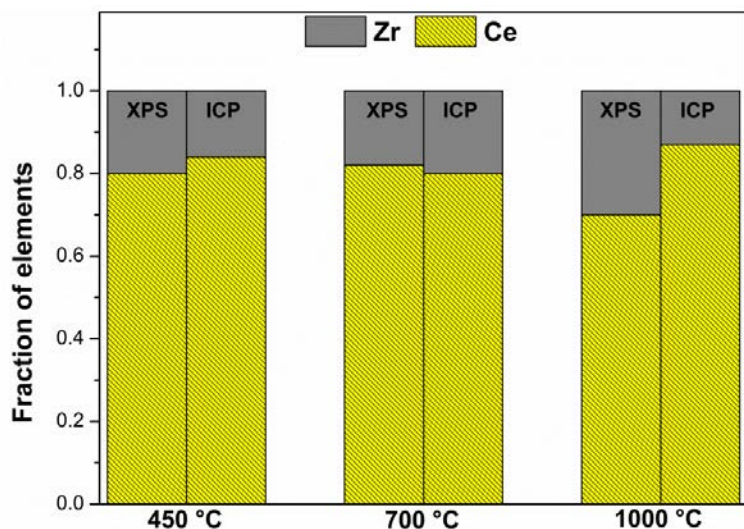


**Figure 4.8.** Comparison of the relative Ce and Zr concentrations in the near-surface-region as measured by XPS with bulk composition (ICP) for C80Z-citrate calcined at 450, 700 and 1000 °C.

### ***Transmission electron microscopy (TEM)***

Figure 4.9 presents TEM images of C80Z-citrate calcined at three different temperatures: 450, 700 and 1000 °C. It can be seen that nanosized particles of C80Z-citrate were obtained under the three calcination temperatures. The particle size of Ce<sub>0.8</sub>Zr<sub>0.2</sub>O<sub>2</sub> calcined at 450 and 700 °C increased from approximately 5 to 10 nm. A more significant increase in the particle size of Ce<sub>0.8</sub>Zr<sub>0.2</sub>O<sub>2</sub> up to 50 nm was observed in samples calcined at 1000 °C. The size of nanoparticle from TEM image is in a good agreement with an average crystallite size calculated from XRD patterns. In addition, via TEM investigation an intergrowth of the single crystallites was detected. In spite of thermal resistivity due to the presence of zirconium in the ceria lattice, the effect was found to be low at 1000 °C. A well separated particle morphology and grain boundary was observed for C80Z-citrate samples calcined at 450 and 700 °C (Figure 4.9a and 4.9b). In a case of C80Z-citrate calcined at 1000 °C, a significant aggregation of crystallites was found (Figure 4.9c).



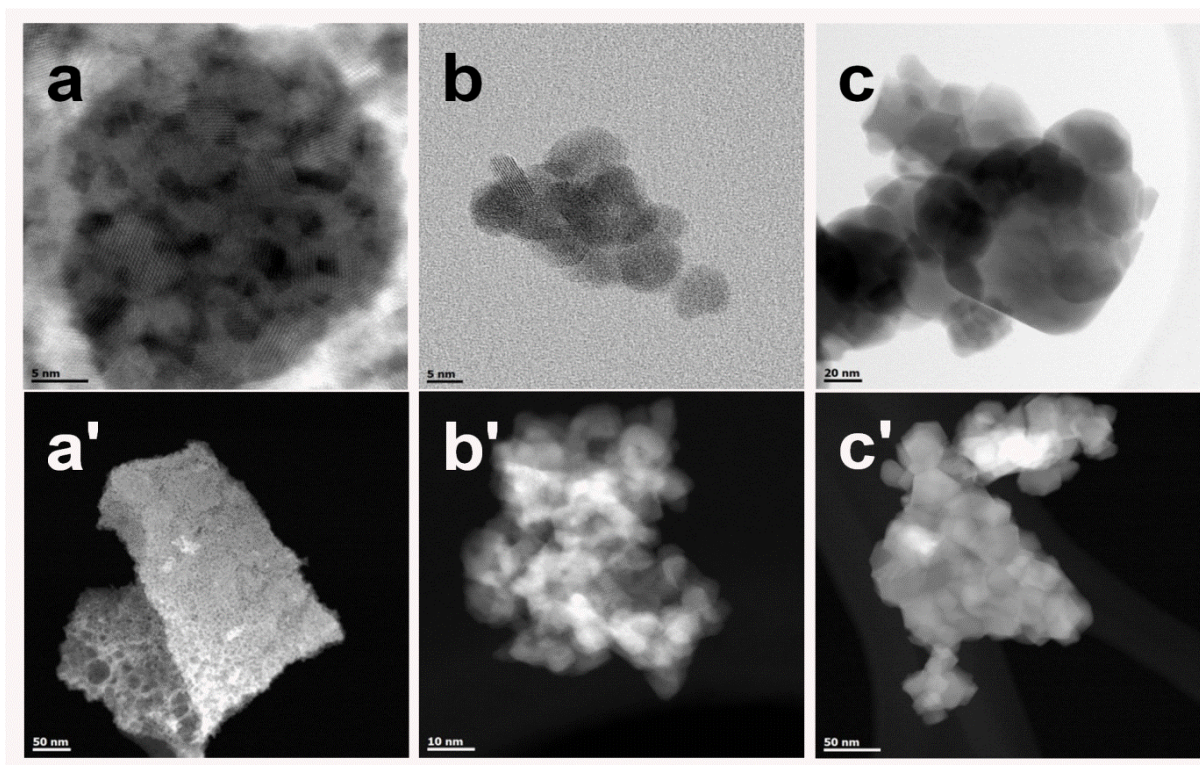


**Figure 4.9.** TEM micrographs of C80Z-citrate solids calcined at different temperatures: (a)-(a') 450 °C; (b)-(b') 700 °C; (c)-(c') 1000 °C.

### *Temperature-programmed reduction (TPR) by H<sub>2</sub>*

Temperature-programmed reduction (TPR) using a feed with 5 vol% H<sub>2</sub> in Ar was applied to study the effect of calcination temperature on the reduction properties of C80Z-citrate catalyst. Figure 4.10 depicts the TPR profiles of the C80Z-citrate catalyst calcined at 450, 700 and 1000 °C.

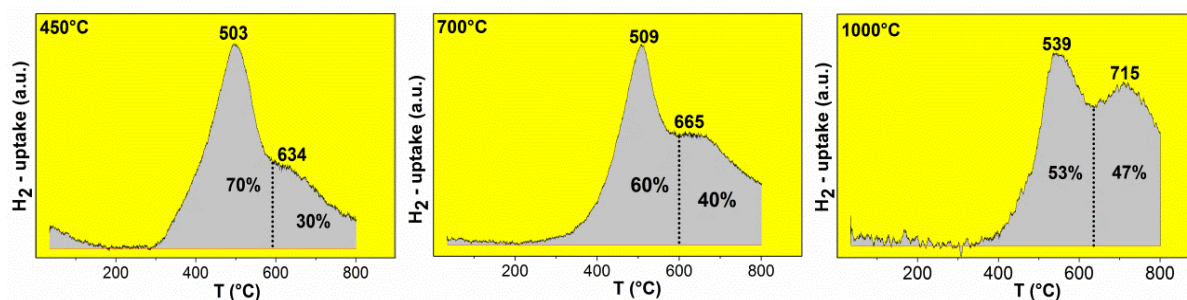


**Figure 4.10.** H<sub>2</sub>-TPR profiles of C80Z-citrate solids calcined at 450, 700 and 1000 °C.

According to the literature low-temperature ( $T \leq 550$  °C) reduction process accounts for reduction of surface oxygen, whereas high-temperature ( $T > 550$  °C) reduction corresponds to the reduction of bulk oxygen [166, 182-186]. Wang *et al.* [133] claimed that the coordinately unsaturated surface lattice oxygen ions can be easily removed in low temperature region

( $T \leq 550$  °C), whereas bulk oxygen requires to be transported to the surface before its removal. Thus bulk reduction takes place at higher temperatures ( $T > 550$  °C). The reduction profile of C80Z-citrate calcined at 450 °C is characterized by two peak at 503 °C (70% of total area) and at higher temperature (634 °C, 30%). Further increase in calcination temperature caused a shift of the reduction peak to higher  $T$ . For C80Z-citrate (700 °C) and C80Z-citrate (1000 °C) samples the reduction process also involves two steps. First region is 350-600 °C with  $T_{\max}$  around 509 (60% of total area of reduction peaks, C80Z-700 °C) and 539 °C (53% of total area, C80Z-1000 °C), second region started at 600 °C with  $T_{\max}$  665 (C80Z-700 °C) and 715 °C (C80Z-1000 °C). Moreover, a good relationship between the BET surface area and H<sub>2</sub> consumption from the first peak was found. It is evident that high surface area of C80Z-citrate calcined at 450 °C (SA: 42 m<sup>2</sup> g<sup>-1</sup>, H<sub>2</sub>-uptake from the first peak: 1.0 mmol g<sup>-1</sup>) sample favours reduction at lower temperature compared to the counterparts sintered at 700 (37 m<sup>2</sup> g<sup>-1</sup>, 0.9 mmol H<sub>2</sub> g<sup>-1</sup>) and 1000 °C (11 m<sup>2</sup> g<sup>-1</sup>, 0.6 mmol H<sub>2</sub> g<sup>-1</sup>). According to the literature, a linear relationship was obtained between the BET surface area and the H<sub>2</sub>-uptake during the low-temperature reduction using experimental data determined by Trovarelli *et al.* [184, 187, 188] and the values predicted by the method of Johnson and Mooi [189]. For the bulk reduction, the temperature of reduction gradually became higher and the area of peaks progressively became relatively larger (30%→40%→47%) with the increase of calcination temperature.

The hydrogen consumption expressed as the amount of H<sub>2</sub> per gram of catalyst is summarized in Table 4.7. A decrease in the amount of H<sub>2</sub> consumed by surface lattice oxygen with an increase in calcination temperature of C80Z-citrate can be related to a temperature-induced decrease in BET-SA as suggested in [190]. Thermal treatments strongly affect redox behaviour of C80Z-citrate solid solution and reduce H<sub>2</sub>-uptake at lower reduction temperatures [182, 191].

**Table 4.7.** H<sub>2</sub> uptake and temperature of maximal hydrogen consumption ( $T_{\max}$ ) during TPR runs for C80Z-citrate catalysts calcined at 450, 700 and 1000 °C.

Sample	$T_c$ (°C)	H <sub>2</sub> uptake (mmol g <sup>-1</sup> )	$T_{\max}$ (°C)
C80Z-citrate	450	1.482	503, 634
C80Z-citrate	700	1.441	509, 665
C80Z-citrate	1000	1.196	539, 715

### Acid-base properties: Temperature-programmed desorption (TPD) of NH<sub>3</sub> or CO<sub>2</sub>

Temperature-programmed desorption (TPD) of ammonia or carbon dioxide was applied for determining the concentration of acidic or basic sites. The temperature, at which desorption occurred, indicates the strength of adsorption, whereas the amount of desorbed probe molecules represent the concentration of acidic or basic sites on the surface of C80Z-citrate. NH<sub>3</sub>-TPD profiles for C80Z-citrate samples calcined at 450, 700 and 1000 °C are shown in Figure 4.11a. Two C80Z-citrate samples (450 and 700 °C) exhibit a broad desorption profile. It reveals the presence of different types of acid sites mostly concentrated in region of moderate acidity. However, a slight shift in desorption temperature towards lower T was found in C80Z-citrate calcined at 700 °C. Such shift of desorption peak was attributed to a decrease in the strength of acidic sites. The solid calcined at 1000 °C has completely lost acidic sites and hence there is absolutely no adsorption of NH<sub>3</sub> over this sample.

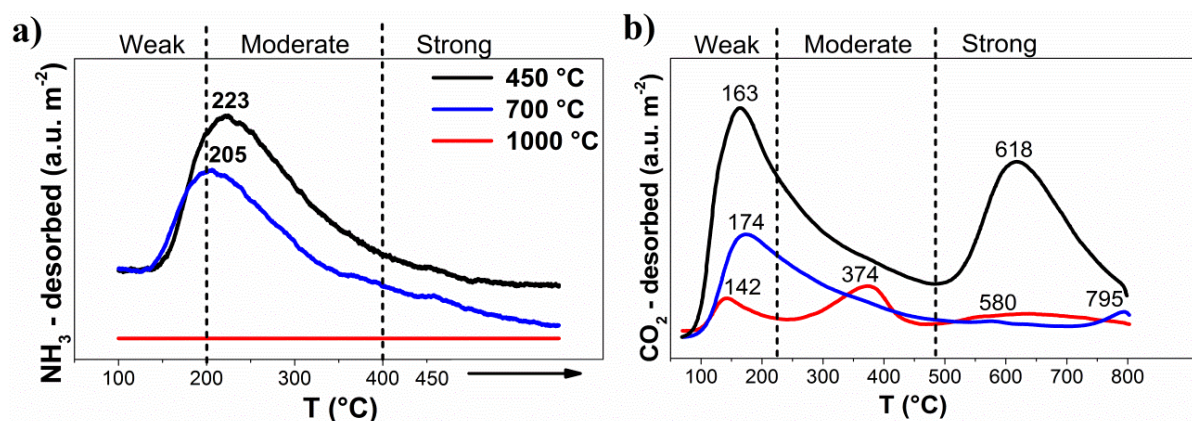


**Figure 4.11.** (a) NH<sub>3</sub>- and (b) CO<sub>2</sub>-TPD profiles of C80Z-citrate samples calcined at 450, 700 and 1000 °C.

Figure 4.11b shows CO<sub>2</sub>-TPD profiles of C80Z-citrate calcined at 450, 700 and 1000 °C. It can be clearly seen that the total amount of CO<sub>2</sub> desorbed from C80Z-citrate 450 °C is very high compared to other two samples. Furthermore, this sample exhibited two large peaks at different temperatures indicating that different types of basic sites are present with weak (100-230 °C), moderate (230-500 °C) and strong (above 500 °C) strength [105, 135]. Compared to C80Z-citrate 450 °C, the intensity of the peak with T<sub>max</sub> at 174 °C for C80Z-citrate 700 °C decreased gradually indicating a drop in the concentration of basic sites. Moreover, C80Z-citrate 700 °C does not possess strong basic sites. As shown in Table 4.7, high calcination temperature provoked crystal growth along with a decrease in the specific surface area. This seemed to be a probable reason for the decline in the concentration of both

acidic and basic sites on the surface of C80Z-citrate 1000 °C. The similar behaviour for Ce<sub>0.33</sub>Zr<sub>0.67</sub>O<sub>2</sub> was described by Tomishige *et al.* [135]. They claimed that both acidity and basicity decreased for material calcined at high temperature (1000 °C). It has been speculated that the surface on Ce-Zr-O catalysts calcined at low temperatures (400 °C) has more roughness and more coordinatively unsaturated cations and anions thereby yielding a higher acidity. Similar effect of calcination temperature on acidic properties of zirconia was also reported by Bolis *et al.* [192] It was assumed that by increasing temperature the elimination of coordinatively unsaturated zirconium ions located at the corners of crystals takes place.

The total concentration of acidic and basic sites on C80Z-citrate samples treated at 450, 700 and 1000 °C has been evaluated and is given in Table 4.8. Compared to C80Z-citrate 450 °C, the peak intensities in TPD profiles of NH<sub>3</sub> and CO<sub>2</sub> for C80Z-citrate 700 °C dropped significantly. This intensity drop was attributed to an overall loss of the total number of acid-base sites with increasing calcination temperatures. The decrease in concentration of acid-base sites, preferentially strong, was in accordance with the surface thermal treatment. Almost no NH<sub>3</sub> and CO<sub>2</sub> were desorbed from C80Z-citrate calcined at 1000 °C indicating negligible number of acidic and basic sites on it.

**Table 4.8.** Acid-base properties of C80Z-citrate catalyst calcined at 450, 700 and 1000 °C. T<sub>max</sub> (NH<sub>3</sub>) and T<sub>max</sub> (CO<sub>2</sub>) stand for temperature of maximal NH<sub>3</sub> and CO<sub>2</sub> desorption, respectively.

Sample	T <sub>c</sub> (°C)	Total acidity (NH <sub>3</sub> -TPD)		Total basicity (CO <sub>2</sub> -TPD)	
		NH <sub>3</sub> -desorbed (μmol g <sup>-1</sup> / μmol m <sup>-2</sup> )	Peak max (°C)	CO <sub>2</sub> -desorbed (μmol g <sup>-1</sup> / μmol m <sup>-2</sup> )	Peak max (°C)
C80Z-citrate	450	94 / 2.2	220	104 / 2.5	163, 618
C80Z-citrate	700	41 / 1.1	205	29 / 0.8	174, 580, 794
C80Z-citrate	1000	0 / 0	-	4 / 0.4	142, 374

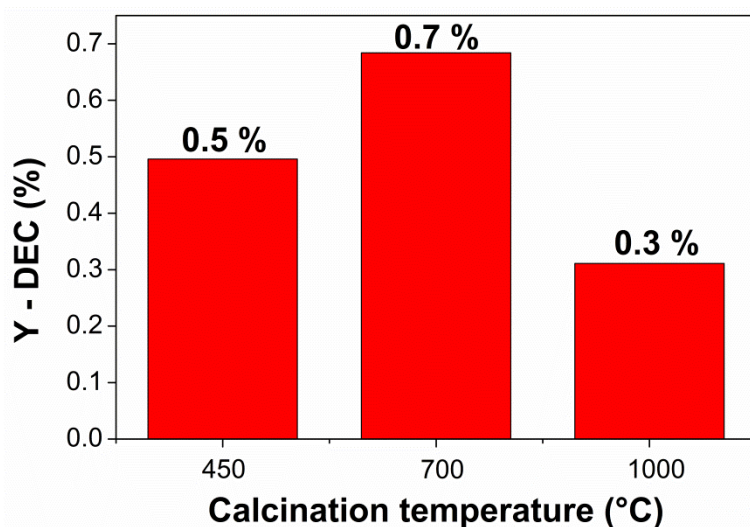
#### 4.2.2. Catalytic results and material properties affecting the activity

Figure 4.12 compares DEC yield obtained over C80Z-citrate catalysts under continuous-flow conditions at 140 bar and 140 °C. The effect of pressure and temperature on the catalytic performance [193, 194] was described in previous paragraph 4.1. The pressure of 140 bar and temperature of 140 °C were selected for further tests, since the highest DEC yield was achieved under these reaction conditions. Tomishige *et al.* [65] applied similar catalysts for the carboxylation of methanol to DMC and claimed that high calcination temperature for



Ce<sub>0.2</sub>Zr<sub>0.8</sub>O<sub>2</sub> catalysts is more favourable for DMC formation even though the BET surface area was considerably reduced after thermal treatment. Consequently, the Ce<sub>0.2</sub>Zr<sub>0.8</sub>O<sub>2</sub> catalyst calcined at 1000 °C despite its much lower surface area exhibited the highest performance in case of Y<sub>DMC</sub> = 0.8%. The authors speculated that the surface structure and properties, especially acidity and basicity, are modified with a high temperature of calcination. Keeping this aspect in mind, I tried to apply the same logic and extended such treatment to my catalysts but for the DEC synthesis. The intention is also to elucidate the correlation between DEC formation and catalyst properties such as BET-SA, crystalline structure, redox properties, adsorption of NH<sub>3</sub> and CO<sub>2</sub> using the present C80Z solid.

Figure 4.12 presents the DEC yield as a function of the calcination temperature of C80Z-citrate catalyst precursor. The yield increased with catalyst calcination temperature only up to 700 °C and then decreased at 1000 °C. Consequently, the DEC formation over C80Z-citrate samples is very dependent on catalyst calcination temperature [195]. However, somewhat different results were obtained compared to the studies of Tomishige *et al.* related to DMC synthesis [65].



**Figure 4.12.** Effect of calcination temperature on the yield of DEC over C80Z-citrate catalysts. Reaction conditions: catalyst weight 1 g, EtOH : CO<sub>2</sub> = 1 : 6, 1 h-on-stream, LHSV = 42 L<sub>liq.</sub> kg<sub>cat.</sub><sup>-1</sup> h<sup>-1</sup>, τ = 68.6 s.

XRD results reveals that C80Z-citrate solids had cubic crystal structure and the phase composition did not change strongly with rising calcination temperature, though crystallite size became larger on the sample calcined at higher temperature. A decrease of BET-SA from 42 m<sup>2</sup> g<sup>-1</sup> (T<sub>c</sub> = 450 °C) to 11 m<sup>2</sup> g<sup>-1</sup> (T<sub>c</sub> = 1000 °C) caused by the high temperature treatment. However, no correlation between BET surface area and DEC formation could be found. The yield of DEC can be related to changes of the strength of acidic and basic sites. C80Z-citrate

calcined at 450 °C possesses higher acidity and basicity than the other two samples. In addition, the presence of strong basic sites in C80Z-citrate calcined at 450 °C has a rather negative effect on the DEC formation. Based on these results, it can be concluded that the active sites of C80Z-citrate solids were the weak and moderate acid-base sites that are present on the surface of the catalysts calcined at 700 °C. In case of C80Z-citrate calcined at 1000 °C, poor performance was observed, which may be attributed to the very low number of acid-base sites. Wang *et al.* [99] observed a similar effect of calcination temperature (400, 600, 800 and 1000 °C) on acid-base behaviour of Ce<sub>0.07</sub>Zr<sub>0.93</sub>O<sub>2</sub> catalysts. Over pure CeO<sub>2</sub> and Ce<sub>0.07</sub>Zr<sub>0.93</sub>O<sub>2</sub> calcined at 800 °C the highest DEC yield (0.16 and 0.11%) was obtained. It was claimed that the Ce-Zr-O solid solutions calcined at lower temperature has more surface roughness while high temperatures lead to more plain surfaces. As a result, more coordinatively unsaturated cations and anions on rough surfaces possess higher number of acidic sites and hence higher DEC yield.

### 4.3. Effect of LHSV and ratio of EtOH : CO<sub>2</sub> on catalytic performance

As seen above, superior catalytic performance could be achieved with C80Z-citrate calcined at 700 °C. In subsequent tests, the effect of different EtOH : CO<sub>2</sub> ratios and different LHSV's on the target reaction was investigated. The results of these studies are illustrated in Figure 4.13a and 4.13b.

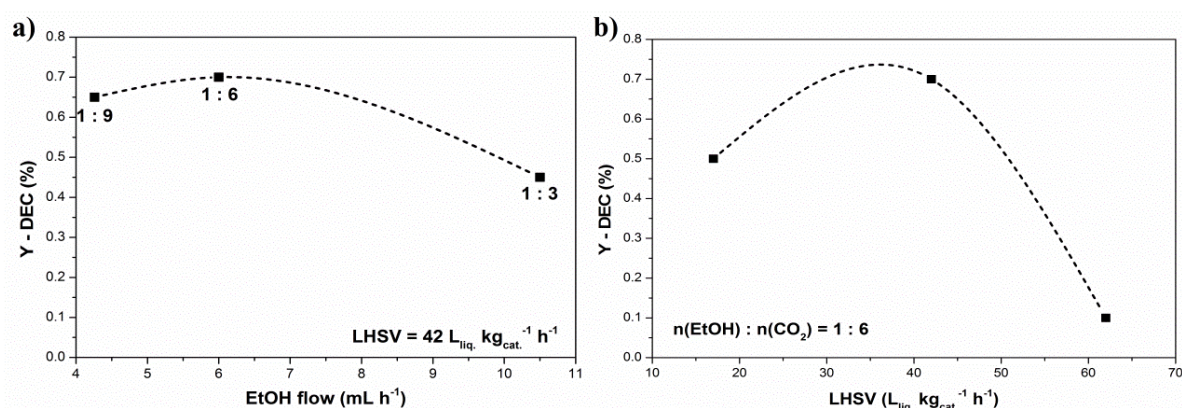


**Figure 4.13.** Effect of (a) EtOH : CO<sub>2</sub> ratios and (b) LHSV's on DEC yield over C80Z-citrate calcined at 700 °C. Reaction conditions: catalyst weight 1 g, 1 h-on-stream, T = 140 °C, p = 140 bar.

The yield of DEC was observed to maintain at around 0.7 % within EtOH : CO<sub>2</sub> ratios ranging from 1 : 9 to 1 : 6 and then decreased considerably with a further increase in the ratio to 1 : 3. As a result, with rise in concentration of ethanol in the feed mixture, the DEC yield

decreased. In this case, an increase in concentration of ethanol requires to apply the higher reaction temperature (up to the critical temperature of pure EtOH,  $T_{cr} = 241\text{ }^{\circ}\text{C}$ ) in order to reach equilibrium DEC yield. On the whole, a EtOH : CO<sub>2</sub> ratio of 1 : 6 was found to be somewhat better. Moreover, up to a LHSV of  $42\text{ L}_{liq}\text{ kg}_{cat}^{-1}\text{ h}^{-1}$  ( $\tau = 68.6\text{ s}$ ) an increase in the DEC yield up to  $Y_{DEC} \sim 0.7\%$  was observed. A further increase in LHSV, e.g.  $62\text{ L}_{liq}\text{ kg}_{cat}^{-1}\text{ h}^{-1}$  ( $\tau = 46.5\text{ s}$ ), caused a drastic drop of the DEC yield ( $Y_{DEC} \sim 0.1\%$ ). The total CO<sub>2</sub>–EtOH flow greatly influences on the contact time. Very low CO<sub>2</sub>–EtOH flow was found to be effective for this continuous reaction mode, since the longer is the contact time, the higher the conversion of EtOH can be achieved.

In order to get better assessment of DEC formation over C80Z-citrate, the predictive Soave–Redlich–Kwong equation was used to calculate the equilibrium DEC yield of  $\sim 0.8\%$  under similar reaction conditions  $T = 120\text{ }^{\circ}\text{C}$  and  $p = 140\text{ bar}$  (see Table 1.4b). In sum, a continuous process for the direct formation of DEC from carbon dioxide and ethanol can be operated at a near equilibrium level.

#### 4.4. Conclusions

Ce<sub>x</sub>Zr<sub>1-x</sub>O<sub>2</sub> catalysts were applied for the direct synthesis of DEC from EtOH and CO<sub>2</sub> under continuous-flow conditions. The Ce : Zr ratio displayed a considerable effect on the catalytic performance. As a result, for Zr-rich catalysts higher reaction temperature regimes is required in comparison with Zr-lean catalysts. Ce<sub>x</sub>Zr<sub>1-x</sub>O<sub>2</sub> solid solutions with  $x \geq 0.5$  showed better catalytic performance than the catalysts with  $x < 0.5$ . Furthermore, the reaction pressure, temperature, EtOH : CO<sub>2</sub> and LHSV are also crucial parameters for improving the catalytic performance.

NH<sub>3</sub>- and CO<sub>2</sub>-TPD results revealed that the concentration of acidic and basic sites was the lowest for pure ceria, but markedly increased upon addition of Zr. The highest amount of desorbed NH<sub>3</sub> was found on pure zirconia due to its acidic nature. H<sub>2</sub>-TPR results showed that the introduction of Zr into the CeO<sub>2</sub> lattice remarkably enhanced the amount of oxygen vacancies due to the formation of Ce<sup>3+</sup> species. These additional adsorption sites lead to a significant increase in  $Y_{DEC}$  by cubic Ce<sub>x</sub>Zr<sub>1-x</sub>O<sub>2</sub> solid solutions instead of pure CeO<sub>2</sub>. The Ce : Zr ratio is helpful to tune the acid–base properties, reducibility, surface vacancies, phase composition of the solids and hence the catalytic properties as well. C80Z-citrate and C50Z-citrate solids with equal concentration of acidic and basic sites (1 : 1) exhibited better DEC yields compared to other catalysts tested.

In addition, the influence of calcination temperature on structural, textural, surface and catalytic properties of Ce<sub>0.8</sub>Zr<sub>0.2</sub>O<sub>2</sub> mixed oxides was studied. The synthesis of DEC from ethanol and CO<sub>2</sub> was studied at 140 °C and 140 bar over Ce<sub>0.8</sub>Zr<sub>0.2</sub>O<sub>2</sub> catalysts calcined at 450, 700 and 1000 °C. XRD results confirmed the presence of cubic fluorite phase in all three cases. C80Z-citrate calcined at 450 °C exhibited the highest concentration of acidic and basic sites, especially strong. High-temperature treatment caused a decrease in the concentration and the strength of acidic and basic sites on C80Z-citrate catalysts. It was supposed that high calcination temperature leads to more plain surfaces and less coordinatively unsaturated cations and anions. C80Z-citrate calcined at 700 °C seems to have good balance between acidity/basicity that probably leads to the observed improved performance. For C80Z-citrate calcined at 1000 °C the acid-base concentration and strengths significantly drops to a very low level. It showed a negative effect on the key catalytic properties for DEC synthesis. A high DEC yield (0.7%) could be achieved with C80Z-citrate calcined at 700 °C. This catalyst was tested at 140 °C and 140 bar at a EtOH : CO<sub>2</sub> ratio of 1 : 6 at a LHSV of 42 L<sub>liq.</sub> kg<sub>cat.</sub><sup>-1</sup> h<sup>-1</sup> (τ = 68.6 s). Hence, it is possible to run the reaction continuously at the near equilibrium level (Y<sub>DEC</sub> = 0.8%) applying suitable contact time.

## Chapter 5

### 5. Effect of second metal in $Ce_{0.8}M_{0.2}O_2$ catalysts on the catalytic activity towards DEC synthesis from ethanol and $CO_2$

Chapter 5 describes the effect of introduction of isovalent  $Hf^{4+}$  and  $Ti^{4+}$  guest cations into host  $CeO_2$  lattice on the DEC formation from ethanol and  $CO_2$  over this novel catalytic system. Pure  $CeO_2$  (C-citrate),  $HfO_2$  (H-citrate),  $TiO_2$  (T-citrate) and Ce-Ti (C80T-citrate), Ce-Hf (C80H-citrate) mixed oxides (80:20 mole ratio based on metal) were prepared by a citrate complexation method, calcined in air at 700 °C for 3 h and characterized by  $N_2$ -adsorption, XRD, ICP-OES, XPS, TEM,  $H_2$ -TPR,  $NH_3$ - &  $CO_2$ -TPD. Catalytic experiments were carried out under continuous-flow conditions in a plug-flow reactor at 140 bar and at 140 °C.

$T = 140\text{ }^{\circ}\text{C}, p = 140\text{ bar}$

$C_2H_5OH + CO_2 \rightleftharpoons [C_2H_5O]_2CO + H_2O$

Catalyst:  $Ce_{0.8}M_{0.2}O_2$  (M = Ti, Hf)

1g,  $T_c = 700\text{ }^{\circ}\text{C}$

III		IV		V	
21 Sc 44.96	22 <b>Ti</b> 47.87	24 V 50.94			
39 Y 88.91	40 Zr 91.22 <b><u>Chapter 3</u></b>	41 Nb 92.91			
57 La 138.905	72 <b>Hf</b> 178.49	73 Ta 180.95			

Cerium oxide ( $CeO_2$ ) based solids are effective catalysts for producing DEC from ethanol and  $CO_2$  due to the presence of both acidic and basic sites. The replacement of cerium ions (0.097 nm) by other smaller cations, such as  $Ti^{4+}$  (0.069 nm),  $Hf^{4+}$  (0.078 nm) or  $Zr^{4+}$  (0.084 nm) is expected to improve those properties compared to pure  $CeO_2$ . In spite of the similarities in structure and stoichiometry of the corresponding metal oxides (metallic ions in the same Group IV), they possess differences in metal-oxygen bond strengths, which depend on their crystalline ionic radii. The Ce-M-O (M = Hf, Ti) is an efficient catalyst for the direct synthesis of DEC from ethanol and  $CO_2$  due to the presence of M-OH hydroxyl groups and coordinately unsaturated  $M^{4+}O^{2-}$  sites that act as Lewis acid-base pairs on its surface. The present chapter describes the effect of introduction of  $Hf^{4+}$  and  $Ti^{4+}$  cations into ceria lattice on the performance of resulted Ce-M-O catalyst for the direct synthesis of DEC from ethanol and  $CO_2$ . The catalytic properties of  $CeO_2$  doped with  $Zr^{4+}$  were already described in details in Chapter 4. The results showed that 20 mol% of Zr doped ceria catalyst yielded DEC at the equilibrium level of  $Y_{DEC} \sim 0.7\%$  at 140 °C and 140 bar at a EtOH :  $CO_2$  ratio of 1 : 6 at a LHSV of 42  $L_{liq} kg_{cat}^{-1} h^{-1}$ . This catalyst has good balance between acidity/basicity that probably leads to the observed improved performance.

## 5.1. Catalyst characterization

### *BET surface areas*

The specific surface area, average pore diameter and total pore volume of  $Ce_{0.8}M_{0.2}O_2$  catalysts and their individual metal oxides are summarized in Table 5.1.

**Table 5.1.** Textural properties and crystallite sizes of pure and mixed Ce-M catalysts.

Sample	BET-SA ( $m^2 g^{-1}$ )	Average pore d (nm)	Total pore V ( $cm^3 g^{-1}$ )	D (nm)
C-citrate	30	3	0.10	26
H-citrate	12	8	0.04	12
C80H-citrate	38	6	0.11	7
T-citrate	15	28	0.14	26
C80T-citrate	29	13	0.08	6

Pure  $HfO_2$  exhibits the lowest surface area ( $12 m^2 g^{-1}$ ) compared to  $CeO_2$  and  $TiO_2$ . Upon incorporating 20 mol% of Hf into  $CeO_2$ , the surface area of the resulting mixed oxides increased to  $38 m^2 g^{-1}$ . A similar effect was also observed by Biswas [196] and Masui [197].

The specific surface area and pore volume of the Ti-containing counterpart were slightly lower than those of bare  $CeO_2$ , i.e. 30 versus 29  $m^2 g^{-1}$  and 0.10 versus 0.08  $cm^3 g^{-1}$ , respectively.

### X-ray diffraction (XRD)

Figure 5.1 shows the XRD patterns of  $Ce_{0.8}M_{0.2}O_2$  mixed oxides. The XRD patterns of pure  $CeO_2$ ,  $HfO_2$  and  $TiO_2$  are also included for comparative purposes. The crystal phases of all these materials were identified through a comparison with the corresponding JCPDS files. The reflection peaks at  $2\Theta = 28.6, 33.19, 47.57, 56.43, 59.23, 69.49$  and  $79.11^\circ$  correspond to the fluorite cubic  $CeO_2$  phase (JCPDS 65-5923).

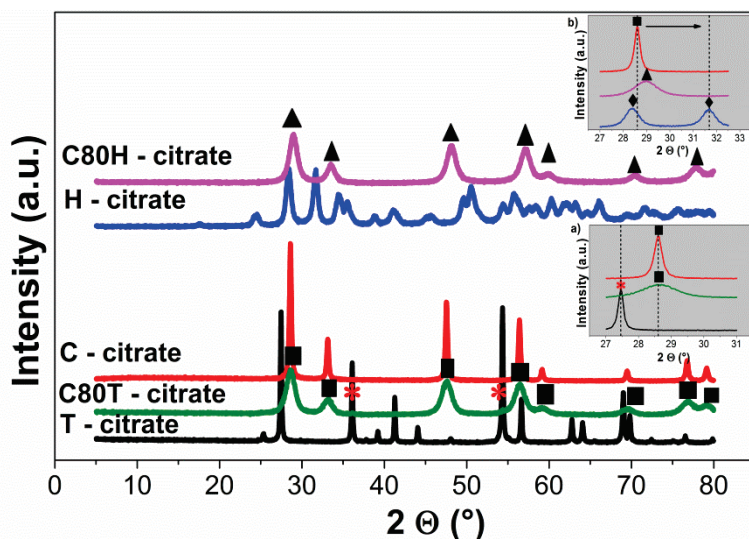


**Figure 5.1.** XRD patterns of  $Ce_{0.8}M_{0.2}O_2$  catalysts ( $M = Hf, Ti$ ). Phase composition:  $\blacktriangle$  c- $Ce_{0.8}Hf_{0.2}O_2$  (ICDD 04-006-1933),  $\blacksquare$  cubic  $CeO_2$  (JCPDS 65-5923). Inset: a) \* tetragonal  $TiO_2$  (rutile, JCPDS 89-4920), b)  $\blacklozenge$  monoclinic  $HfO_2$  (JCPDS 78-49).

In case of pure  $HfO_2$ , the most intensive diffraction peaks at  $2\Theta = 24.43, 28.22, 31.55, 34.45, 35.46$  and  $50.54^\circ$  are characteristic for monoclinic  $HfO_2$  phase. The addition of 20 mol% of Hf into  $CeO_2$  lattice led to a shift of reflection peaks towards higher  $2\Theta$  values compared to pure  $CeO_2$ . The diffraction peaks at  $2\Theta = 29.01, 33.49, 48.07, 57.14, 59.82, 70.39$  and  $77.99^\circ$  represent the cubic  $Ce_{0.8}Hf_{0.2}O_2$  phase (ICDD-04-006-1933). The XRD pattern of pure  $TiO_2$  catalyst consists of the most intensive reflexes at  $2\Theta = 27.48, 36.07, 39.19, 41.22, 54.33, 56.51$  and  $68.98^\circ$  which are representative for the tetragonal (rutile)  $TiO_2$  phase. These findings are in a good agreement with those reported in literature [198] where transformation of anatase to rutile is thermodynamically possible above  $500^\circ C$ . Even in case of mixed oxides, the diffractogram of the C80T-citrate provides typical patterns of cubic



$CeO_2$  and a few less intensive reflexes at  $36.07^\circ$  and  $54.33^\circ$  due to the rutile  $TiO_2$  phase. Thus, phase segregation for  $Ce_{0.8}Ti_{0.2}O_2$  into  $CeO_2$  and  $TiO_2$  was detected, confirming that  $Ti^{4+}$  was not homogeneously incorporated into the  $CeO_2$  lattice.

The crystallite size of pure and mixed oxides calculated using Scherrer equation [125] is summarized in Table 5.1. As was reported earlier, pure  $CeO_2$  exhibited poor thermostability [199] and hence high-temperature treatment ( $700^\circ C$ ) caused a crystallite growth (26 nm). However, the presence of  $Hf^{4+}$  in ceria hinders the crystallite growth resulting in the formation of smaller crystallites (7 nm). XRD pattern of T-citrate confirms high crystallinity of  $TiO_2$  (26 nm). In contrast,  $Ce_{0.8}Ti_{0.2}O_2$ , where the cubic  $CeO_2$  structure predominated along with the tetragonal  $TiO_2$  (rutile) is composed of crystallites of 6 nm. Compared to  $CeO_2$  (26 nm), such decrease in crystallite size is attributed to the presence of the  $TiO_2$  rutile phase in C80T-citrate, which restrained the growth of  $CeO_2$  crystallite. As a conclusion, the incorporation of  $Hf^{4+}$  and  $Ti^{4+}$  into  $CeO_2$  lattice leads to an increase in BET-SA and the formation of smaller crystallite size in comparison to their individual metal oxides.

### ***Elemental analysis determined by Inductively coupled plasma optical emission spectrometry (ICP-OES) and X-ray photoelectron spectroscopy (XPS)***

Selected surface and bulk composition of  $Ce_{0.8}M_{0.2}O_2$  solids is reported in Table 5.2. From ICP analysis it can be seen clearly, that cerium mostly concentrated in the bulk of Ce-M-O solid solutions. Consequently, the XPS studies indicate surface enrichment of promoter metal (Hf, Ti) in all catalysts. Similar results were previously reported by Fang *et al.* [200], where the surface region of  $CeO_2$ - $TiO_2$  with high Ce content  $> 0.7$  is enriched with  $Ti^{4+}$ .

**Table 5.2.** Surface and bulk composition of  $Ce_{0.8}M_{0.2}O_2$  catalysts as determined by XPS and ICP.

Sample	Bulk composition (ICP)			Surface composition (XPS)			EDX
	Ce (mol%)	M (mol%)	Ce/M	Ce (mol%)	M (mol%)	Ce/M	Ce/M
C80H-citrate	75	25	3	56	44	1.3	
C80T-citrate	79	21	3.8	65	35	1.9	1.1, 14.9



### Transmission electron microscopy (TEM)

TEM was applied to investigate the morphology and elemental composition of  $Ce_{0.8}M_{0.2}O_2$  catalysts. Selected micrographs of different Ce-M mixed oxides are shown in Figure 5.2. It is clearly seen that C80H-citrate is composed of nano-sized particles in the range of 8-10 nm, which are distributed uniformly (Figure 5.2(1a)). However, C80T-citrate represents some regions with different shapes and sizes of particles (Figure 5.2(2)). EDX analysis confirmed the presence of Ti-rich region (2c(1)) with very low Ce content as well as Ce-rich region (2c(2)). Using EDX results, it was possible to distinguish Ce- and Ti-rich regions. Ce-rich area exhibits large with well-defined boundaries particles whose size exceeds 10 nm.

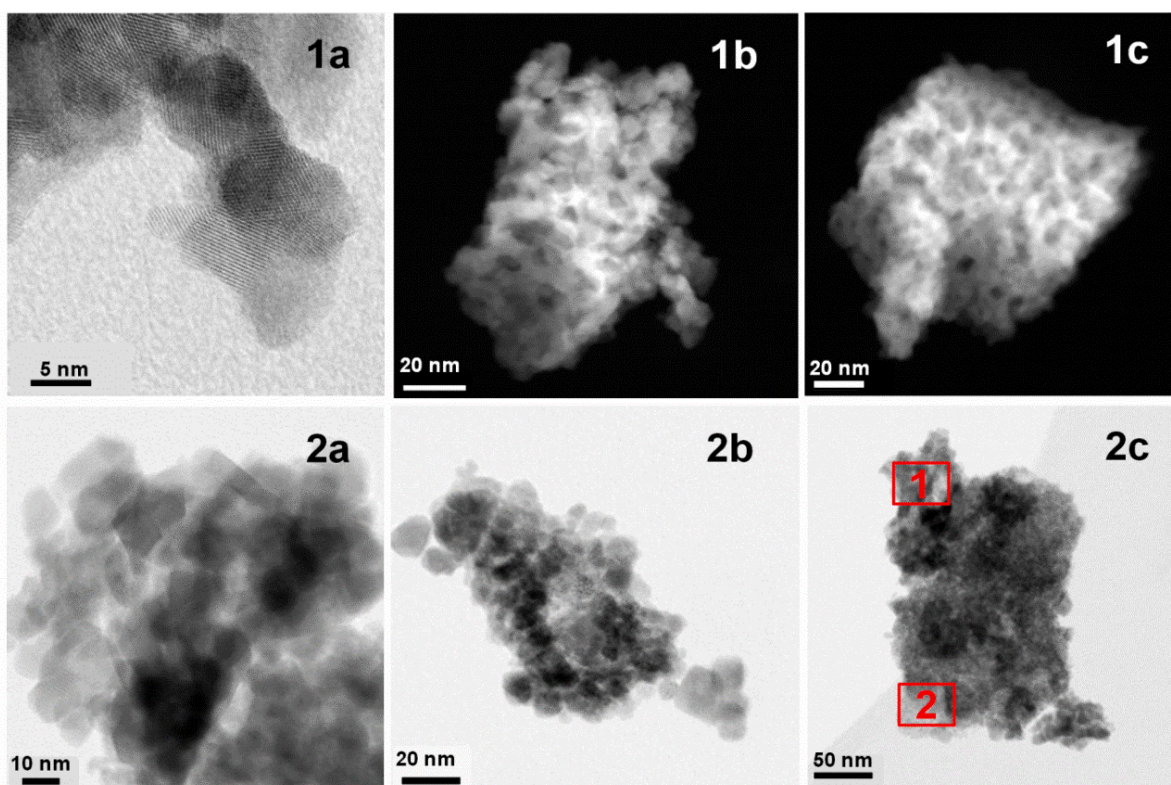


**Figure 5.2.** TEM images of (1a, 1b, 1c) C80H-citrate and (2a, 2b, 2c) C80T-citrate. EDX analysis of the Ce/Ti molar ratio: (2c) area 1 = 1.1, area 2 = 14.9.

### Temperature-programmed reduction (TPR) by $H_2$

Figure 5.3 demonstrates the profiles of  $H_2$  upon temperature-programmed reduction of  $Ce_{0.8}M_{0.2}O_2$  mixed oxides as well as their individual metal oxides. Two peaks of  $H_2$  consumption were identified for pure  $CeO_2$ : the first at low temperature (475 °C) was attributed to the removal of surface lattice oxygen, while the second at 744 °C was assigned to the removal of bulk lattice oxygen [169, 201]. The  $H_2$ -TPR profile for rutile  $TiO_2$  is

characterized by a maximum at 563 °C, whereas the maximal  $H_2$  consumption over  $HfO_2$  was achieved at 758 °C. Thus, among all pure oxides,  $HfO_2$  is the most difficult oxide to be reduced.

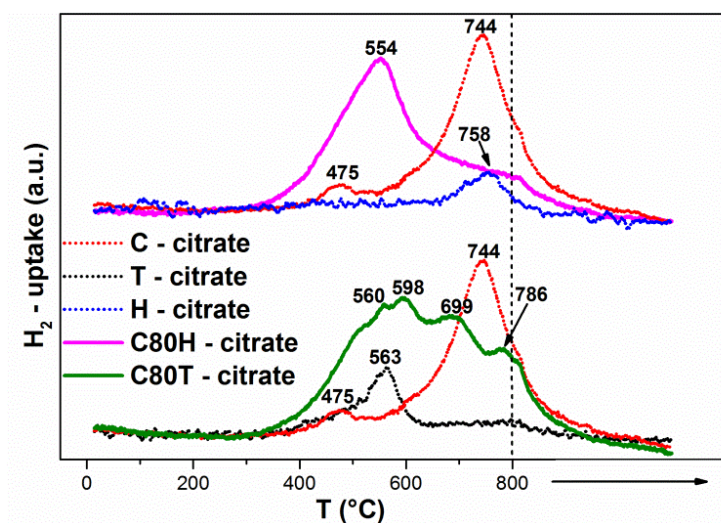


**Figure 5.3.**  $H_2$ -TPR profiles of  $Ce_{0.8}M_{0.2}O_2$  mixed oxides and their parent pure oxides (→: indicates stationary treatment of sample at 800 °C for 2 h).

The incorporation of isovalent almost non-reducible cations such as  $Hf^{4+}$  and  $Ti^{4+}$  into  $CeO_2$  can improve its redox properties. It can be ascribed to the smaller ionic radii of  $Hf^{4+}$  (0.078 nm) and  $Ti^{4+}$  (0.069 nm) in comparison with that of  $Ce^{4+}$  (0.097 nm) that compensated for volume expansion and facilitates the formation of oxygen vacancies. Subsequently, it leads to higher mobility of lattice oxygen inside Ce-M-O solid solution [202]. C80H-citrate demonstrates one reduction peak at  $T_{max}$  554 °C and small shoulder at ~800 °C. In contrast with pure  $CeO_2$ , the position of surface reduction peak moved towards higher temperature in the presence of  $Hf^{4+}$ . Moreover, the  $H_2$ -uptake for C80H-citrate is greatly increased at low temperature indicating high reduction degree of the catalyst. These obtained results are in a good agreement with earlier reports where the reducibility of ceria was enhanced when it was mixed with Hf to form a solid solution [203, 204]. The  $H_2$ -TPR profile of the C80T-citrate catalyst is very broad with several maxima, attributing to the removal of surface and bulk lattice oxygen. C80T-citrate sample shows highest  $H_2$ -uptake (1.928 mmol  $g^{-1}$ ) in a wide temperature range. According to Fang *et al.* [205], among different  $Ce_xTi_{1-x}O_2$  tested,  $Ce_{0.8}Ti_{0.2}O_2$  solid solution exhibited the best reducibility. In addition, the surface enrichment (XPS results) of  $Hf^{4+}$  and  $Ti^{4+}$  in C80H-citrate and C80T-citrate, respectively, is responsible for the high surface reduction degree of corresponding mixed oxides compared to  $CeO_2$ .

**Table 5.3.**  $H_2$  uptake and temperature of maximal hydrogen consumption ( $T_{max}$ ) during TPR runs for  $Ce_{0.8}M_{0.2}O_2$  solids.

Sample	$T_{max}$ (°C)	$H_2$ -uptake ( $mmol\ g^{-1}$ )
CeO <sub>2</sub>	475, 744	1.249
HfO <sub>2</sub>	758	0.064
C80H	554	1.532
TiO <sub>2</sub>	563	0.232
C80T	560, 598, 699, 786	1.928

### ***Acid-base properties: Temperature-programmed desorption (TPD) of $NH_3$ and $CO_2$***

Temperature-programmed desorption (TPD) of  $NH_3$  used as a probe molecule was employed to investigate surface acidity of  $Ce_{0.8}M_{0.2}O_2$  catalysts. The total concentration of acid sites, expressed as the amount of  $NH_3$  desorbed per gram and per square meter of catalyst, is present in Table 5.4.

**Table 5.4.** Acid-base characteristics of  $Ce_{0.8}M_{0.2}O_2$  where M = Hf, Ti.  $T_{max}$  ( $NH_3$ ) and  $T_{max}$  ( $CO_2$ ) stand for temperature of maximal  $NH_3$  and  $CO_2$  desorption, respectively.

Sample	$NH_3$ desorbed ( $\mu mol\ g^{-1} / \mu mol\ m^{-2}$ )	$T_{max}$ ( $NH_3$ ) (°C)	$CO_2$ desorbed ( $\mu mol\ g^{-1} / \mu mol\ m^{-2}$ )	$T_{max}$ ( $CO_2$ ) (°C)
C80H-citrate	60 / 1.6	191	49 / 1.3	158, 607, 785
C80T-citrate	0 / 0	-	9 / 0.3	152, 360, 790

No  $NH_3$  was desorbed from C80T-citrate catalyst, thus indicating the absence of acidic sites able to adsorb ammonia above 100 °C. However, the  $NH_3$ -TPR profile of C80H-citrate is characterized by a broad peak with a maximum at 191 °C (Figure 5.4a) which is in the range of weak to moderate strength of acidity. It was suggested that differences in both acidic and basic sites can be attributed to the various fractions of crystal phases along with the crystallite sizes of catalyst. Temperature-programmed desorption (TPD) of  $CO_2$  is used to evaluate the number and the strength of basic sites on  $Ce_{0.8}M_{0.2}O_2$  surface. The obtained  $CO_2$ -TPD profiles are shown in Figure 5.4b. The profile of the C80H-citrate catalyst consists of a broad peak between 50 and 500 °C with a maximum at 158 °C and additionally of lower intensive peaks at higher temperatures, which are characteristic of strong acidic sites. In case of C80T-citrate,  $CO_2$  desorption takes place in a broad temperature range with maxima at 152, 360 and 790 °C. The obtained results suggest that structural (crystal phase) and textural (specific SA)

changes in  $Ce_{0.8}M_{0.2}O_2$  solids caused by the introduction of either Hf or Ti into  $CeO_2$  can modify surface basicity making it either weaker or stronger in comparison to pure  $CeO_2$ .

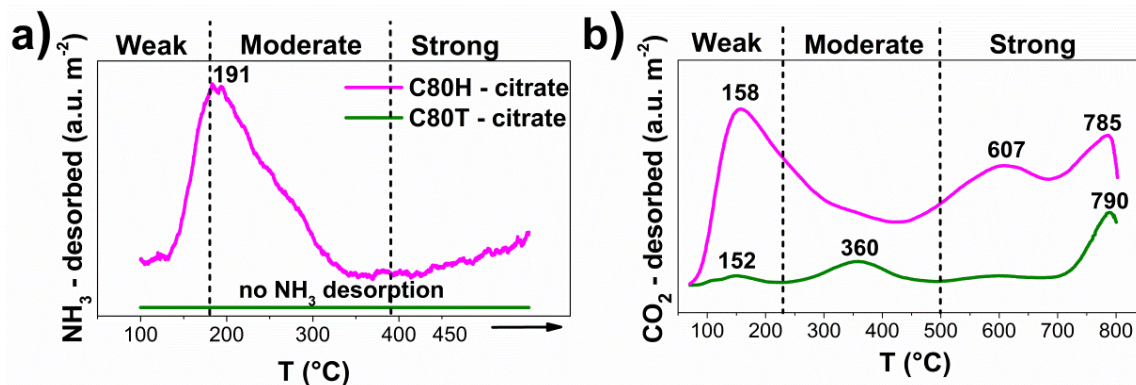


**Figure 5.4.** (a)  $NH_3$ -TPD profiles and (b)  $CO_2$ -TPD profiles of  $Ce_{0.8}M_{0.2}O_2$  catalysts (M = Hf, Ti).

The total amount of  $CO_2$  desorbed from the surface of  $Ce_{0.8}M_{0.2}O_2$  samples in the temperature range of 50-800 °C is shown in Table 5.4. The concentration of  $CO_2$  desorbed from C80H-citrate is  $1.3 \mu\text{mol m}^{-2}$  and from C80T-citrate is  $0.3 \mu\text{mol m}^{-2}$ .

## 5.2. Catalytic results

Figure 5.5 demonstrates the effect of  $Ce^{4+}$  substitution with isovalent cations such as  $Hf^{4+}$  and  $Ti^{4+}$  in  $CeO_2$  lattice on the yield of DEC. In addition, pure oxides were also tested. The DEC yield over pure  $CeO_2$  (C-citrate) is about 0.5%, while over  $HfO_2$  (H-citrate) DEC formation was negligible (the yield of 0.04%). In case of pure  $TiO_2$ , no DEC was formed over pure  $TiO_2$ . In a case of Ce-M-O solid solution, 20 mol% of  $Hf^{4+}$  doped ceria (C80H-citrate) resulted in higher DEC yield than 20 mol% of  $Ti^{4+}$  doped ceria (C80T-citrate). The reason for improved catalytic activity of C80H-citrate catalyst in comparison with C80T-citrate might be rooted from the difference in their textural, structural and acid-base properties, which can affect the interaction between catalyst surface and the adsorbed reactants. BET-SAs of C80H-citrate and C80T-citrate are  $38$  and  $29 \text{ m}^2 \text{ g}^{-1}$ , respectively. However, for carboxylation of ethanol C80T-citrate catalyst was almost not active. Thus, no relationship between specific surface area and DEC formation was found. XRD was performed to correlate the crystalline phase structure and catalytic properties of these solids for carboxylation of ethanol. XRD patterns show the formation of single cubic  $Ce_{0.8}Hf_{0.2}O_2$  phase, whereas the diffractogram of the C80T-citrate sample exhibits typical patterns of cubic  $CeO_2$  and a few less intensive peaks due to rutile  $TiO_2$  phase. Based on XRD results, it was suggested that C80H-citrate possesses



reactive Ce-rich crystal planes. TEM reveals the formation of nanocrystalline mixed solution with particle size of 8-10 nm when  $Hf^{4+}$  is incorporated into ceria lattice. C80T-citrate sample represents both Ce-rich and Ti-rich nanocrystals.

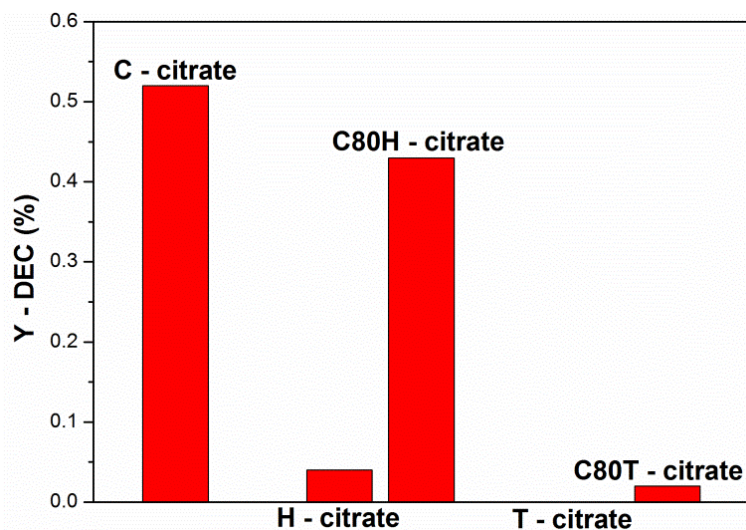


**Figure 5.5.** Effect of second metal in  $CeO_2$  on the catalytic performance towards DEC formation. Reaction conditions: catalyst amount 1g,  $T_c = 700\text{ }^\circ\text{C}$ ,  $EtOH : CO_2 = 1 : 6$ ,  $p = 140\text{ bar}$ ,  $T = 140\text{ }^\circ\text{C}$ , 1 hour-on-stream,  $LHSV = 42\text{ L}_{liq.}^{-1} \cdot kg_{cat}^{-1} \cdot h^{-1}$ ,  $\tau = 68.6\text{ s}$ .

The  $NH_3$ - and  $CO_2$ -TPD results reveal the presence of acid-base sites on C80H-citrate sample. No  $NH_3$  was desorbed from C80T-citrate catalyst, whereas  $CO_2$ -TPD experiments showed only a small amount of  $CO_2$  desorbed from C80T-citrate. However, C80H-citrate sample demonstrates the high amount of desorbed  $CO_2$  in high temperature region. Previous reports [94, 206] have shown that weak to medium acidity is required to produce carbonates such as DEC and DMC over solid catalysts. Combining the  $NH_3$ - and  $CO_2$ -TPD results together, it was noted that C80H-citrate possesses both acidic and basic sites. The simultaneous presence of them on the surface is required for DEC synthesis. Especially, when acidic and basic functions are well balanced in terms of site concentrations, two-points of adsorption of reactants (ethanol and  $CO_2$ ) occur: ethanol interacts with acid  $M^{4+}$  sites (Lewis acid) to form ethoxide groups and basic  $O^{2-}$  sites (Lewis base) is required to activate  $CO_2$ . In a situation where the amount of one kind of active sites is much higher than the other, only the activation of one reactant is dominated, which can in turn lead to reduced performance of the catalysts. Such observation was also reported to be unfavorable in the DEC/DMC formation [207].

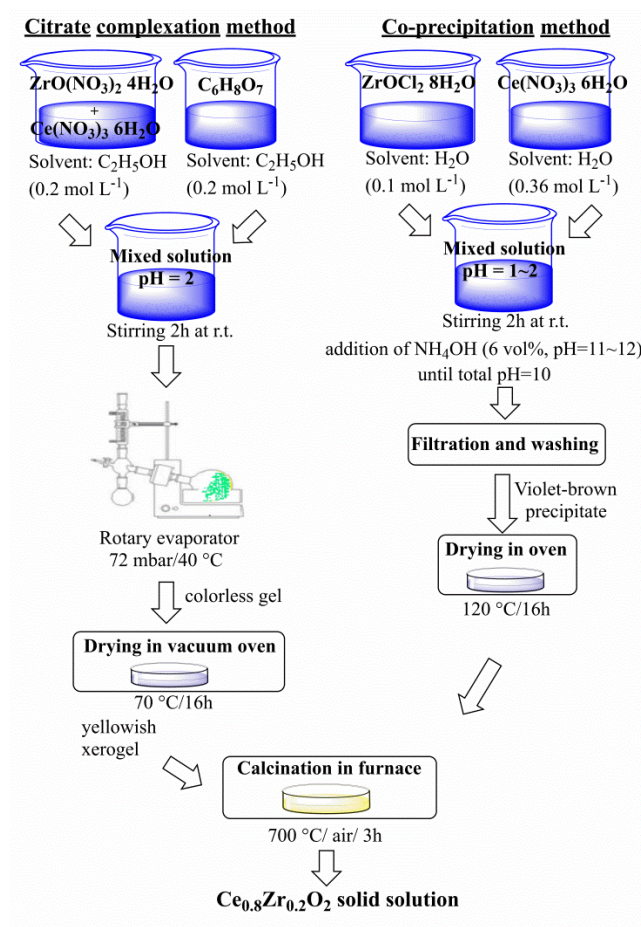
### 5.3. Conclusions

A  $Ce_{0.8}Hf_{0.2}O_2$  solid solution was successfully synthesized by citrate complexation method. The XRD results proved the formation of homogeneous Ce-Hf-O solid material without any phase segregation, while  $Ce_{0.8}Ti_{0.2}O_2$  catalyst was composed of cubic  $CeO_2$  and rutile  $TiO_2$ . Hence  $Hf^{4+}$  cations were fully inserted into  $CeO_2$ . Ce-based samples demonstrated relatively high specific surface areas in the range of  $29\text{--}38\text{ m}^2\text{ g}^{-1}$  and crystallite size in 6-10 nm range. Surface areas were found to depend on the nature of metal incorporated into ceria. Furthermore, the redox properties and acidity characteristics are also considerably affected by the kind of doped metal. The different performance of  $Ce_{0.8}M_{0.2}O_2$  catalyst towards DEC formation was assigned to its varying acid-base properties. C80T-citrate catalyst exhibited poor catalytic performance, which was attributed to the absence of acidic sites on its surface. C80H-citrate with high number of acid-base sites showed the high DEC yield. Such difference in acid-base properties could be related to difference in the geometric arrangement of cations and anions of the various crystallographic planes exposed at the surface of  $CeO_2$ ,  $TiO_2$  and  $Ce_{0.8}Hf_{0.2}O_2$  crystallites. In conclusion, the bimetal catalysts (C80H-citrate and C80T-citrate) exhibited better catalytic performance than individual metals ( $HfO_2$  and  $TiO_2$ ). However compared to pure  $CeO_2$ , C80H-citrate possessed the high concentration of strong basic sites with characteristic desorption temperatures of 680 and 785 °C which is responsible for its lower DEC yield.

## Chapter 6

### 6. Influence of synthesis parameters on catalytic performance of $\text{Ce}_{0.8}\text{Zr}_{0.2}\text{O}_2$ in the production of diethyl carbonate from ethanol and $\text{CO}_2$

Chapter 6 addresses different preparation routes of  $\text{Ce}_{0.8}\text{Zr}_{0.2}\text{O}_2$  solids. Ce-Zr-O catalysts were prepared by two methods: co-precipitation and citrate complexation. The synthesis methods greatly affected textural, structural and acid-base properties of Ce-Zr-O solids. The influence of  $\text{Ce}_{0.8}\text{Zr}_{0.2}\text{O}_2$  physico-chemical properties on catalytic performance in DEC formation from  $\text{CO}_2$  and ethanol is also thoroughly discussed.



Chapter 6 is focused on the influence of different synthesis methods of  $Ce_{0.8}Zr_{0.2}O_2$  on its catalytic performance in synthesis of diethyl carbonate from ethanol and  $CO_2$ . According to the literature [160, 208-213], the physico-chemical properties of Ce-Zr-O material largely depend on preparation methods. Thus, two different methods were applied for preparation of  $Ce_{0.8}Zr_{0.2}O_2$  solid solutions such as co-precipitation [99] and citrate complexation methods [121] using water (already discussed in Chapter 4) and ethanol as solvents. Co-precipitation method using ammonia as precipitating agent is the most common method for the preparation of Ce-Zr solid solution [214, 215]. Applying this synthesis route, mixed metal oxides with relatively high specific surface area are formed [216]. Citrate complexation method is also well-known method for preparation of Ce-Zr mixed oxides. According to this method, highly dispersed and homogeneously distributed solid solutions are formed. Usually for this method a complexing agent is required.

## 6.1. Catalyst characterization

### *BET surface areas*

Selected textural properties such as BET surface area, total pore volume and average pore diameter of differently prepared  $Ce_{0.8}Zr_{0.2}O_2$  materials are summarized in Table 6.1.

**Table 6.1.** Effect of preparation methods on the textural properties of C80Z catalysts.

Sample	Method of preparation	BET-SA ( $m^2 g^{-1}$ )	Total pore V ( $cm^3 g^{-1}$ )	Average pore d (nm)
C80Z-1	Citrate (solvent: $C_2H_5OH$ )	46	0.057	4.2
C80Z-2	Co-precipitation (solvent: $H_2O$ )	51	0.103	7.7

The material prepared by co-precipitation method (C80Z-2) possesses higher surface area and total pore volume than its counterpart prepared by citrate complexation method (C80Z-1) despite the fact that the former material is composed of larger crystallites (15 nm versus 10 nm). It might be due to the use of  $ZrOCl_2 \cdot 8H_2O$  as a Zr precursor and high pH of mixed solution ( $\geq 10$ ) which prevented the collapse of the porous network during drying and calcination (detailed explanation in works of Yoo *et al.* [217] and Hudson *et al.* [218]).



### X-ray diffraction (XRD)

The XRD patterns of two  $Ce_{0.8}Zr_{0.2}O_2$  samples are depicted in Figure 6.1. They are characterized by reflections at  $2\theta$  of 28.69, 33.23, 47.68, 56.49, 59.25, 69.70, 77.01, 79.26 and 88.82°, which correspond to the cubic  $Ce_{0.75}Zr_{0.25}O_2$  (PDF number 00-28-0271) structure with a space group  $Fm-3m$ . No reflexes corresponding to any  $ZrO_2$  structure were found. However, additional reflexes at  $2\theta$  of 30.20 and 50.08° were identified in the XRD pattern of C80Z-2 catalyst and can be ascribed to a Zr-rich phase. On the basis of the database of powder diffraction patterns, this phase is the tetragonal  $Ce_{0.16}Zr_{0.84}O_2$  (Pdf number 00-038-1437) phase with phase group  $P4_2/nmc$ . Nevertheless, the major crystal phase in C80Z-2 is cubic  $Ce_{0.75}Zr_{0.25}O_2$ .

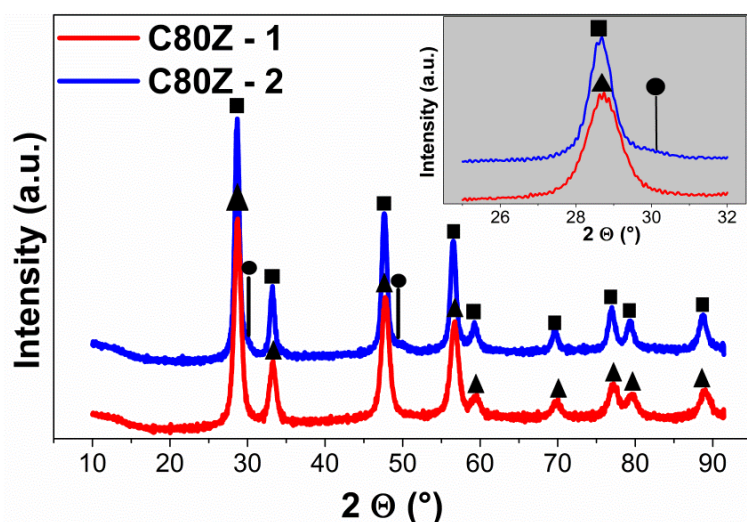


**Figure 6.1.** XRD diffraction patterns of  $Ce_{0.8}Zr_{0.2}O_2$  prepared by citrate complexation (C80Z-1) and co-precipitation (C80Z-2) methods.

The calculated crystal sizes using Scherrer equation [125] are shown in Table 6.2. For sample prepared by citrate method, the crystal size is 10 nm. C80Z-2, where two phases were found, exhibits the  $Ce_{0.75}Zr_{0.25}O_2$  crystal with 15 nm in size and  $Ce_{0.16}Zr_{0.84}O_2$  with 6 nm. It can be noted that the Ce-Zr crystal size changes according to the concentration of Zr, being larger at high Ce content. In addition, the structural assignment was also performed using V-curves (Figure 6.2). Therefore, the lattice volume was related to the respective atomic compositions in the  $Ce_xZr_{1-x}O_2$  solid solution. In case of C80Z-1, the cubic  $Ce_{0.87}Zr_{0.13}O_2$  phase is the only identified phase. It means that Ce and Zr ions were homogeneously distributed in the Ce-Zr powder. C80Z-2 exhibits both Ce-rich  $Ce_{0.89}Zr_{0.11}O_2$  and Zr-rich  $Ce_{0.17}Zr_{0.83}O_2$  phases.

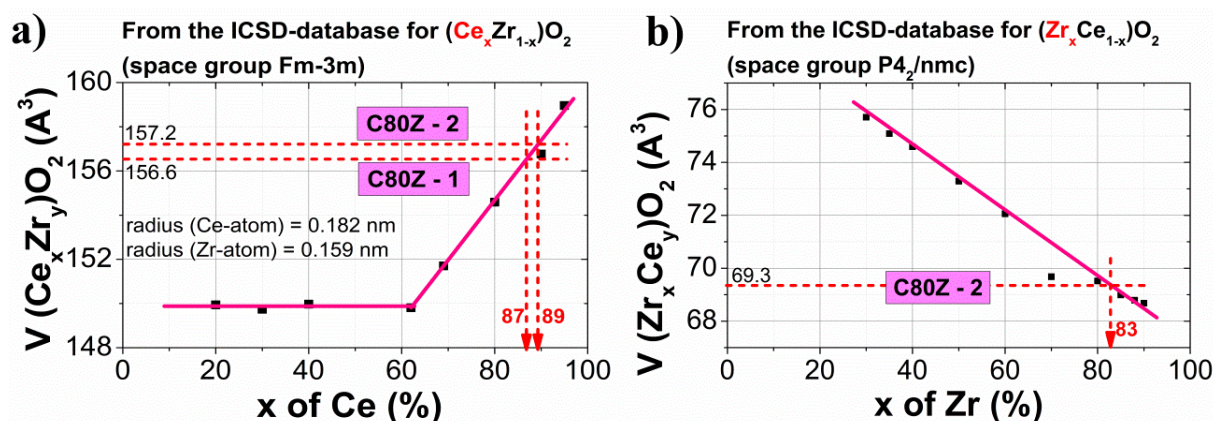


**Figure 6.2.** Volume of the unit cell of the cubic  $(\text{Ce}_x\text{Zr}_{1-x})\text{O}_2$  as function of the (a) Ce content and tetragonal  $(\text{Zr}_x\text{Ce}_{1-x})\text{O}_2$  phase as function of the (b) Zr content.

The phase composition of  $\text{Ce}_x\text{Zr}_{1-x}\text{O}_2$  solids determined by applying V-curves is summarized in Table 6.2. The C80Z-1 sample shows 100% of cubic  $\text{Ce}_{0.87}\text{Zr}_{0.13}\text{O}_2$  phase. In case of C80Z-2, 90% of cubic  $\text{Ce}_{0.89}\text{Zr}_{0.11}\text{O}_2$  and 10% of tetragonal  $\text{Ce}_{0.17}\text{Zr}_{0.83}\text{O}_2$  phases are present. The obtained phase compositions from V-curves are in a good agreement with those defined by the Rietveld method (program package TOZr.PAS 4.2 from Bruker).

**Table 6.2.** Effect of preparation methods on crystallite size and lattice parameters of C80Z samples.

Sample	Crystal phase		a nm	c nm	V nm <sup>3</sup>	$\rho$ g cm <sup>-3</sup>	$\epsilon$ %	D nm
	V-curve	ICSD-database						
C80Z-1	100% c- $\text{Ce}_{0.87}\text{Zr}_{0.13}\text{O}_2$	c- $\text{Ce}_{0.75}\text{Zr}_{0.25}\text{O}_2$ (Pdf number 00-028-0271)	0.539	-	0.157	7.03	0.30	10
C80Z-2	90% c- $\text{Ce}_{0.89}\text{Zr}_{0.11}\text{O}_2$	c- $\text{Ce}_{0.75}\text{Zr}_{0.15}\text{O}_2$ (Pdf number 00-028-0271)	0.539	-	0.157	7.05	0.21	15
	10% t- $\text{Ce}_{0.17}\text{Zr}_{0.83}\text{O}_2$	t- $\text{Ce}_{0.16}\text{Zr}_{0.84}\text{O}_2$ (Pdf number 00-038-1437)	0.363	0.53	0.069	6.42	0.11	6

It can be concluded that the use of co-precipitation route for  $\text{Ce}_{0.8}\text{Zr}_{0.2}\text{O}_2$  synthesis resulted in phase segregation: the major phase is cubic Ce-rich phase with the composition  $\text{Ce}_{0.89}\text{Zr}_{0.11}\text{O}_2$  and the minor phase is tetragonal Zr-rich phase with composition  $\text{Ce}_{0.17}\text{Zr}_{0.83}\text{O}_2$ . These observations prove that homogeneous solid solution is difficult to obtain by co-precipitation method, since Ce and Zr precursors have different rates of precipitation.

### ***Elemental analysis by Inductively coupled plasma optical emission spectrometry (ICP-OES) and X-ray photoelectron spectroscopy (XPS)***

XPS and ICP studies were used to determine the elemental composition in the near-surface-region and in the bulk of  $\text{Ce}_{0.8}\text{Zr}_{0.2}\text{O}_2$  samples, respectively. Table 6.3 compares the surface Ce and Zr atomic concentration with bulk composition. It could be seen that C80Z-2 shows the formation of solid solution with a bulk composition almost equal to nominal. In case of C80Z-1, the Ce-enrichment is observed in the bulk of Ce-Zr-O, which corresponds to composition obtained from V-curve (Figure 6.2a). The surface concentration of Ce species is lower than in the bulk in both cases. On the basis of these results it can be concluded that the bulk and surface compositions of  $\text{Ce}_{0.8}\text{Zr}_{0.2}\text{O}_2$  differ and also depend strongly on preparation method.

**Table 6.3.** Surface and bulk elemental composition of  $\text{Ce}_{0.8}\text{Zr}_{0.2}\text{O}_2$  catalysts measured by XPS and ICP.

Sample	Bulk composition (ICP)			Surface composition (XPS)		
	Ce (mol%)	Zr (mol%)	Ce/Zr	Ce (mol%)	Zr (mol%)	Ce/Zr
C80Z-1	87.7	12.3	7.1	74.7	25.3	3.0
C80Z-2	82.8	17.2	4.8	68.6	31.4	2.2

### ***Transmission electron microscopy (TEM)***

Selected TEM images of two  $\text{Ce}_{0.8}\text{Zr}_{0.2}\text{O}_2$  samples are illustrated in Figure 6.3. C80Z-1 reveals an agglomerated structure, the particles with 10 nm in size are found. C80Z-2 is composed of particles with irregular size and shape (5-15 nm).

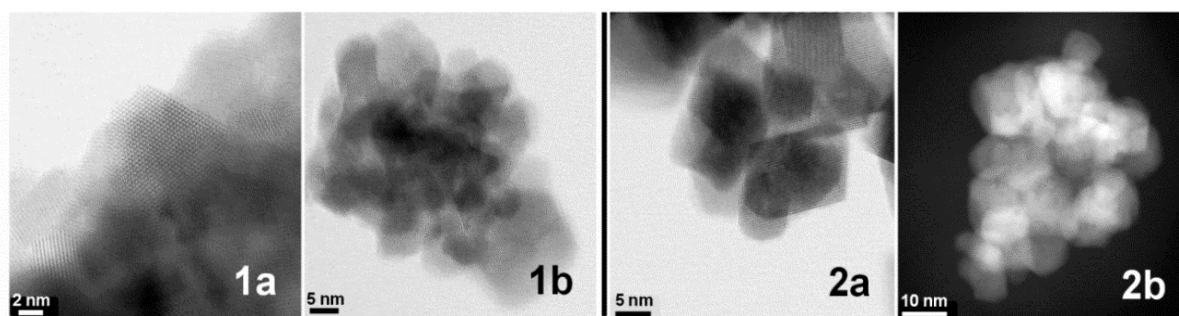


**Figure 6.3.** TEM images of  $\text{Ce}_{0.8}\text{Zr}_{0.2}\text{O}_2$  solid solution synthesized by various methods: C80Z-1 (1a, 1b) and C80Z-2 (2a, 2b).

As evidenced by XRD, such broad distribution in the size is due to the presence of two different crystallite phases, i.e. cubic  $\text{Ce}_{0.89}\text{Zr}_{0.11}\text{O}_2$  and tetragonal  $\text{Ce}_{0.17}\text{Zr}_{0.83}\text{O}_2$  with crystallite

size of 15 and 6 nm, respectively. Based on these observations, it can be concluded that nanosized particles were obtained in samples prepared both by co-precipitation and citrate methods. In summary, the co-precipitation method can be used to produce well crystalline powder, whereas the citrate route - homogeneous material with agglomerated particles.

### ***Temperature-programmed reduction (TPR) by $H_2$***

Redox properties of the two  $Ce_{0.8}Zr_{0.2}O_2$  materials were determined by temperature programmed reduction (TPR) using a feed consisting of 5 vol%  $H_2$  in Ar. Figure 6.4 depicts the obtained TPR profiles.

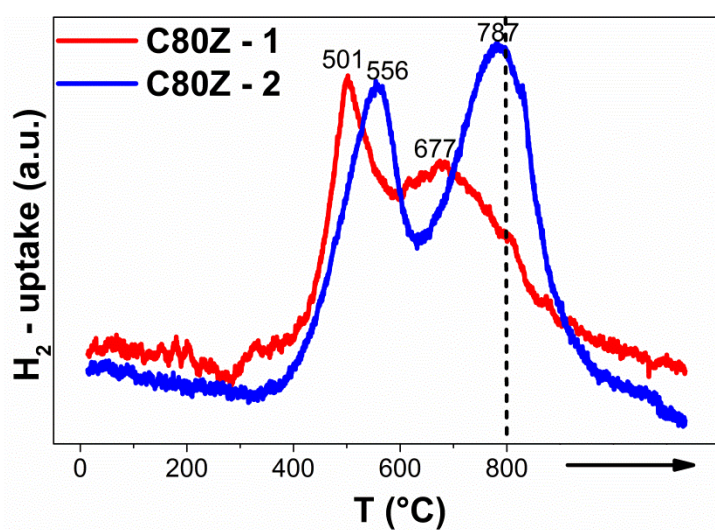


**Figure 6.4.**  $H_2$ -TPR profiles of  $Ce_{0.8}Zr_{0.2}O_2$  catalysts prepared by different methods.

The reduction of C80Z-1 and C80Z-2 samples occurs in two temperature regions. The first peak between 400 and 635 °C is ascribed to the removal of surface lattice oxygen whereas the second peak is associated with removal of bulk lattice oxygen [166]. In general, both the surface and bulk reduction processes occur easier for C80Z-1 than for C80Z-2 as concluded from the temperature of maximal  $H_2$  consumption (Figure 6.4 and Table 6.4).

**Table 6.4.**  $H_2$  uptake and temperature of maximal hydrogen consumption ( $T_{max}$ ) during TPR runs for C80Z solids.

Sample	Peak max (°C)	$H_2$ -uptake (mmol g <sup>-1</sup> )
C80Z-1	501, 677	1.396
C80Z-2	556, 787	1.114



The total  $H_2$  consumption, expressed as mmol of hydrogen per gram of catalyst, and different  $T_{max}$  are summarized in Table 6.4. C80Z-2 synthesized by co-precipitation method shows lower  $H_2$  uptake than C80Z-1 most probably due to the presence of tetragonal Zr-rich phase which is, in general, hardly reduced [166, 219, 220].

### ***Acid-base properties: Temperature-programmed desorption (TPD) of $NH_3$ and $CO_2$***

Temperature-programmed desorption tests using  $NH_3$  as basic molecule were applied for characterization of material acidity. Using this method, it was possible to determine the total number and the strength of acidic sites. The obtained  $NH_3$ -TPD profiles of C80Z-1 and C80Z-2 are given in Figure 6.5a. The observed desorption peaks are in the temperature range of 100-450 °C: the broad peaks at  $T_{max}$  of 205 °C and 190 °C correspond to weak and moderate acid sites, while others at higher temperatures (394 and ~450 °C) are assigned to strong acidity.

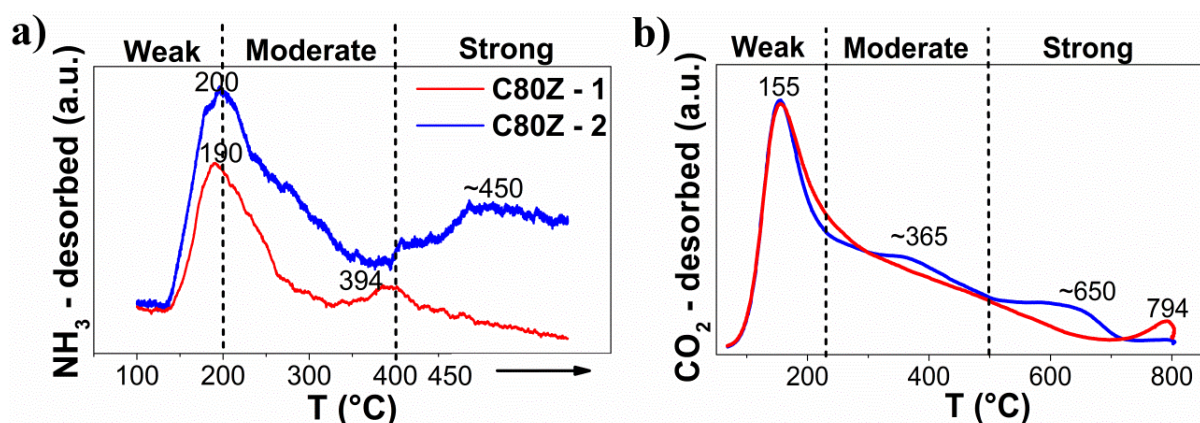


**Figure 6.5.** (a)  $NH_3$ - and (b)  $CO_2$ -TPD profiles of C80Z samples prepared by citrate complexation (C80Z-1) and co-precipitation (C80Z-2) methods.

The total acidity estimated from the peak area under  $NH_3$ -TPD curve and different  $T_{max}$  are summarized in Table 6.5. The C80Z-2 derived by co-precipitation method exhibits much higher concentration of acidic sites ( $1.7 \mu mol NH_3 m^{-2}$ ) than that prepared by citrate complexation method ( $0.54 \mu mol NH_3 m^{-2}$ ). Moreover, the contribution of strong acidity to total acidity is more significant for C80Z-2. It can be explained by the higher concentration of Zr atoms on surface of C80Z-2 than on C80Z-1 (revealed by XPS). It is already known fact, that  $ZrO_2$  is more acidic than  $CeO_2$  [170] and excess of  $Zr^{4+}$  amount on C80Z-2 surface leads to an increase in the surface acidity of resulted solid in contrast to C80Z-1 [177, 217].

**Table 6.5.** Acid-base characteristics of C80Z solids prepared by two different methods.  $T_{max}$  ( $NH_3$ ) and  $T_{max}$  ( $CO_2$ ) stand for temperature of maximal  $NH_3$  and  $CO_2$  desorption, respectively.

Sample	$NH_3$ desorbed ( $\mu mol\ g^{-1} / m^{-2}$ )	$T_{max}$ ( $NH_3$ ) ( $^{\circ}C$ )	$CO_2$ desorbed ( $\mu mol\ g^{-1} / m^{-2}$ )	$T_{max}$ ( $CO_2$ ) ( $^{\circ}C$ )
C80Z-1	25 / 0.54	190, 394	39 / 0.85	155, 794
C80Z-2	80 / 1.7	200, ~450	45 / 0.88	155, ~365, ~650

Additionally, temperature programmed desorption of carbon dioxide ( $CO_2$ -TPD) was used to estimate the basicity of  $Ce_{0.8}Zr_{0.2}O_2$  solids by determining the total number and the strength of surface basic sites (Table 6.5). C80Z-2 ( $0.88\ \mu mol\ CO_2\ m^{-2}$ ) catalyst exhibits somewhat higher concentration of basic sites than C80Z-1 ( $0.85\ \mu mol\ CO_2\ m^{-2}$ ) sample. Figure 6.5b shows the broad  $CO_2$ -TPD profiles (Figure 6.5b) for both C80Z-1 and C80Z-2 catalysts with desorption peaks at  $155\ ^{\circ}C$  and a few shoulders at 365, 650 and  $794\ ^{\circ}C$ . Hence, these solid solutions represent weak, moderate and strong basic sites. However, C80Z-2 catalyst reveals the higher amount of  $CO_2$  desorbed at 650 and  $794\ ^{\circ}C$  corresponded to strong basicity. The difference in basicity and acidity of  $Ce_{0.8}Zr_{0.2}O_2$  prepared by two different methods was ascribed to various specific SA and concentration of  $Zr^{4+}$  on their surface.

## 6.2. Catalytic results and materials properties affecting the catalyst performance

The texture and crystal structure of Ce-Zr mixed oxides were affected by preparation methods. C80Z-1 and C80Z-2 catalysts showed quite similar specific surface areas of 46 and  $51\ m^2\ g^{-1}$ . Since C80Z-1 catalyst with lower specific surface area ( $46\ m^2\ g^{-1}$ ) exhibited higher DEC yield (0.68 mol% vs. 0.6 mol%) than C80Z-2 with higher surface area ( $51\ m^2\ g^{-1}$ ), there is no relationship between BET-SA and DEC yield. The crystal structures of resulted C80Z were greatly depended on synthesis route. Using co-precipitation method, non-homogeneous solid material was formed. XRD results of C80Z-2 revealed the co-existence of two crystal phases: 90% of cubic  $Ce_{0.89}Zr_{0.11}O_2$  and 10% of tetragonal  $Ce_{0.17}Zr_{0.83}O_2$ . C80Z-1 solid solutions using citrate route showed a single cubic Ce-Zr-O phase: 100% cubic  $Ce_{0.87}Zr_{0.13}O_2$ . From  $H_2$ -TPR results, it was evident that the surface oxygen ions were more easily removable in samples prepared by citrate method. From  $NH_3$ - and  $CO_2$ -TPD results, it was found that all samples possess both acidic and basic sites. The highest concentration of strong acid-base

sites with characteristic desorption temperature of about 400 and 500 °C were observed in C80Z-2 solid only.

The effect of acidity/basicity ratio on catalytic performance is shown in Table 6.6. The catalytic results reveal that the higher this ratio, the lower is the DEC yield indicating the negative effect of high concentration of acidic sites, especially strong. However, over C80Z-1 with  $n(NH_3)/n(CO_2) = 0.6$  the formation of DEC slightly increased. The preparation method was an important parameter since it defines the crystalline phase, specific surface area and consequently the redox and acid-base behavior of Ce-Zr mixed oxides.

**Table 6.6.** Correlation of molar ratios  $n_{NH_3}/n_{CO_2}$  with DEC yield. (Reaction conditions: catalyst weight 1g,  $T_c = 700$  °C, EtOH :  $CO_2 = 1 : 6$ ,  $p = 140$  bar,  $T = 140$  °C, 1 hour-on-stream,  $LHSV = 42$  L<sub>liq.</sub><sup>-1</sup>•kg<sub>cat</sub><sup>-1</sup>•h<sup>-1</sup>,  $\tau = 68.6$  s). \*Standard deviation is 0.6%.

Sample	Preparation method	Y-DEC (mol%)*	$n(NH_3) / n(CO_2)$
C80Z-1	citrate complexation	0.68	0.6
C80Z-2	co-precipitation	0.60	1.9

### 6.3. Conclusions

The effective catalyst properties such as crystallite size, porosity, homogeneity, redox and acid-base properties were found to depend on the preparation method of  $Ce_{0.8}Zr_{0.2}O_2$  samples. All the obtained Ce-Zr solid solutions were mesoporous materials confirming by the average pore size in a range of 4-9 nm. Co-precipitation technique applied for the synthesis of C80Z-2 resulted in higher BET-SA in contrast with C80Z-1 prepared by citrate complexation method. Using co-precipitation method, the phase-segregated Ce-Zr samples were obtained, while single c- $Ce_{0.75}Zr_{0.25}O_2$  phase was formed in material prepared by citrate method. It is clearly indicated that Ce and Zr ions were homogeneously distributed in Ce-Zr-O powder. TPD results revealed the presence of high concentration of acidic and basic sites, especially strong, on the surface of C80Z-2. It caused to the lower DEC yield in comparison with C80ZP-1 catalyst. Reduction degree, concentration and strength of acid-base sites were influenced by preparation method and recognized as important parameters in increase of DEC yield over Ce-Zr-O catalyst. Between the two methods applied, the citrate derived  $Ce_{0.8}Zr_{0.2}O_2$  was effective catalyst for DEC synthesis.

# Chapter 7

## 7. Summary and Outlook

*This chapter summarizes the results obtained in the frame of this thesis, provides some conclusions and an outlook for future research on the direct synthesis of organic carbonates, such as DMC and DEC, from alcohols and CO<sub>2</sub>.*

### 7.1. Ce-Zr mixed oxide catalysts and surface modified Ce<sub>0.8</sub>Zr<sub>0.2</sub>O<sub>2</sub> for the direct synthesis of dimethyl carbonate from methanol and CO<sub>2</sub>

The influence of Ce-content in Ce<sub>x</sub>Zr<sub>1-x</sub>O<sub>2</sub> materials and their surface functionalization with phosphoric acid on the DMC yield in liquid phase carboxylation of methanol was investigated. The effectiveness of Ce<sub>x</sub>Zr<sub>1-x</sub>O<sub>2</sub> catalyst for DMC synthesis was ascribed to the co-existence of acid–base sites on its surface. Basic sites are required to activate MeOH and CO<sub>2</sub> and the acidic sites are required to supply methyl groups from MeOH in the last step of the reaction. DMC yield over Ce<sub>x</sub>Zr<sub>1-x</sub>O<sub>2</sub> catalysts was found to depend strongly on cerium content. DMC was not formed over pure ZrO<sub>2</sub> catalyst, while it was significantly enhanced after cerium introduction into ZrO<sub>2</sub>. Thus DMC yield increased from 0.04% over C20Z<sup>prec</sup> to 0.24% over C60Z<sup>prec</sup> and remained the same over C80Z<sup>prec</sup> and C<sup>prec</sup>. Different physico-chemical characterization studies such as N<sub>2</sub> physisorption, XRD, TEM, XPS, NH<sub>3</sub>- and CO<sub>2</sub>-TPD were performed to elucidate the effect of Ce content in Ce<sub>x</sub>Zr<sub>1-x</sub>O<sub>2</sub> solid solution on DMC yield. The crystal structure of Ce<sub>x</sub>Zr<sub>1-x</sub>O<sub>2</sub> with high Ce proportion ( $x \geq 0.6$ ) was cubic with negligible amount of tetragonal phase, whereas Ce<sub>x</sub>Zr<sub>1-x</sub>O<sub>2</sub> high Zr content ( $x < 0.6$ ) showed single phase of the tetragonal structure. Based on CO<sub>2</sub>-TPD results, it was suggested that all Ce<sub>x</sub>Zr<sub>1-x</sub>O<sub>2</sub> contained basic sites of three different strengths: weak, moderate and strong. However, Ce<sub>x</sub>Zr<sub>1-x</sub>O<sub>2</sub> solids with  $x < 0.6$  possessed a high concentration of strong basic sites, confirming that the high content of zirconium greatly enhanced the strength of basic sites. NH<sub>3</sub>-TPD revealed the presence of both weak and medium strength acidic sites on all Ce<sub>x</sub>Zr<sub>1-x</sub>O<sub>2</sub> catalysts. Pure ZrO<sub>2</sub> showing poor catalytic performance had the highest concentration of acidic sites (4.4 μmol m<sup>-2</sup>). It was assumed that C60Z<sup>prec</sup>, C80Z<sup>prec</sup>, C<sup>prec</sup> catalysts having the right balance of the weak and moderate acid/base sites showed high DMC yield.



The surface of  $\text{Ce}_{0.8}\text{Zr}_{0.2}\text{O}_2$  was modified by phosphoric acid in order to promote acid-base properties. Different P-content in  $\text{Ce}_{0.8}\text{Zr}_{0.2}\text{O}_2$  was investigated with the aim to identify efficient catalyst compositions for achieving enhanced DMC yields. In subsequent efforts on the optimization of P/Zr ratios, the yield of DMC enhanced from 0.24 % over  $\text{C80Z}^{\text{prec}}$  to 1.62 % over C80ZP-2 (P/Zr = 0.12). The phosphate treatment has caused remarkable changes in phase composition of  $\text{C80Z}^{\text{prec}}$  leading to Ce-rich cubic and Zr-rich tetragonal  $\text{Ce}_x\text{Zr}_{1-x}\text{O}_2$  phases. Specific surface properties such as surface composition (P/Zr ratios) and acid-base properties were established to be crucial for achieving high DMC yield. The modification by  $\text{H}_3\text{PO}_4$  caused a decrease in the concentration moderate and strong basic sites and an increase in the concentration of Lewis acidic sites from most likely unsaturated surface  $\text{Zr}^{4+}$  cations which are responsible for an enhanced ability to form monodentate methoxy species which further converted to the methyl carbonate species (reaction intermediate for DMC formation) under high  $\text{CO}_2$  pressure. In addition, the introduction of phosphate ions on the surface of calcined  $\text{C80Z}^{\text{prec}}$  ( $\text{C80ZP}^*$ , P/Zr = 0.12) was studied. Such modification caused a decrease of DMC formation ( $Y_{\text{DMC}} = 0.004\%$ ) compared to its addition on uncalcined samples. It was concluded that any thermal treatment, especially double, led to the surface changes, indicating by the drop in BET-SA and by increase in the concentration of strong acidic and basic sites.

## 7.2. Continuous synthesis of diethyl carbonate from $\text{CO}_2$ and ethanol over $\text{Ce}_x\text{Zr}_{1-x}\text{O}_2$ ( $x = 0, 0.2, 0.5, 0.8, 1$ ) catalysts

Different catalyst composition and reaction variables, e.g. reaction temperature, molar ratio of reactants, reaction pressure, reaction time, LHSV, were evaluated for the continuous synthesis of diethyl carbonate from  $\text{CO}_2$  and EtOH. With the knowledge of suitable reaction conditions and catalyst active species, it was possible to reach maximum possible amount of DEC, i.e. at the equilibrium level. Since this route shows high thermodynamic limitations, the acid-base catalyst is required to activate  $\text{CO}_2$  and EtOH.  $\text{Ce}_x\text{Zr}_{1-x}\text{O}_2$  catalyst was applied for DEC synthesis due to its unique acid-base bifunctional properties.  $\text{Ce}_x\text{Zr}_{1-x}\text{O}_2$  solids were prepared by citrate complexation method and calcined at  $450\text{ }^\circ\text{C}/3\text{h}/\text{air}$ . Catalytic performance of the catalysts was evaluated towards the synthesis of DEC from ethanol and  $\text{CO}_2$  in a broad range of pressures (80-180 bar) and temperatures (80-180  $^\circ\text{C}$ ). The Ce proportion has shown a considerable influence on DEC formation. The results revealed that the SSA, crystal structure, redox properties as well as acid-base characteristics of the solids are strongly influenced by the content of Ce in the catalysts, which in turn showed a clear impact on the catalytic

performance. C80Z-citrate solid, exhibited a single  $\text{Ce}_{0.75}\text{Zr}_{0.25}\text{O}_2$  phase of cubic structure and right concentration of acidic and basic sites (2.2 : 2.5) of weak and moderate strength, showed the best catalytic performance compared to all other Ce-Zr mixed catalysts.

Next, the effect of reaction temperature and pressure on DEC formation was investigated over C-citrate, C80Z-citrate, C50Z-citrate, C20Z-citrate and Z-citrate catalysts in continuous running plug flow reactor. An increase of DEC yield was observed with pressure rise upto 140-160 bar depending Ce-Zr-O composition, beyond which it showed some adverse effect on the yield of DEC. Temperature also revealed positive effect on DEC yield, which increased from 0.06 to 0.5% with rise of temperature from 80 to 140 °C. But a further increase in temperature to 180 °C again caused a decrease in the DEC formation due to thermodynamic reasons. The highest yield of DEC obtained over C80Z-citrate was 0.52% at 140 °C and at 140 bar. This obtained DEC yield was still lower than thermodynamically possible  $Y_{\text{DEC}}$  of 0.8% at similar reaction conditions.

In order to explore catalyst on-stream stability, the DEC reaction was performed at 140 °C, 140 bar for 20 hours over the C80Z-citrate catalyst. The experimental results revealed that the formation of DEC slightly increased with reaction time and levelled off after 6 hours ( $Y_{\text{DEC}} = 0.55\%$ ). This result indicates that equilibrium was not established for the formation of DEC from ethanol and  $\text{CO}_2$ .

In subsequent runs, the influence of the calcination temperature on the phase composition and other properties of the best catalyst (C80Z-citrate) were studied. These characterizations were explored to check its impact on DEC formation. The C80Z-citrate catalyst precursors were calcined at three different temperatures (i.e. 450, 700 and 1000 °C) in air for 3 hours and tested at temperature of 140 °C and pressure of 140 bar. The structural and surface changes were related to alterations of the Ce-Zr-O crystallite size, reducibility, and/or acid-base properties. The increase in the crystallite size of  $\text{Ce}_{0.75}\text{Zr}_{0.25}\text{O}_2$  leading to decrease of BET-SA and concentration of acid-base sites was observed with increasing the calcination temperature. Among the three calcination temperatures, the sample calcined at 700 °C further improved the yield of DEC to 0.7%. On the whole, C80Z-citrate calcined at 700 °C exhibited a good balance between acidity/basicity (1.1 : 0.8) and crystallite size (10 nm) variation that led to the observed improved performance.

Since this chapter has focused on continuous process for the synthesis of DEC from  $\text{CO}_2$  and ethanol, the total flow rate of reagents was very important parameter to achieve a high DEC yield. Therefore, the effect of LHSV on catalytic performance was investigated.

C80Z-citrate catalyst calcined at 700 °C was tested at constant temperature (140 °C) and pressure (140 bar) but different total flow rates: 17, 42 and 62 L<sub>liq</sub>·kg<sub>cat</sub><sup>-1</sup>·h<sup>-1</sup>. It was found that an increase of CO<sub>2</sub>-EtOH flow rate up to 42 L<sub>liq</sub>·kg<sub>cat</sub><sup>-1</sup>·h<sup>-1</sup> favored the DEC formation. However, further increase of total flow rate caused to dramatic drop of Y<sub>DEC</sub>. Based on this finding, a flow rate of 42 L<sub>liq</sub>·kg<sub>cat</sub><sup>-1</sup>·h<sup>-1</sup> was selected for the further catalytic tests because it enables maximum space-time-yield.

### 7.3. Effect of second metal in Ce<sub>0.8</sub>M<sub>0.2</sub>O<sub>2</sub> catalysts on the catalytic activity towards DEC synthesis from ethanol and CO<sub>2</sub>

The effect of introduction of isovalent M<sup>4+</sup> (where M<sup>4+</sup> is either Hf<sup>4+</sup> or Ti<sup>4+</sup>) guest cations into host ceria lattice (Metal : Ce molar ratio of 20 : 80) and its influence on DEC yield was investigated. The ceria doped with M<sup>4+</sup> resulted in different crystallite size, redox and acid-base properties compared to pure CeO<sub>2</sub>, since the substitution of Ce<sup>4+</sup> (ionic radius 0.097 nm) with smaller M<sup>4+</sup> (Hf<sup>4+</sup> or Ti<sup>4+</sup> with ionic radii of 0.078 and 0.069 nm, respectively) led to the structural modifications of the fluorite-type lattice of ceria. XRD pattern of C80H-citrate showed the formation of cubic Ce<sub>0.8</sub>Hf<sub>0.2</sub>O<sub>2</sub> phase, whereas C80T-citrate sample provided typical patterns of cubic CeO<sub>2</sub> with a few less intensive peaks due to rutile phase, indicating a limited solubility of Ti<sup>4+</sup> in the ceria matrix. C80H-citrate and C80T-citrate exhibited the better redox properties than their parent metal oxides. C80H-citrate contained the higher concentration of weak and moderate acid sites than pure CeO<sub>2</sub>. However, the number of basic sites did not change considerably after doping of Hf<sup>4+</sup>. No NH<sub>3</sub> was desorbed from C80T-citrate, indicating the absence of acid sites. It was suggested that various crystal structure of Ce<sub>0.8</sub>M<sub>0.2</sub>O<sub>2</sub> affected the properties of both surface M<sup>4+</sup> and O<sup>2-</sup> ions forming acid-base pairs. On the whole, the 20 mol% of Hf doped ceria (i.e. C80H-citrate) catalyst gave the higher DEC yield (0.45%) compared to C80T-citrate catalyst (0.02%).

### 7.4. Influence of synthesis methods on catalytic performance of Ce<sub>0.8</sub>Zr<sub>0.2</sub>O<sub>2</sub> in the production of diethyl carbonate from ethanol and CO<sub>2</sub>

Finally, with aim to improve the efficient catalyst properties for DEC synthesis, two different methods were applied for preparation of Ce<sub>0.8</sub>Zr<sub>0.2</sub>O<sub>2</sub> solid solutions such as co-precipitation and citrate complexation methods. Citrate complexation method provided a homogeneous nanocrystalline Ce<sub>0.8</sub>Zr<sub>0.2</sub>O<sub>2</sub> solid solution, whereas co-precipitation method resulted in

relatively high specific surface area  $\text{Ce}_{0.8}\text{Zr}_{0.2}\text{O}_2$ . From  $\text{NH}_3$ -TPD experiments was found that C80Z-2 prepared by co-precipitation method had much higher concentration of acid sites, especially strong, compared to C80Z-1 prepared by citrate method. The distribution of basic sites on C80Z-1 and C80Z-2 surfaces was almost the same. However, C80Z-2 demonstrated more basic character than C80Z-1 that led to its lower catalytic activity compared to C80Z-2. As a conclusion, the catalysts prepared by different methods possess different crystal phase and surface properties that affected the catalyst performance.

## 7.5. Outlook

This work presents the preparation, thorough characterization and evaluation of Ce-based catalysts for the direct synthesis of dialkyl carbonates from  $\text{CO}_2$  and  $\text{C}_1$ - $\text{C}_2$  alcohols (methanol and ethanol). Since a possible high yield (close to equilibrium yield) of dialkyl carbonate was achieved in the present study, future works should continue tests in a continuous-flow reactor under reaction conditions of  $p = 140$  bar,  $T = 140$  °C,  $\text{R-OH} : \text{CO}_2 = 1 : 6$  over Ce-Zr-O catalysts.

Despite the high yields of DMC and DEC over  $\text{CeO}_2$ - $\text{ZrO}_2$  and  $\text{CeO}_2$ - $\text{ZrO}_2/\text{H}_3\text{PO}_4$  described in this work, the amount of DMC/DEC produced remains very low. This is due to the thermodynamic limitations. Therefore, the most powerful method to shift the reaction equilibrium towards the product side is the use of dehydrating agent to remove water. Inorganic agents, such as zeolites or  $\text{MgSO}_4$ , can be used for this purpose. However, under high reaction temperature (140-180 °C) it is difficult to adsorb water from the reaction mixture. It can be successfully done, using external loop with a fixed bed column (at room temperature) filled with zeolite 3A and circulating the reaction mixture through this loop. After the required time, the system should be depressurized and then the reaction products can be analyzed. Another, more attractive technology for water removal is membrane catalytic reactor. However, under reaction conditions applied in the present work it will be difficult to remove water from the reaction mixture. In most cases, high reaction pressure will cause swelling of the membrane. The introduction of reactive dehydration agents, such as  $\text{CH}_3\text{I}$ , trimethyl phosphate, butylene oxide, acetal and *ortho* ester into reaction media can also increase the amount of the desired products. The big advantage of these dehydration systems is their ability to work at high reaction temperature ( $> 100$  °C) that was not possible with inorganic absorbents. However, they have many disadvantages: i) toxic and corrosive reactants; ii) formation of by-products that cause difficulties in separation from DMC/DEC;

iii) side reaction and deactivation of catalyst. To overcome these drawbacks, the use of catalytic hydration system becomes very attractive method to remove the water from the reaction media. This means that dehydration reagents are hydrated by catalysts. In conclusion, the combination of Ce-Zr-O catalyst (acid-base properties) with catalytic dehydration system will increase the yield and selectivity of organic carbonates.

## 8. References

- [1] M. Aresta, A. Dibenedetto, I. Tommasi, *Energy & Fuels* 15 (2001) 269.
- [2] M. Aresta, M. Galatola, *J. Clean. Prod.* 7 (1999) 181.
- [3] P. Freund, S. Bachu, D. Simbeck, K. Thambimuthu, M. Gupta, Properties of CO<sub>2</sub> and carbon-based fuels, IPCC special report on CO<sub>2</sub> capture and storage, 2013, pp. 383.
- [4] P.J. Cormier, R.M. Clarke, R.M.L. McFadden, K. Ghandi, *J. Am. Chem. Soc.* 136 (2014) 2200.
- [5] I.P.O.C. Change, Properties of CO<sub>2</sub> and carbon-based fuels, IPCC Special Report on CO<sub>2</sub> Capture and Storage, 2005, pp. 381.
- [6] P. Forster, V. Ramaswamy, P. Artaxo, T. Berntsen, R. Betts, D.W. Fahey, J. Haywood, J. Lean, D.C. Lowe, G. Myhre, J. Nganga, R. Prinn, G. Raga, M. Schulz, R.V. Dorland, Contribution of working group I to the fourth assessment report of the intergovernmental panel on climate change, Cambridge University Press, NY, USA, 2007, pp. 131.
- [7] J. Olivier, Emission Database for Global Atmospheric Research (Version 3.2), Netherlands
- [8] R.A. Rohde, Greenhouse Gas by Sector, 2006.
- [9] G.P. Peters, R.M. Andrew, T. Boden, J.G. Canadell, P. Ciais, C. Le Quere, G. Marland, M.R. Raupach, C. Wilson, *Nature Clim. Change* 3 (2013) 4.
- [10] F.e. al., Global Carbon Project 2014, CDIAC, 2014.
- [11] J.G.J. Olivier, G. Janssens-Maenhout, M. Muntean, J.A.H.W. Peters, Trends in global CO<sub>2</sub> emissions: 2013 Report, PBL Netherlands Environmental Assessment Agency, 2013.
- [12] P. Markewitz, W. Kuckshinrichs, W. Leitner, J. Linssen, P. Zapp, R. Bongartz, A. Schreiber, T.E. Muller, *Energy & Environmental Science* 5 (2012) 7281.
- [13] C. Song, *Catal. Today* 115 (2006) 2.
- [14] N. Sridhar, D. Hill, CO<sub>2</sub> utilization: electrochemical conversion of CO<sub>2</sub>-opportunities and challenges, 2011.
- [15] E. Gobina, CO<sub>2</sub> utilization and recovery, Business Communications Company, Norwalk, 2004.
- [16] I. Ganesh, *Renew. Sust. Energ. Rev.* 31 (2014) 221.
- [17] S.G. Jadhav, P.D. Vaidya, B.M. Bhanage, J.B. Joshi, *Chem. Eng. Res. Des.* 92 (2014) 2557.
- [18] B. Loges, A. Boddien, F. Gärtner, H. Junge, M. Beller, *Top. Catal.* 53 (2010) 902.
- [19] J.E. Whitlow, C.F. Parrish, *AIP Conf. Proc.* 654 (2003) 1116.
- [20] A. Budiman, S.-H. Song, T.-S. Chang, C.-H. Shin, M.-J. Choi, *Catal Surv Asia* 16 (2012) 183.
- [21] E.A. Quadrelli, G. Centi, J.-L. Duplan, S. Perathoner, *ChemSusChem* 4 (2011) 1194.
- [22] J. Ma, N. Sun, X. Zhang, N. Zhao, F. Xiao, W. Wei, Y. Sun, *Catal. Today* 148 (2009) 221.
- [23] W.-L. Dai, S.-L. Luo, S.-F. Yin, C.-T. Au, *Appl. Catal. A: Gen.* 366 (2009) 2.
- [24] S. Sankaranarayanan, K. Srinivasan, *Indian J. Chem.* 51A (2012) 1252.
- [25] T. Sakakura, K. Kohno, *Chem. Commun.* 11 (2009) 1312.
- [26] E. Leino, P. Mäki-Arvela, V. Eta, D.Y. Murzin, T. Salmi, J.P. Mikkola, *Appl. Catal. A: Gen.* 383 (2010) 1.
- [27] H.J. Hofmann, A. Brandner, P. Claus, *Chem.-Ing.-Tech.* 83 (2011) 1711.
- [28] H. Lee, S. Park, I. Song, J. Jung, *Catal. Lett.* 141 (2011) 531.
- [29] N. Kumar, E. Leino, P. Mäki-Arvela, A. Aho, M. Käldestrom, M. Tuominen, P. Laukkanen, K. Eränen, J.-P. Mikkola, T. Salmi, D.Y. Murzin, *Micropor. Mesopor. Mat.* 152 (2012) 71.

- [30] F. Gasc, S. Thiebaud-Roux, Z. Mouloungui, J. Supercrit. Fluids 50 (2009) 46.
- [31] O. Arbeláez, A. Orrego, F. Bustamante, A. Villa, Top. Catal. 55 (2012) 668.
- [32] Y. Ono, Appl. Catal. A: Gen. 155 (1997) 133.
- [33] T. Sakakura, J.C. Choi, H. Yasuda, Chem Rev 107 (2007) 2365.
- [34] N. Keller, G. Rebmann, V. Keller, J. Mol. Catal. A: Chem. 317 (2010) 1.
- [35] F. Rivetti, R. Paludetto, U. Romano, EniChem process, US Patent 5 705 673 (1998).
- [36] M. Berhil, N. Lebrun, A. Tranchant, R. Messina, J. Power Sources 55 (1995) 205.
- [37] R. Naejus, R. Coudert, P. Willmann, D. Lemordant, Electrochimica Acta 43 (1998) 275.
- [38] J.P. Parrish, R.N. Salvatore, K.W. Jung, Tetrahedron 56 (2000) 8207.
- [39] D.A. Bolon, J.E. Hallgren, General Electric Company, US Patent 4 452 968 (1984).
- [40] A.-A.G. Shaikh, S. Sivaram, Chem. Rev. 96 (1996) 951.
- [41] M. Berridge, D. Comar, C. Crouzel, Appl. Radiat. Isot. 34 (1983) 1657.
- [42] S.-K. Jeong, M. Inaba, Y. Iriyama, T. Abe, Z. Ogumi, J. Power Sources 119–121 (2003) 555.
- [43] D. Delledonne, F. Rivetti, U. Romano, Appl. Catal. A: Gen. 221 (2001) 241.
- [44] Y. Ono, Catal. Today 35 (1997) 15.
- [45] B.C. Dunn, C. Guenneau, S.A. Hilton, J. Pahnke, E.M. Eyring, J. Dworzanski, H.L.C. Meuzelaar, J.Z. Hu, M.S. Solum, R.J. Pugmire, Energ. Fuel. 16 (2002) 177.
- [46] Y. Zhou, J. Wu, E.W. Lemmon, J. Phys. Chem. Ref. Data 40 (2011) 043106.
- [47] M.A. Pacheco, C.L. Marshall, Energy & Fuels 11 (1997) 2.
- [48] X. Xiaoding, J.A. Moulijn, Energy & Fuels 10 (1996) 305.
- [49] A. Nobel, Annual Report 2015.
- [50] H.P. Kiran Pulidindi, DMC Market Size By Application, Industry Analysis Report, 2016.
- [51] R. Zevenhoven, S. Eloneva, S. Teir, Catal. Today 115 (2006) 73.
- [52] H. Babad, A.G. Zeiler, Chem. Rev. 73 (1973) 75.
- [53] M. Matzner, R.P. Kurkcy, R.J. Cotter, Chem. Rev. 64 (1964) 645.
- [54] I.E. Muskat, F. Strain, 2 379 250 (1945), PPG.
- [55] U. Romano, R. Tesei, G. Cipriani, L. Micucci, EniChem process, US Patent 4 218 391 (1980).
- [56] U. Romano, R. Tesel, M.M. Mauri, P. Rebora, Ind. Eng. Chem. Prod. RD 19 (1980) 396.
- [57] H. Miyazaki, Y. Shiomi, S. Fujitus, K. Masunaga, H. Yanagisawa, UBE industries, Patent US 4 384 133 (1983).
- [58] J. Zhen, S. Hua, C. Hua, Catal. Lett. 69 (2000) 153.
- [59] S. Tahara, K. Nishihira, M. Masuda, K. Mizutare, US Patent 4 467 109 (1984),
- [60] J.F. Knifton, Texaco process, US Patent 4 661 609 (1987).
- [61] P. Qiu, L. Wang, X. Jiang, B. Yang, Energy & Fuels 26 (2012) 1254.
- [62] M. Wang, N. Zhao, Wei, Y. Sun, Ind. Eng. Chem. Res. 44 (2005) 7596.
- [63] D. Wang, B. Yang, X. Zhai, L. Zhou, Fuel Process. Technol. 88 (2007) 807.
- [64] K. Tomishige, T. Sakaihor, Y. Ikeda, K. Fujimoto, Catal. Lett. 58 (1999) 225.
- [65] K. Tomishige, Y. Furusawa, Y. Ikeda, M. Asadullah, K. Fujimoto, Catal. Lett. 76 (2001) 71.
- [66] S. Wada, K. Oka, K. Watanabe, Y. Izumi, Front. Chem. 1 (2013) 1.
- [67] S. Wang, L. Zhao, W. Wang, Y. Zhao, G. Zhang, X. Ma, J. Gong, Nanoscale 5 (2013) 5582.
- [68] Z.-F. Zhang, Z.-W. Liu, J. Lu, Z.-T. Liu, Ind. Eng. Chem. Res. 50 (2011) 1981.
- [69] W.A. Hoffman, J. Org. Chem. 47 (1982) 5209.
- [70] A. Dibenedetto, C. Pastore, M. Aresta, Catal. Today 115 (2006) 88.
- [71] K. Kohno, J.-C. Choi, Y. Ohshima, H. Yasuda, T. Sakakura, ChemSusChem 1 (2008) 186.
- [72] M. Aresta, A. Dibenedetto, C. Pastore, Inorg. Chem. 42 (2003) 3256.

- [73] D. Ballivet-Tkatchenko, S. Chambrey, R. Keiski, R. Ligabue, L. Plasseraud, P. Richard, H. Turunen, *Catal. Today* 115 (2006) 80.
- [74] D. Ballivet-Tkatchenko, R.A. Ligabue, L. Plasseraud, *Braz. J. Chem. Eng.* 23 (2006) 111.
- [75] D. Ballivet-Tkatchenko, T. Jerphagnon, R. Ligabue, L. Plasseraud, D. Poinso, *Appl. Catal. A: Gen.* 255 (2003) 93.
- [76] J.-C. Choi, K. Kohno, Y. Ohshima, H. Yasuda, T. Sakakura, *Catal. Commun.* 9 (2008) 1630.
- [77] J.-C. Choi, L.-N. He, H. Yasuda, T. Sakakura, *Green Chem.* 4 (2002) 230.
- [78] B. Fan, H. Li, W. Fan, J. Zhang, R. Li, *Appl. Catal. A: Gen.* 372 (2010) 94.
- [79] S. Hong, H. Park, J. Lim, Y.-W. Lee, M. Anpo, J.-D. Kim, *Res. Chem. Intermediat.* 32 (2006) 737.
- [80] Q. Cai, C. Jin, B. Lu, H. Tangbo, Y. Shan, *Catal. Lett.* 103 (2005) 225.
- [81] A. Aouissi, S.S. Al-Deyab, A. Al-Owais, A. Al-Amro, *Int. J. Mol. Sci.* 11 (2010) 2770.
- [82] L.A. Allaoui, A. Aouissi, *J. Mol. Catal. A: Chem.* 259 (2006) 281.
- [83] K.W. La, J.C. Jung, H. Kim, S.-H. Baeck, I.K. Song, *J. Mol. Catal. A: Chem.* 269 (2007) 41.
- [84] C. Jiang, Y. Guo, C. Wang, C. Hu, Y. Wu, E. Wang, *Appl. Catal. A: Gen.* 256 (2003) 203.
- [85] W. Xu, S. Ji, W. Quan, J. Yu, *Modern Research in Catalysis* 2 (2013) 22.
- [86] K. Jung, A. Bell, *Top. Catal.* 20 (2002) 97.
- [87] K. Tomishige, Y. Ikeda, T. Sakaihor, K. Fujimoto, *J. Catal.* 192 (2000) 355.
- [88] V. Eta, P. Mäki-Arvela, A.-R. Leino, K. Kordás, T. Salmi, D.Y. Murzin, J.-P. Mikkola, *Ind. Eng. Chem. Res.* 49 (2010) 9609.
- [89] C.-F. Li, S.-H. Zhong, *Catal. Today* 82 (2003) 83.
- [90] J. Bian, X.W. Wei, Y.R. Jin, L. Wang, D.C. Luan, Z.P. Guan, *Chem. Eng. J.* 165 (2010) 686.
- [91] M. Aresta, A. Dibenedetto, C. Pastore, A. Angelini, B. Aresta, I. Pápai, *J. Catal.* 269 (2010) 44.
- [92] K. Almusaiter, *Catal. Commun.* 10 (2009) 1127.
- [93] H.J. Hofmann, A. Brandner, P. Claus, *Chem. Eng. Technol.* 35 (2012) 2140.
- [94] K. Tomishige, K. Kunimori, *Appl. Catal. A: Gen.* 237 (2002) 103.
- [95] G. Ranga Rao, H.R. Sahu, *J. Chem. Sci.* 113 (2001) 651.
- [96] Y. Ikeda, T. Sakaihor, K. Tomishige, K. Fujimoto, *Catal. Lett.* 66 (2000) 59.
- [97] X.L. Wu, M. Xiao, Y.Z. Meng, Y.X. Lu, *J. Mol. Catal. A: Chem.* 238 (2005) 158.
- [98] K. Arata, *Solid Superacids*, in: Herman Pines D.D. Eley, B. Weisz Paul, *Adv. Catal.*, 1990, pp. 165.
- [99] W. Wang, S. Wang, X. Ma, J. Gong, *Catal. Today* 148 (2009) 323.
- [100] I. Prymak, V.N. Kalevaru, S. Wohlrab, A. Martin, *Catal. Sci. Technol.* (2015).
- [101] M. Honda, M. Tamura, Y. Nakagawa, K. Nakao, K. Suzuki, K. Tomishige, *J. Catal.* 318 (2014) 95.
- [102] E. Leino, P. Mäki-Arvela, V. Eta, N. Kumar, F. Demoisson, A. Samikannu, A.-R. Leino, A. Shchukarev, D.Y. Murzin, J.-P. Mikkola, *Catal. Today* 210 (2013) 47.
- [103] E. Leino, P. Mäki-Arvela, K. Eränen, M. Tenho, D.Y. Murzin, T. Salmi, J.-P. Mikkola, *Chem. Eng. J.* 176–177 (2011) 124.
- [104] M. Honda, S. Kuno, N. Begum, K.-i. Fujimoto, K. Suzuki, Y. Nakagawa, K. Tomishige, *Appl. Catal. A: Gen.* 384 (2010) 165.
- [105] E. Leino, N. Kumar, P. Mäki-Arvela, A. Aho, K. Kordás, A.-R. Leino, A. Shchukarev, D.Y. Murzin, J.-P. Mikkola, *Mater. Chem. Phys.* 143 (2013) 65.



- [106] A. Dibenedetto, M. Aresta, A. Angelini, J. Ethiraj, B.M. Aresta, *Chem.-Eur. J.* 18 (2012) 10324.
- [107] M. Aresta, A. Dibenedetto, E. Fracchiolla, P. Giannoccaro, C. Pastore, I. Pápai, G. Schubert, *J. Org. Chem.* 70 (2005) 6177.
- [108] S. Xie, A. Bell, *Catal. Lett.* 70 (2000) 137.
- [109] K.T. Jung, A.T. Bell, *J. Catal.* 204 (2001) 339.
- [110] M. Honda, S. Kuno, S. Sonehara, K.-i. Fujimoto, K. Suzuki, Y. Nakagawa, K. Tomishige, *ChemCatChem* 3 (2011) 365.
- [111] A.I. Abdulagatov, G.V. Stepanov, I.M. Abdulagatov, *High Temperature* 45 (2007) 85.
- [112] L.C.W. Baker, T.F. Anderson, *J. Am. Chem. Soc.* 79 (1957) 2071.
- [113] S. Takishima, K. Saiki, K. Arai, S. Saito, *J. Chem. Eng. Jpn.* 19 (1986) 48.
- [114] J.S. Lim, Y.Y. Lee, H.S. Chun, *J. Supercrit. Fluids* 7 (1994) 219.
- [115] S.-D. Yeo, S.-J. Park, J.-W. Kim, J.-C. Kim, *J. Chem. Eng. Data* 45 (2000) 932.
- [116] L.A. Galicia-Luna, A. Ortega-Rodriguez, D. Richon, *J. Chem. Eng. Data* 45 (2000) 265.
- [117] C. Secuianu, V. Feroiu, D. Geană, *J. Supercrit. Fluids* 47 (2008) 109.
- [118] Q. Cai, B. Lu, L. Guo, Y. Shan, *Catal. Commun.* 10 (2009) 605.
- [119] S. Gurdial Gurdev, R. Foster Neil, S.L.J. Yun, D. Tilly Kevin, *Supercrit. Fluid Eng. Sci.*, American Chem. Society, 1992, pp. 34.
- [120] T. Holderbaum, *Die Vorausberechnung von Dampf-Flüssig-Gleichgewichten mit einer Gruppenbeitragszustandsgleichung*, VDI Verlag, 1991.
- [121] M. Alifanti, B. Baps, N. Blangenois, J. Naud, P. Grange, B. Delmon, *Chem. Mater.* 15 (2003) 395.
- [122] M. Muthuraman, N. Dhas, K.C. Patil, *Bull. Mater. Sci.* 17 (1994) 977.
- [123] A. Bienholz, F. Schwab, P. Claus, *Green Chem.* 12 (2010) 290.
- [124] Y. Ikeda, M. Asadullah, K. Fujimoto, K. Tomishige, *J. Phys. Chem. B* 105 (2001) 10653.
- [125] P. Scherrer, *Göttinger Nachrichten Gesell.* 2 (1918) 98.
- [126] C. Perego, S. Peratello, *Catal. Today* 52 (1999) 133.
- [127] A. Kambolis, H. Matralis, A. Trovarelli, C. Papadopoulou, *Appl. Catal. A: Gen.* 377 (2010) 16.
- [128] S. Abdollahzadeh-Ghom, C. Zamani, T. Andreu, M. Epifani, J.R. Morante, *Appl. Catal. B: Environ* 108–109 (2011) 32.
- [129] S. Yao-Matsuo, S. Otsuka, T. Yao, T. Omata, *High Temp. Mater. Processes* 22 (2003) 157.
- [130] R. Si, Y.-W. Zhang, S.-J. Li, B.-X. Lin, C.-H. Yan, *J. Phys. Chem. B* 108 (2004) 12481.
- [131] G. Postole, B. Chowdhury, B. Karmakar, K. Pinki, J. Banerji, A. Auroux, *J. Catal.* 269 (2010) 110.
- [132] G.R. Rao, T. Rajkumar, *J. Colloid Interface Sci.* 324 (2008) 134.
- [133] R. Wang, S.I. Mutinda, M. Fang, *RSC Advances* 3 (2013) 19508.
- [134] J.C. Lavalley, *Catal. Today* 27 (1996) 377.
- [135] K. Tomishige, H. Yasuda, Y. Yoshida, M. Nurunnabi, B. Li, K. Kunimori, *Green Chem.* 6 (2004) 206.
- [136] M.G. Cutrufello, I. Ferino, R. Monaci, E. Rombi, V. Solinas, *Top. Catal.* 19 (2002) 225.
- [137] B.A.V. Santos, C.S.M. Pereira, V.M.T.M. Silva, J.M. Loureiro, A.E. Rodrigues, *Appl. Catal. A: Gen.* 455 (2013) 219.
- [138] K. Müller, L. Mokrushina, W. Arlt, *Chem.-Ing.-Tech.* 86 (2014) 497.
- [139] K. Tomishige, Y. Ikeda, T. Sakaihorii, K. Fujimoto, *Catal. Lett.* 58 (1999) 225.
- [140] M. López Granados, F.C. Galisteo, P.S. Lambrou, R. Mariscal, J. Sanz, I. Sobrados, J.L.G. Fierro, A.M. Efstathiou, *J. Catal.* 239 (2006) 410.
- [141] V.K. Smitha, H. Suja, J. Joyce, S. Sugunan, *Indian J. Chem.* 42A (2003) 300.

- [142] C.E. Hori, K.Y.S. Ng, A. Brenner, K.M. Rahmoeller, D. Belton, *Brazilian J. Chem. Eng.* 18 (2001) 23.
- [143] I. Atribak, N. Guillén-Hurtado, A. Bueno-López, A. García-García, *Appl. Surf. Sci.* 256 (2010) 7706.
- [144] M. Bensitel, V. Moraver, J. Lamotte, O. Saur, J.-C. Lavalley, *Spectrochim. Acta A: M.* 43 (1987) 1487.
- [145] C. Binet, A. Badri, J.-C. Lavalley, *J. Phys. Chem.* 98 (1994) 6392.
- [146] Y. Denkwitz, A. Karpenko, V. Plzak, R. Leppelt, B. Schumacher, R.J. Behm, *J. Catal.* 246 (2007) 74.
- [147] C. Binet, M. Daturi, J.C. Lavalley, *Catal. Today* 50 (1999) 207.
- [148] C. Li, K. Domen, K.-i. Maruya, T. Onishi, *J. Catal.* 125 (1990) 445.
- [149] M. Daturi, C. Binet, J.-C. Lavalley, A. Galtayries, R. Sporken, *Phys. Chem. Chem. Phys.* 1 (1999) 5717.
- [150] J. Lamotte, V. Morávek, M. Bensitel, J.C. Lavalley, *React. Kinet. Catal. L.* 36 (1988) 113.
- [151] E.L. Crepaldi, G.J. de A. A. Soler-Illia, A. Bouchara, D. Grosso, D. Durand, C. Sanchez, *Angew. Chem. Int. Ed.* 42 (2003) 347.
- [152] M. Lundberg, B. Skårman, F. Cesar, L. Reine Wallenberg, *Micropor. Mesopor. Mat.* 54 (2002) 97.
- [153] D. Terribile, A. Trovarelli, J. Llorca, C. de Leitenburg, G. Dolcetti, *Catal. Today* 43 (1998) 79.
- [154] C.E. Hori, H. Permana, K.Y.S. Ng, A. Brenner, K. More, K.M. Rahmoeller, D. Belton, *Appl. Catal. B: Environ* 16 (1998) 105.
- [155] W. Huang, J. Yang, C. Wang, B. Zou, X. Meng, Y. Wang, X. Cao, Z. Wang, *Mater. Res. Bull.* 47 (2012) 2349.
- [156] L. Xu, H. Song, L. Chou, *Int. J. Hydrogen Energ.* 37 (2012) 18001.
- [157] M. Yashima, K. Morimoto, N. Ishizawa, M. Yoshimura, *J. Am. Ceram. Soc.* 76 (1993) 2865.
- [158] M. Yashima, K. Morimoto, N. Ishizawa, M. Yoshimura, *J. Am. Ceram. Soc.* 76 (1993) 1745.
- [159] J.I. Gutiérrez-Ortiz, B. de Rivas, R. López-Fonseca, J.R. González-Velasco, *Appl. Catal. A: Gen.* 269 (2004) 147.
- [160] M. Yashima, H. Arashi, M. Kakihana, M. Yoshimura, *J. Am. Ceram. Soc.* 77 (1994) 1067.
- [161] E. Aneggi, C. de Leitenburg, G. Dolcetti, A. Trovarelli, *Catal. Today* 114 (2006) 40.
- [162] P. Fornasiero, R. Dimonte, G.R. Rao, J. Kaspar, S. Meriani, A. Trovarelli, M. Graziani, *J. Catal.* 151 (1995) 168.
- [163] D. Srinivas, C.V.V. Satyanarayana, H.S. Potdar, P. Ratnasamy, *Appl. Catal. A: Gen.* 246 (2003) 323.
- [164] Z.Y. M. Pudukudy, *Der Pharma Chem.* 6 (2014) 188.
- [165] T. Murota, T. Hasegawa, S. Aozasa, H. Matsui, M. Motoyama, *J. Alloy Compd.* 193 (1993) 298.
- [166] A. Trovarelli, *Cataly. Rev.* 38 (1996) 439.
- [167] B. de Rivas, R. López-Fonseca, C. Sampedro, J.I. Gutiérrez-Ortiz, *Appl. Catal. B: Environ* 90 (2009) 545.
- [168] B. de Rivas, C. Sampedro, M. García-Real, R. López-Fonseca, J.I. Gutiérrez-Ortiz, *Appl. Catal. B: Environ* 129 (2013) 225.
- [169] C. Pojanavaraphan, A. Luengnaruemitchai, E. Gulari, *Int. J. Hydrogen Energ.* 38 (2013) 1348.

- [170] W. Khaodee, B. Jongsomjit, S. Assabumrungrat, P. Praserthdam, S. Goto, *Catal. Commun.* 8 (2007) 548.
- [171] B.M. Reddy, B. Chowdhury, P.G. Smirniotis, *Appl. Catal. A: Gen.* 211 (2001) 19.
- [172] F. Bustamante, A.F. Orrego, S. Villegas, A.L. Villa, *Ind. Eng. Chem. Res.* 51 (2012) 8945.
- [173] B.A.V. Santos, V.M.T.M. Silva, J.M. Loureiro, D. Barbosa, A.E. Rodrigues, *Fluid Phase Equilibr.* 336 (2012) 41.
- [174] V. Feroiu, S. Sima, D. Geană, High pressure phase equilibrium in CO<sub>2</sub>+EtOH system, 2013.
- [175] Z. Hou, B. Han, Z. Liu, T. Jiang, G. Yang, *Green Chem.* 4 (2002) 467.
- [176] Y. Yoshida, Y. Arai, S. Kado, K. Kunimori, K. Tomishige, *Catal. Today* 115 (2006) 95.
- [177] J.I. Gutiérrez-Ortiz, B. de Rivas, R. López-Fonseca, J.R. González-Velasco, *Appl. Catal. B: Environ* 65 (2006) 191.
- [178] I. Dobrosz-Gómez, M.A.G. García, M.I. Szykowska, I. Kocemba, J.M. Rynkowski, *Catal. Today* 191 (2012) 142.
- [179] M. Yashima, T. Hirose, S. Katano, Y. Suzuki, M. Kakihana, M. Yoshimura, *Phys. Rev. B* 51 (1995) 8018.
- [180] J.L.M. Rupp, A. Infortuna, L.J. Gauckler, *Acta Mater.* 54 (2006) 1721.
- [181] J. Fan, D. Weng, X. Wu, X. Wu, R. Ran, *J. Catal.* 258 (2008) 177.
- [182] P. Fornasiero, G. Balducci, R. Di Monte, J. Kašpar, V. Sergo, G. Gubitosa, A. Ferrero, M. Graziani, *J. Catal.* 164 (1996) 173.
- [183] K. Otsuka, Y. Wang, M. Nakamura, *Appl. Catal. A: Gen.* 183 (1999) 317.
- [184] A. Trovarelli, F. Zamar, J. Llorca, C.d. Leitenburg, G. Dolcetti, J.T. Kiss, *J. Catal.* 169 (1997) 490.
- [185] J. Kašpar, P. Fornasiero, M. Graziani, *Catal. Today* 50 (1999) 285.
- [186] F. Fally, V. Perrichon, H. Vidal, J. Kaspar, G. Blanco, J.M. Pintado, S. Bernal, G. Colon, M. Daturi, J.C. Lavalley, *Catal. Today* 59 (2000) 373.
- [187] M. Boaro, M. Vicario, C. de Leitenburg, G. Dolcetti, A. Trovarelli, *Catal. Today* 77 (2003) 407.
- [188] S. Damyanova, B. Pawelec, K. Arishtirova, M.V.M. Huerta, J.L.G. Fierro, *Appl. Catal. A: Gen.* 337 (2008) 86.
- [189] M.F.L. Johnson, J. Mooi, *J. Catal.* 103 (1987) 502.
- [190] V. Perrichon, A. Laachir, G. Bergeret, R. Frety, L. Tournayan, O. Touret, *J. Chem. Soc. Faraday T* 90 (1994) 773.
- [191] C. de Leitenburg, A. Trovarelli, J. Llorca, F. Cavani, G. Bini, *Appl. Catal. A: Gen.* 139 (1996) 161.
- [192] V. Bolis, C. Morterra, M. Volante, L. Orio, B. Fubini, *Langmuir* 6 (1990) 695.
- [193] I. Prymak, V. N. Kalevaru, P. Kollmorgen, S. Wohlrab, A. Martin, *DGMK-Tagungsbericht* 2 (2013) 249.
- [194] I. Prymak, V.N. Kalevaru, S. Wohlrab, A. Martin, *Catal. Sci. Technol.* 5 (2015) 2322.
- [195] I. Prymak, V.N. Kalevaru, S. Wohlrab, A. Martin, *DGMK-Tagungsbericht* 3 (2014) 211.
- [196] P. Biswas, D. Kunzru, *Int. J. Hydrogen Energ.* 32 (2007) 969.
- [197] T. Masui, K. Fujiwara, Y. Peng, T. Sakata, K.-i. Machida, H. Mori, G.-y. Adachi\*, *Journal of Alloys and Compounds* 269 (1998) 116.
- [198] K.I. Hadjiivanov, D.G. Klissurski, *Chem. Soc. Rev.* 25 (1996) 61.
- [199] P. Bharali, G. Thrimurthulu, L. Katta, B.M. Reddy, *J. Ind. Eng. Chem.* 18 (2012) 1128.
- [200] J. Fang, X. Bi, D. Si, Z. Jiang, W. Huang, *Appl. Surf. Sci.* 253 (2007) 8952.
- [201] C. Pojanavaraphan, A. Luengnaruemitchai, E. Gulari, *Int. J. of Hydrog. Energy* 37 (2012) 14072.

- [202] G. Balducci, J. Kašpar, P. Fornasiero, M. Graziani, M.S. Islam, J.D. Gale, *J. Phys. Chem. B* 101 (1997) 1750.
- [203] F. Zamar, A. Trovarelli, C. de Leitenburg, G. Dolcetti, *J. Chem. Soc., Chem. Commun.* (1995) 965.
- [204] G. Balducci, P. Fornasiero, R. Di Monte, J. Kaspar, S. Meriani, M. Graziani, *Catal. Lett.* 33 (1995) 193.
- [205] J. Fang, F. Shi, H. Bao, K. Qian, Z. Jiang, W. Huang, *Chin. J. Catal.* 34 (2013) 2075.
- [206] I. Yoshiki, F. Yutaka, T. Keiichi, F. Kaoru, *CO<sub>2</sub> Conversion and Utilization*, American Chemical Society, 2002, pp. 71.
- [207] Y. Zhou, S. Wang, M. Xiao, D. Han, Y. Lu, Y. Meng, *RSC Advances* 2 (2012) 6831.
- [208] A.E. Nelson, K.H. Schulz, *Appl. Surf. Sci.* 210 (2003) 206.
- [209] Z. Zhang, Y. Zhang, Z. Mu, P. Yu, X. Ni, S. Wang, L. Zheng, *Appl. Catal. B Environ* 76 (2007) 335.
- [210] T. Luo, R.J. Gorte, *Appl. Catal. B* 53 (2004) 77.
- [211] A. Cabanas, J.A. Darr, E. Lester, M. Poliakoff, *J. Mater. Chem.* 11 (2001) 561.
- [212] X. Liang, X. Wang, Y. Zhuang, B. Xu, S. Kuang, Y. Li, *J. Am. Chem. Soc.* 130 (2008) 2736.
- [213] B. Zhao, G. Li, C. Ge, Q. Wang, R. Zhou, *Appl. Catal. B: Environ* 96 (2010) 338.
- [214] B. de Rivas, R. López-Fonseca, M.A. Gutiérrez-Ortiz, J.I. Gutiérrez-Ortiz, *Appl. Catal. B: Environ* 104 (2011) 373.
- [215] C.J. Shih, Y.J. Chen, M.H. Hon, *Mater. Chem. Phys.* 121 (2010) 99.
- [216] T. García, B. Solsona, S.H. Taylor, *Appl. Catal. B Environ.* 66 (2006) 92.
- [217] C.-J. Yoo, D.-W. Lee, M.-S. Kim, D.J. Moon, K.-Y. Lee, *J. Mol. Catal. Chem.* 378 (2013) 255.
- [218] M.J. Hudson, J.A. Knowles, *J. Mater. Chem.* 6 (1996) 89.
- [219] M. Adamowska, S. Muller, P. Da Costa, A. Krzton, P. Burg, *Appl. Catal. B: Environ* 74 (2007) 278.
- [220] E. Díaz, B. de Rivas, R. López-Fonseca, S. Ordóñez, J.I. Gutiérrez-Ortiz, *J. Chromatogr. A* 1116 (2006) 230.
- [221] I. Prymak, O. Prymak, J. Wang, N.V. Kalevaru, A. Martin, U. Bentrup, S. Wohlrab, *ChemCatChem* 10 (2018) 391.
- [222] M. Aresta, A. Dibenedetto, C. Pastore, C. Cuocci, B. Aresta, S. Cometa, E. De Giglio, *Catal. Today* 137 (2008) 125.
- [223] B. Fan, J. Zhang, R. Li, W. Fan, *Catal. Lett.* 121 (2008) 297.
- [224] X.J. Wang, M. Xiao, S.J. Wang, Y.X. Lu, Y.Z. Meng, *J. Mol. Catal. A: Chem.* 278 (2007) 92.
- [225] X.L. Wu, Y.Z. Meng, M. Xiao, Y.X. Lu, *J. Mol. Catal. A: Chem.* 249 (2006) 93.
- [226] T. Sakakura, J.-C. Choi, Y. Saito, T. Sako, *Polyhedron* 19 (2000) 573.
- [227] L. Wang, H. Li, S. Xin, P. He, Y. Cao, F. Li, X. Hou, *Appl. Catal. A: Gen.* 471 (2014) 19.
- [228] M. Honda, A. Suzuki, B. Noorjahan, K.-i. Fujimoto, K. Suzuki, K. Tomishige, *Chem. Commun.* (2009) 4596.
- [229] G. Busca, *Phys. Chem. Chem. Phys.* 1 (1999) 723.

## 9. Appendices

### *Appendix A: List of supporting figures, tables and discussions*

#### *A1 State of the art: Carboxylation of alcohols*

**Table A1.1.** Important studies related to carboxylation of ethanol to DEC.

	Catalyst	Type of reaction	Conditions				DEC-Yield	Remarks	Year [Reference]
			T (°C)	p (bar)	EtOH (mmol)	t (h)			
1.	Ce <sub>0.8</sub> Zr <sub>0.2</sub> O <sub>2</sub>	Continuous	140	140	n <sub>EtOH</sub> : n <sub>CO2</sub> = 1 : 6	1	0.7	Acid-base bifunctional catalyst; Sc conditions.	2015 [100]
2.	Nb <sub>2</sub> O <sub>5</sub> /CeO <sub>2</sub>	Batch (4×parallel reactors, 10 cm <sup>3</sup> )	135	50	68.5	3	0.7	The presence of Nb ions in the CeO <sub>2</sub> lattice increased the total acidity, while the increase of basic sites was due to a distortion of CeO <sub>2</sub> lattice.	2012 [106]
		Continuous (100 cm <sup>3</sup> )	135	300	n <sub>EtOH</sub> /n <sub>CO2</sub> = 1/4	-	0.9	Under sc conditions, EtOH and CO <sub>2</sub> were in the single phase; the higher was pressure, the higher was conversion of EtOH into DEC.	
3.	Cu-Ni/AC	Continuous	90	13	n <sub>EtOH</sub> /n <sub>CO2</sub> = 2	3	1.9	Molar ratio Cu:Ni=3:1; Cu-Ni bimetallic catalyst–activation of CO <sub>2</sub> at moderate T and p, ethanol through dissociative adsorption.	2012 [31]
4.	K <sub>2</sub> CO <sub>3</sub> –C <sub>2</sub> H <sub>5</sub> I	Batch (200 cm <sup>3</sup> )	110	80	856	5	46 (one-pot reaction)	Sc conditions; K <sub>2</sub> CO <sub>3</sub> acted as base, C <sub>2</sub> H <sub>5</sub> I-co-reagent, PTC-phase transfer catalyst; possible: one- or two-steps reactions; the sc CO <sub>2</sub> acts as swelling solvent	2009 [30]
	K <sub>2</sub> CO <sub>3</sub> –C <sub>2</sub> H <sub>5</sub> I-PTC				1200		51 (two steps reaction)		
5.	Ce <sub>0.07</sub> Zr <sub>0.93</sub> O <sub>2</sub>	Batch (100 cm <sup>3</sup> )	140	80	257	2	0.16	Catalytic performance was related to crystal structure and acid-base properties; catalyst was recyclable.	2009 [99]

**Table A1.2.** Important studies related to carboxylation of methanol to DMC.

	Catalyst	Type of reaction	Conditions				Y-DMC	Remarks	Year [Reference]
			T (°C)	p (bar)	MeOH (mmol)	t (h)			
1.	Ce <sub>0.8</sub> Zr <sub>0.2</sub> O <sub>2</sub> /H <sub>3</sub> PO <sub>4</sub>	Batch (25 cm <sup>3</sup> )	170	65	247	1	1.6	P/Zr = 0.12; P-modification caused to a decrease of moderate and strong basic sites and increase of Lewis acidic sites	2018 [221]
2.	Cu-CeO <sub>2</sub>	Batch (120 cm <sup>3</sup> )	120	13	247	2	0.4	Mild reaction conditions; pretreatment effect in H <sub>2</sub> of catalyst.	2013 [66]
3.	CeO <sub>2</sub>	Batch (100 cm <sup>3</sup> )	140	50	370	2	0.4	Different morphology of CeO <sub>2</sub> : nano-octahedrons, nano-rods, nano-cubes and spindle-like structure; spindle-like ceria and nano-rods possessed nearly equal amount of acid-base sites.	2013 [67]
		Batch (70 cm <sup>3</sup> )	130	60	192	5	0.4	Various kinds of Ce-precursors; effect of calcination temperature; CeO <sub>2</sub> -HS calcined at 600 °C showed high Y-DMC.	2006 [176]
4.	Ce <sub>x</sub> Zr <sub>1-x</sub> O <sub>2</sub>	Batch (30 cm <sup>3</sup> )	170	65	247	1	0.7	Different reaction temperature: the higher was temperature the lower was amount of DMC formed.	2012 [93]
		Continuous	150	18	n <sub>MeOH</sub> /n <sub>CO2</sub> =1	16 TOS	0.25	Different reaction conditions: T, p, MeOH/CO <sub>2</sub> ratio; the correlation of catalytic activity with specific adsorbates species (DRIFT spectroscopy).	
		Batch (70 cm <sup>3</sup> )	110	210	192	16	0.8	High calcination temperature (1000 °C) was favorable though crystal size became larger hence BET-SA was lower.	2001 [65]
5.	Cu-Fe/SiO <sub>2</sub>	Continuous	120	120	-	7 TOS	4.6	Pretreatment in H <sub>2</sub> of Cu-Fe/SiO <sub>2</sub> ; Cu-Fe bimetallic catalysts exhibited a good activity	2012 [207]
6.	5Ga <sub>2</sub> O <sub>3</sub> /Ce <sub>0.6</sub> Zr <sub>0.4</sub> O <sub>2</sub>	Batch (75 cm <sup>3</sup> )	170	60	741	3	0.3	Modification of the acid-base properties of Ce <sub>0.6</sub> Zr <sub>0.4</sub> O <sub>2</sub> by addition of Ga <sub>2</sub> O <sub>3</sub> .	2011 [28]

7.	CeO <sub>2</sub> /Al <sub>2</sub> O <sub>3</sub>	Continuous (4×parallel reactor, 20 cm <sup>3</sup> )	135	50	68.5	3	n <sub>DMC</sub> /n <sub>cat.</sub> = 0.8	Al loading-strong stabilization of the catalyst that can be used for several cycles; nanoparticles with 5-20 nm size.	2010 [91] 2008 [222]
8.	Sn/SBA-15	Batch (100 cm <sup>3</sup> )	240	180	490	10	2.43 TON	Encapsulation/immobilization of organotin compounds on the mesostructured silica; under high pressure the reaction mixture became homogeneous.	2008 [223]
9.	Ce <sub>x</sub> Ti <sub>1-x</sub> O <sub>2</sub> /H <sub>3</sub> PW <sub>12</sub> O <sub>40</sub>	Batch (100 cm <sup>3</sup> )	170	50	200	12	2.5	Catalytic activity increased with increasing acidity and basicity of catalysts; H <sub>3</sub> PW <sub>12</sub> O <sub>40</sub> provided the Brønsted acid sites.	2007 [83]
10.	Cu-Ni/V <sub>2</sub> O <sub>5</sub> -SiO <sub>2</sub>	Continuous, photo-reactor, UV irradiation	120	1	-	-	4	Pretreatment in H <sub>2</sub> ; UV irradiation reduced the reaction pressure to 1 atm and DMC yield increased double compared with pure thermal surface catalytic reaction.	2007 [224]
		Continuous	140	6	n <sub>MeOH</sub> /n <sub>CO<sub>2</sub></sub> = 2	-	1.1	High temperature led to decreasing CO <sub>2</sub> adsorption; high crystallinity of catalyst resulted in a better performance.	2006 [225]
11.	n-Bu <sub>2</sub> Sn(OMe) <sub>2</sub>	Batch (125 cm <sup>3</sup> )	150	200	494	15	0.8	At pressure higher than 160 bar, CO <sub>2</sub> acts as solvent and reactant; at 200 bar - monophasic supercritical medium.	2006 [73, 74]
		Batch (20 cm <sup>3</sup> )	180	300	200	24	1.1	Catalytic activity was strongly dependent on the CO <sub>2</sub> pressure.	2000 [226]
12.	V <sub>2</sub> O <sub>5</sub> /H <sub>3</sub> PO <sub>4</sub>	Continuous	140	6	n <sub>MeOH</sub> /n <sub>CO<sub>2</sub></sub> = 2	-	1.8	The optimum composition of V <sub>2</sub> O <sub>5</sub> /H <sub>3</sub> PO <sub>4</sub> with P/V=0.15-0.50 – activation of both CO <sub>2</sub> and MeOH; V and P – weak Brønsted acid sites, activation of MeOH.	2005 [97]
13.	ZrO <sub>2</sub>	Batch (30 cm <sup>3</sup> )	170	60	82	16	0.5	The surface of ZrO <sub>2</sub> consisted of monoclinic and tetragonal phases showed a high DMC yield; the neighboring acid-base sites on ZrO <sub>2</sub> surface were active for DMC formation.	2002 [86, 109] 2000 [87] 1999 [64]
14.	ZrO <sub>2</sub> /H <sub>3</sub> PO <sub>4</sub>	Batch (70 cm <sup>3</sup> )	130	60	192	2	0.16	ZrO <sub>2</sub> had only Lewis acid sites; ZrO <sub>2</sub> /H <sub>3</sub> PO <sub>4</sub> (P/Zr=0.05) showed Brønsted as well as Lewis acid sites.	2001[124] 2000 [96]

**Table A1.3.** DMC and DEC syntheses using dehydration agents.

Organic carbonate	Catalyst	Dehydrating agent	Type of reaction	Conditions				Yield	Remarks	Year [Reference]
				T (°C)	p (bar)	R-OH (mmol)	t (h)			
1. DEC	KI/EtONa	Ethylene oxide (45 mmol)	Batch (150 cm <sup>3</sup> )	170	30	680	2	63.6	Homogeneous catalyst; mild reaction conditions; recycling of catalyst; reaction products: diethyl carbonate, ethylene glycol, ethylene carbonate, ethinyl estradiol.	2014 [227]
2. DMC DEC	CeO <sub>2</sub>	2-Cyanopyridine (100 mmol)	Batch (190 cm <sup>3</sup> )	120	50	20	16 24	96 91	The hydration of 2-cyanopyridine was very fast and carboxylation of methanol with CO <sub>2</sub> proceeded via two times nucleophilic addition of methoxy group on CeO <sub>2</sub> .	2014 [101]
3. DEC	CeO <sub>2</sub>	Butylene oxide (19 mmol)	Batch (300 cm <sup>3</sup> )	180	90	314	25	0.6	Various preparation conditions (time, calcination temperature and pH) → different catalytic performance of CeO <sub>2</sub> ; CeO <sub>2</sub> prepared under pH 11 of the solution resulted in the highest Y-DEC.	2013 [105] 2011 [103]
4. DEC	CeO <sub>2</sub> /SBA-15	Butylene oxide (19 mmol)	Batch (300 cm <sup>3</sup> )	180	90	314	25	n <sub>DEC</sub> /n <sub>Ce</sub> = 0.28	CeO <sub>2</sub> prepared by precipitation and hydrothermal methods; Ce supported on SBA-15 contained high amount of basic sites.	2013 [102]
5. DEC	16 wt% Ce-H-MCM-41	Butylene oxide (19 mmol)	Batch (300 cm <sup>3</sup> )	170	45	314	23	n <sub>DEC</sub> /n <sub>Ce</sub> = 0.09	Amount and type of basic sites influenced the synthesis of DEC.	2012 [29]
6. DEC	none	Polymeric organic membrane PERVAP 1211	Continuous	80	1	Feed rate 10 mL min <sup>-1</sup>		2.3	All membranes placed after reactor at atmospheric pressure; after pervaporation (feed starting volume = 160 mL, 30 cycles) had a water content of 30-50 ppm suited for running a new carboxylation cycle.	2012 [106]



			Tubular inorganic ceramic membrane	Continuous	130	1	Feed rate 300 mL min <sup>-1</sup>	3		NaA-type tubular ceramic membrane: reduced a water content of ethanolic mixture to 100-150 ppm; the membrane was not permeable; ability in removing water was drastically decreased in presence of CO <sub>2</sub> .	
7.	DMC	CeO <sub>2</sub>	Benzonitrile (200 mmol)	Batch (190 cm <sup>3</sup> )	5	150	100	2	5	The adding of C <sub>6</sub> H <sub>5</sub> CN drastically promoted DMC formation at low CO <sub>2</sub> pressure.	2011 [110]
8.	DEC DMC	CeO <sub>2</sub>	Acetonitrile (300 mmol)	Batch (190 cm <sup>3</sup> )	150	2	100	24	6.5 6	The formation amount of DEC and DMC was caused by the difference in the activity of acetonitrile hydration.	2010 [104]
9.	DMC	CeO <sub>2</sub>	Acetonitrile (300 mmol)	Batch (190 cm <sup>3</sup> )	150	5	100	48	8.94	In situ dehydration of the reaction system; low CO <sub>2</sub> pressure.	2009 [228]
			2,2-Dimethoxypropane (20 mmol)		150	5	100	2	0.3	2,2-Dimethoxypropane was not suitable as dehydrant under low CO <sub>2</sub> pressure.	
10.	DMC	CuCl	N,N'-Dicyclohexylcarbodiimide (2.47 mmol)	Batch (70 cm <sup>3</sup> )	65	50	247	24	83	Mild reaction conditions; CuCl and CuCl <sub>2</sub> catalysts (Lewis acid) improved the formation of carbonates.	2005 [107]
	DEC		N,N'-Dicyclohexylcarbodiimide (2.44 mmol)				171		46		
11.	DMC	Cu-KF/MgSiO	none	Batch	130	100	n <sub>MeOH</sub> /n <sub>CO2</sub> = 2	-	5.9	Acid-base catalyst, where the active centers were Lewis acid and Lewis base.	2003 [89]
			Mesoporous silica membrane supported on TiO <sub>2</sub> /K-M ceramic tubes	Continuous	120	4	n <sub>MeOH</sub> /n <sub>CO2</sub> = 2.2		7.4	The use of MCR promoted the reaction conversion, avoid side-reaction and increase the selectivity by removal of products on time; T improved the adsorption capacity of membrane; the increasing of p was limited by air-proof	

					130	4	$n_{\text{MeOH}}/n_{\text{CO}_2}$ = 2.4	8.8	conditions (silicon rubber, max 5 bar); hybrid membranes had excellent thermal and hydrophilic properties.		
					130	4	$n_{\text{MeOH}}/n_{\text{CO}_2}$ = 2.4	8.3			
12.	DMC	$\text{Bu}_2\text{Sn}(\text{OMe})_2$	Molecular sieve 3A (15 g)	Batch (20cm <sup>3</sup> ) with internal recycle	180	300	100	72	45	Sc CO <sub>2</sub> ; at 200 bar-single homogeneous phase; MS was recyclable and there was no co-product in comparison with using orthoesters or acetals; an extra consumption of energy to cool the loop with MS3A.	2002 [77]

## A2. Catalyst synthesis

### A2.1. Citrate complexation method: $Ce_xZr_{1-x}O_2$

For the correct calculation of the specific  $Ce_xZr_{1-x}O_2$  stoichiometries the determination of  $x$  in  $ZrO(NO_3)_2 \cdot xH_2O$  is absolutely essential.  $x$  was calculated from the thermal decomposition of the Zr precursor studied by TG under air. As shown in Figure A2.1.1, the TG curve had two stages of weight loss in the temperature range from r.t. to 405 °C. The first one starts at r.t. until ~178 °C while the second one took place above 178 °C and ends at ca. 405 °C. The weight loss of 25 wt.% at low temperature and 37 wt.% at higher temperature were caused by  $H_2O$  elimination and decomposition of nitrate precursor ( $ZrO(NO_3)_2 \cdot 4H_2O$ ), respectively. Assuming that the first peak is due to the evolution of water,  $x$  was calculated with ~4. Hence, the molar composition was  $ZrO(NO_3)_2 \cdot 4H_2O$ . No weight loss was observed beyond 405 °C until 1000 °C.

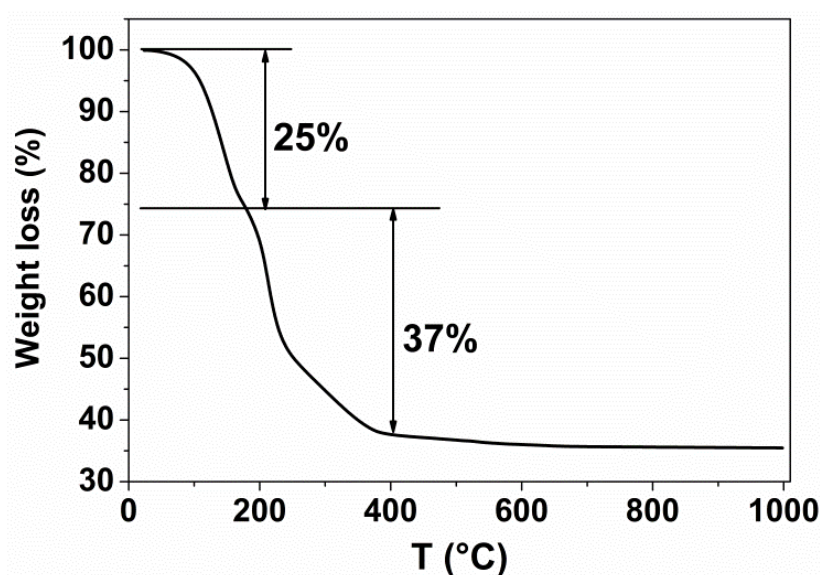


**Figure A2.1.1.** TG curve of thermal decomposition of  $ZrO(NO_3)_2 \cdot xH_2O$  under air.

### A2.2. Preparation of $TiO(NO_3)_2$ precursor for $Ce_{0.8}Ti_{0.2}O_2$ catalyst

Based on the fact that titanyl nitrate is not commercially available,  $TiO(NO_3)_2$  [122] was prepared and used as precursor for  $Ce_{0.8}Ti_{0.2}O_2$ . Titanyl nitrate,  $TiO(NO_3)_2$ , was synthesized by the addition of a 6 vol.% solution of  $NH_4OH$  to titanium tetrachloride till a pH value of 11 was reached (Scheme A2.2.1).



The synthesis was conducted at 0 °C under vigorous stirring. First, a white precipitate,  $\text{TiO}(\text{OH})_2$ , was obtained (Scheme 2.2.1). The precipitate was washed several times with distilled water. Afterwards, 1M nitric acid was added to freshly precipitated  $\text{TiO}(\text{OH})_2$  until the final pH of mixed solution reached 1 (Scheme A2.2.2). Hydrothermally, the titanyl nitrate solution was treated at 80 °C for 3h and then dried at 100 °C for 24 hours. The amount of Ti in the solid was determined by ICP.

**Remark:**  $\text{TiCl}_4$  is a fuming liquid and hydrolysis in the presence of moisture forms HCl gas and  $\text{TiOCl}_2$ . Therefore,  $\text{TiO}(\text{OH})_2$  is preferably prepared under ice-cold conditions.

**Table A2.1.1.** Preparation of  $\text{TiO}(\text{NO}_3)_2$  precursor by treatment of  $\text{TiO}(\text{OH})_2$  by nitric acid.

Precursor	$\text{TiCl}_4$ (g)	6 vol.% $\text{NH}_4\text{OH}$ (mL)	1M $\text{HNO}_3$ (mL)	Drying (T <sub>D</sub> /t)	ICP (wt.% Ti)
$\text{TiO}(\text{NO}_3)_2$	38.6	200	150	100 °C/24h	53.8

### A3 Catalyst characterization

#### A3.1. P-modified $Ce_{0.8}Zr_{0.2}O_2$ catalyst

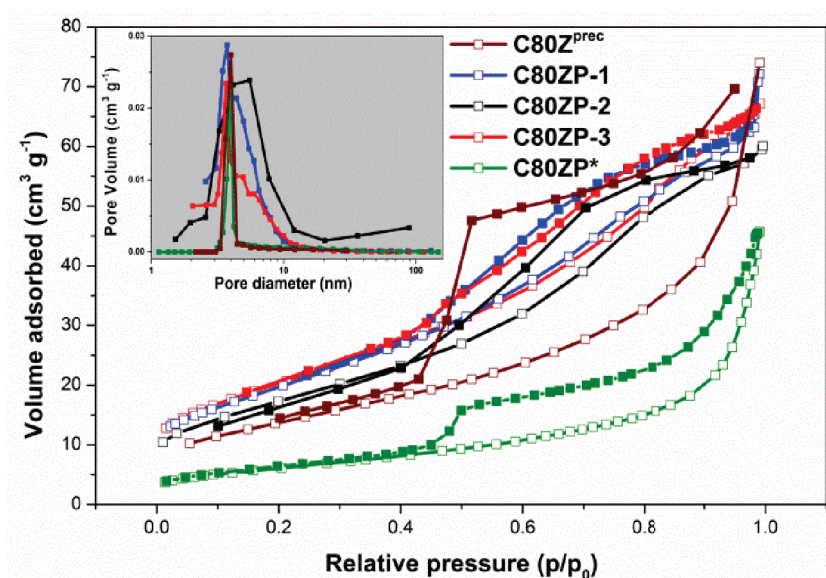


**Figure A3.1.1.**  $N_2$  adsorption-desorption isotherms ( $\square$  adsorption,  $\blacksquare$  desorption) and pore size distribution curves (inset) calculated from the desorption branch using the BJH method for unmodified  $C80Z^{prec}$  and P-modified C80Z catalysts.

**Table A3.1.1.**  $H_2$  uptake and temperature of maximal hydrogen consumption ( $T_{max}$ ) during TPR runs for unmodified  $Ce_xZr_{1-x}O_2$  and modified C80ZP-2 solids.

Sample	Peak max ( $^{\circ}C$ )	$H_2$ -uptake ( $mmol\ g^{-1}$ )
$Z^{prec}$	673	0.207
$C20Z^{prec}$	534	0.968
$C40Z^{prec}$	529	1.088
$C60Z^{prec}$	477, 712	1.435
$C80Z^{prec}$	447, 706	1.414
C80ZP-2	495, 703	1.103
$C^{prec}$	180, 454, 730	1.303

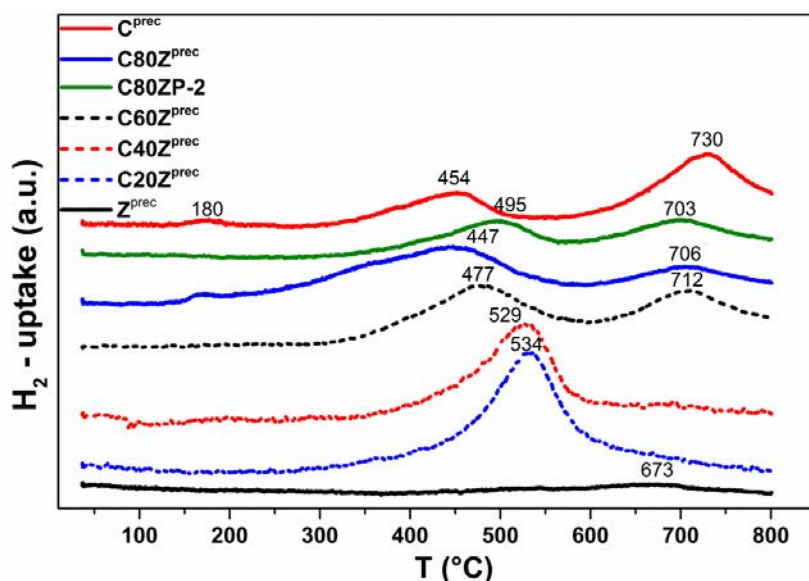
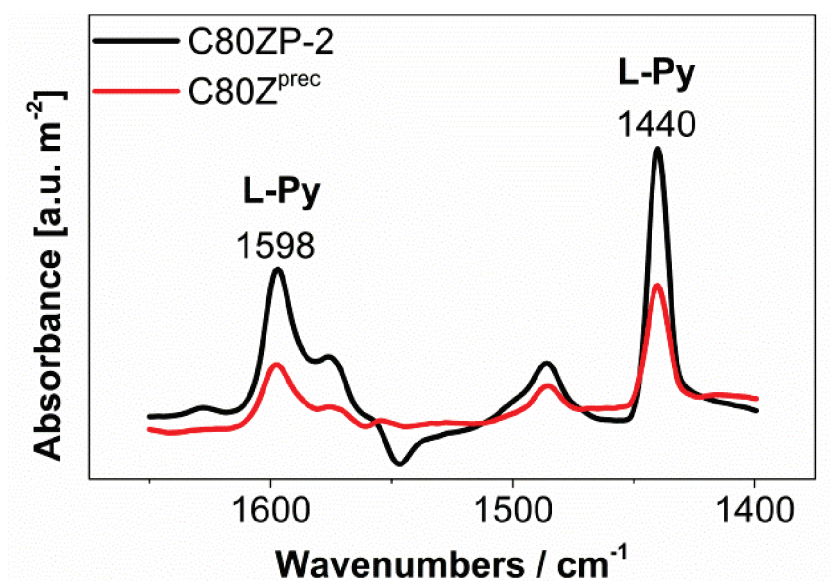


**Figure A3.1.2** H<sub>2</sub>-TPR profiles of unmodified Ce<sub>x</sub>Zr<sub>1-x</sub>O<sub>2</sub> and P-modified C80ZP-2 solids.

### ***Infrared spectroscopy of absorbed pyridine (Py-IR)***

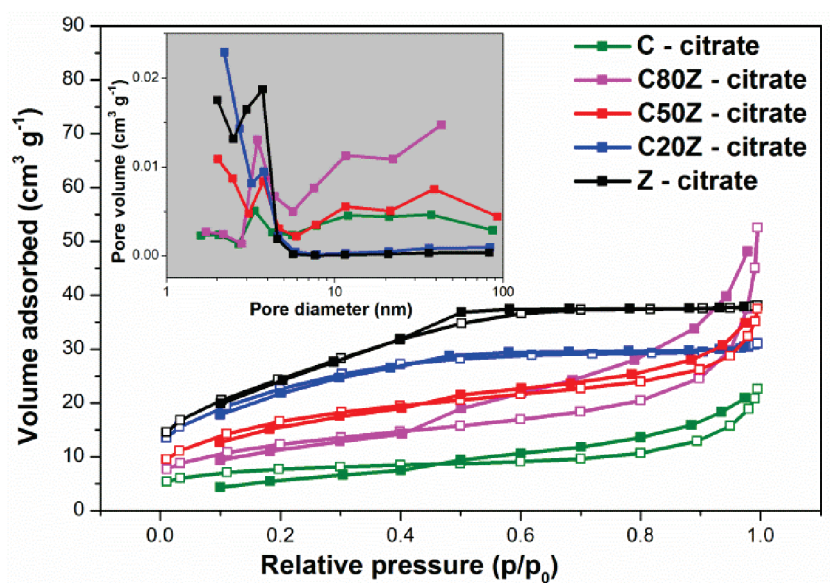
Pyridine adsorption studies were used to investigate the surface acid properties of unmodified C80Z<sup>prec</sup> and P-modified C80ZP-2 samples. The Lewis acid site concentrations were calculated based on the intensity of the band at 1440 cm<sup>-1</sup> in the spectra recorded at 150 °C [229]. The measurements in transmission mode were carried out on a Bruker Tensor 27 FTIR spectrometer equipped with a heatable and evacuable homemade reaction cell with CaF<sub>2</sub> windows connected to a gas-dosing and evacuation system. The sample powders were pressed into self-supporting wafers with a diameter of 20 mm and a weight of 50 mg. Before pyridine adsorption, the samples were pretreated by heating in synthetic air up to 400 °C for 10 min, subsequent cooling to RT and evacuation (around 0.02 mbar). Pyridine was adsorbed at RT until saturation. Then the reaction cell was evacuated for removing physisorbed pyridine. The desorption of pyridine was followed by heating the sample in vacuum up to 400 °C and recording spectra every 50 K.

Py-IR results are shown in Figure A3.1.3. A significant increase of the intensity of the band at 1440 cm<sup>-1</sup> is observed for phosphated C80ZP-2 catalyst compared to un-phosphated C80Z<sup>prec</sup>. These bands are assigned to Lewis acid sites.



**Figure A3.1.3.** Py-IR spectra of adsorbed pyridine at 150 °C on C80Z<sup>prec</sup> and C80ZP-2 catalysts.

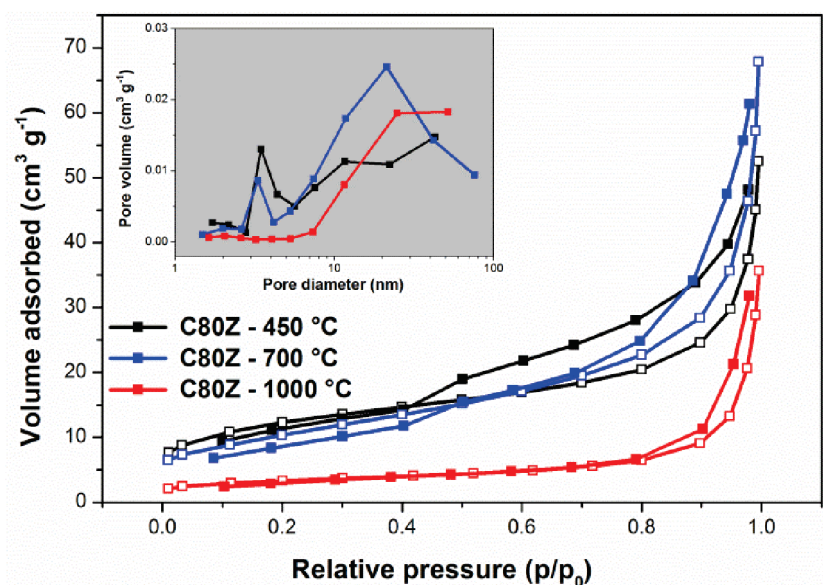
### A3.2. $Ce_xZr_{1-x}O_2$ catalysts: effect of Ce content



**Figure A3.2.1.** N<sub>2</sub> adsorption-desorption isotherms (□ adsorption, ■ desorption) and pore size distribution curves (inset) calculated from the desorption branch using the BJH method for Ce<sub>x</sub>Zr<sub>1-x</sub>O<sub>2</sub> catalysts (T<sub>c</sub> = 450 °C).

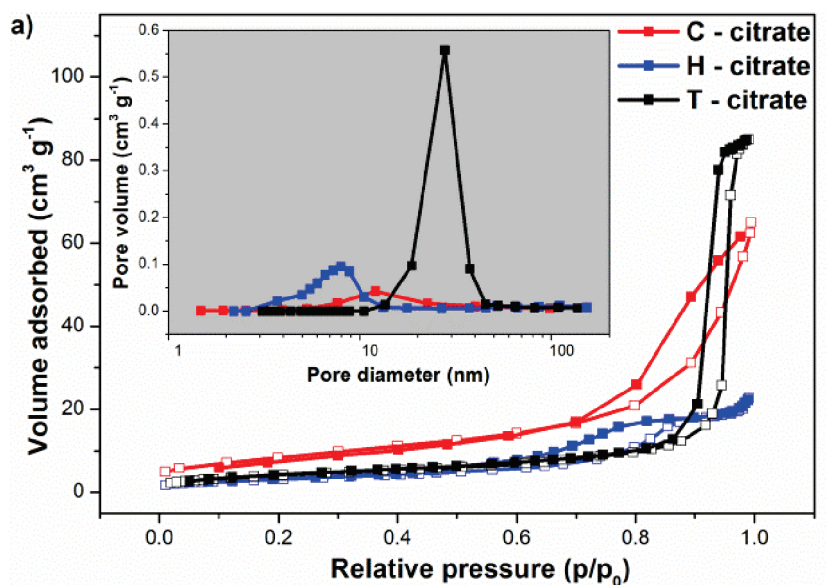


### A3.3. $Ce_{0.8}Zr_{0.2}O_2$ catalyst: effect of calcination temperature



**Figure A3.3.1.**  $N_2$  adsorption-desorption isotherms (□ adsorption, ■ desorption) and pore size distribution curves (inset) calculated from the desorption branch using the BJH method for C80Z-citrate catalysts calcined at 450, 700, 1000 °C.

### A3.4. $Ce_{0.8}M_{0.2}O_2$ catalyst: effect of second metal





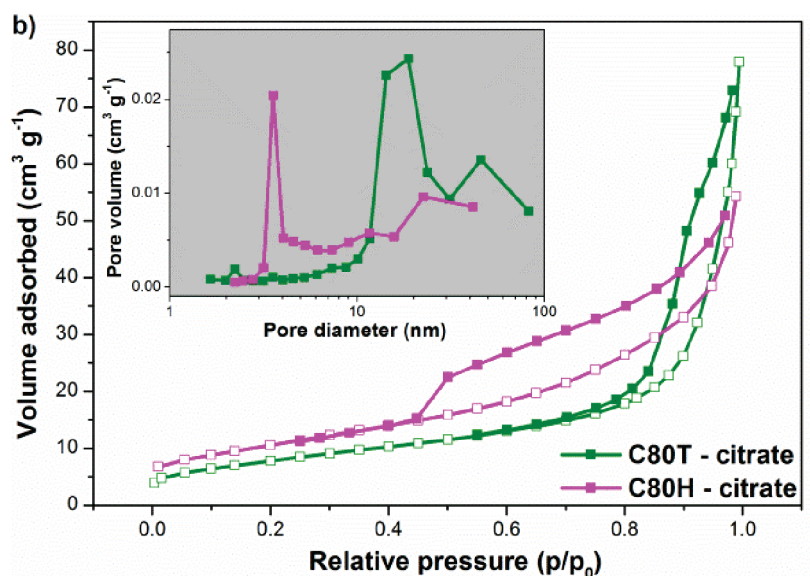


**Figure A3.4.1.** N<sub>2</sub> adsorption-desorption isotherms (□ adsorption, ■ desorption) and pore size distribution curves (inset) calculated from the desorption branch using the BJH method for (a) pure CeO<sub>2</sub>, HfO<sub>2</sub> and TiO<sub>2</sub> and (b) mixed oxides (T<sub>c</sub> = 700 °C).

### A3.5. *Ce<sub>0.8</sub>M<sub>0.2</sub>O<sub>2</sub> catalyst: effect of preparation method*

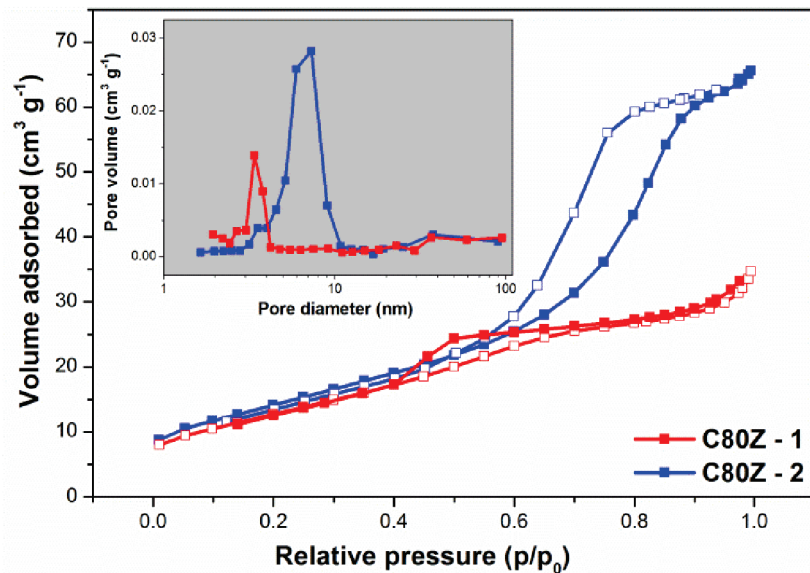


**Figure A3.5.1.** N<sub>2</sub> isotherms (□ adsorption, ■ desorption) and the corresponding BJH pore size distribution curves (inset) of C80Z-1 and C80Z-2.

## Appendix B

### List of publications

1. **Application of  $\text{Ce}_x\text{Zr}_{1-x}\text{O}_2$  catalysts for the synthesis of diethyl carbonate from ethanol and carbon dioxide**  
I. Prymak, V. N. Kalevaru, P. Kollmorgen, S. Wohlrab, A. Martin, DGMK Tagungsbericht 2 (2013) 249 (ISBN 978-3-941721-32-6)
2. **Impact of calcination temperature on the catalytic properties of Ce-Zr-O solids in the direct synthesis of diethyl carbonate from ethanol and  $\text{CO}_2$ .**  
I. Prymak, O. Prymak, V. N. Kalevaru, S. Wohlrab, A. Martin, DGMK Tagungsbericht 3 (2014) 211 (ISBN 978-3-941721-44-9)
3. **Continuous synthesis of diethyl carbonate from ethanol and  $\text{CO}_2$  over Ce-Zr-O catalysts**  
I. Prymak, V. N. Kalevaru, S. Wohlrab, A. Martin, Catal. Sci. Technol. 5 (2015) 2322 (DOI: 10.1039/C4CY01400F)
4. **Phosphate functionalization of  $\text{CeO}_2\text{-ZrO}_2$  solid solutions for the catalytic formation of dimethyl carbonate from methanol and carbon dioxide**  
I. Prymak, O. Prymak, J. Wang, V. N. Kalevaru, A. Martin, U. Bentrup and S. Wohlrab, ChemCatChem 10 (2018) 391 (DOI: 10.1002/cctc.201701105)

**Conference contributions**

1. **Direct synthesis of diethyl carbonate from ethanol and carbon dioxide over  $\text{Ce}_x\text{Zr}_{1-x}\text{O}_2$  catalysts.**  
I. Prymak, V. N. Kalevaru, P. Kollmorgen, S. Wohlrab, A. Martin  
 "46 Jahrestreffen Deutscher Katalytiker", Weimar 13-15 March 2013 (poster).
2. **One-step synthesis of diethyl carbonate from ethanol and  $\text{CO}_2$  using Ce-Zr-O catalysts.**  
I. Prymak, V. N. Kalevaru, P. Kollmorgen, S. Wohlrab, A. Martin  
 Workshop CaSuS Göttingen / LIKAT Rostock, Rostock, 16-18 September 2013 (poster).
3. **Application of  $\text{Ce}_x\text{Zr}_{1-x}\text{O}_2$  catalysts for the synthesis of diethyl carbonate from ethanol and carbon dioxide.**  
I. Prymak, V. N. Kalevaru, P. Kollmorgen, S. Wohlrab, A. Martin  
 DGMK-conference "New Technologies and Alternative Feedstocks in Petrochemistry and Refining", Dresden, 9-11 October 2013 (poster).
4. **Studies on Ce-Zr-O catalysts and their application for one-pot syntheses of diethyl carbonate from ethanol and  $\text{CO}_2$ .**  
I. Prymak, V. N. Kalevaru, P. Kollmorgen, S. Wohlrab, A. Martin  
 "47 Jahrestreffen Deutscher Katalytiker", Weimar, 12-14 March 2014 (poster).
5. **Impact of calcination temperature on the catalytic properties of Ce-Zr-O solids in the direct synthesis of diethyl carbonate from ethanol and  $\text{CO}_2$ .**  
I. Prymak, O. Prymak, V. N. Kalevaru, S. Wohlrab, A. Martin  
 DGMK-conference "Selective Oxidation and Functionalization: Classical and Alternative Routes and Sources", Berlin, 13-15 October 2014 (poster).

## ***Appendix C: Curriculum Vitae***

### Personal information

Full name: Iuliia Prymak

Date of birth: 18.05.1987

Place of birth: Charkiw, Ukraine

Nationality: Ukraine

Gender: Female

Marital status: Married

Email: iuliia.prymak@catalysis.de, prymak\_julia@mail.ru

Phone number: +4917682463806

### Academic Education

4/2015-present	<p>Leibniz Institute for Catalysis at University of Rostock, Germany</p> <p>PhD student (guest) at Bioinspired Homo- &amp; Heterogeneous Catalysis</p> <p>Supervisors: PD Dr. habil. E. Kondratenko , Dr. V. N. Kalevaru</p>
5/2011-3/2015	<p>Leibniz Institute for Catalysis at University of Rostock, Germany</p> <p>PhD student at the Department of Heterogeneous Catalytic Processes</p> <p>Supervisors: PD Dr. habil. A. Martin, Dr. V. N. Kalevaru</p>
1/2010-4/2011	<p>The state-owned enterprise "Turboatom" of Charkiw, Ukraine</p> <p>Engineer at the Department of Radiography with X-rays and gamma rays</p>
5/2009	<p>University of Duisburg-Essen, Germany</p> <p>DAAD Scholarship holder (Leonard-Euler program) at the Department of Solid State Chemistry and Bio-Inorganic Chemistry</p> <p>Supervisor: Prof. Dr. M. Epple</p>
9/2008-6/2009	<p>National University of Charkiw, Ukraine</p> <p>Master at the Department of Solid-State Physics</p> <p>Master Thesis "Alterung von karbonisierter Hydroxylapatit Keramik bei Raumtemperatur"</p>

9/2004-6/2009

Supervisors: Prof. Dr. Z. Z. Zyman, Dr. M. V. Tkachenko

National University of Charkiw, Ukraine

Bachelor at the Department of Solid-State Physics

Bachelor Thesis "Untersuchung des Alterungsprozesses des karbonisierten Hydroxylapatits"

Supervisors: Prof. Dr. Z. Z. Zyman, Dr. M. V. Tkachenko